Reactor Physics Analysis
of the Pin-Cell Doppler Effect
in a Thermal Nuclear Reactor

A computational study

PROEFSCHRIFT

ter verkrijging van de graad van doctor
aan de Technische Universiteit Delft,
op gezag van de Rector Magnificus Prof. Ir. K.F. Wakker,
in het openbaar te verdedigen ten overstaan van een commissie,
door het College van Dekanen aangewezen,
op dinsdag 8 november 1994
te 10.30 uur
door

Wilhelmus Joannes Maria DE KRUIJF

natuurkundig ingenieur
geboren te 's-Hertogenbosch

Dit proefschrift is goedgekeurd door de promotor:
Prof. Dr. Ir. H. van Dam

en de toegevoegd promotor: Dr. Ir. J.E. Hoogenboom.

Dr. Ir. A.J. Janssen heeft als begeleider in belangrijke mate aan het totstandkomen
van het proefschrift bijgedragen.

stellingen

behorende bij het proefschrift

Reactor Physics Analysis of the Pin-Cell Doppler Effect in a Thermal Nuclear Reactor

1. De benadering van een vierkante eenheidscel door een cylindrische cel met hetzelfde oppervlak wordt in de reactorfysica ten onrechte als Wigner-Seitz-benadering aangeduid.

   C. Kittel, *Introduction to Solid State Physics*, John Wiley & Sons, New York, 1967

2. Een afname van de absorptie van neutronen in een bepaald gedeelte van het energiespectrum ten gevolge van een stijgende splijtstoftemperatuur gaat niet noodzakelijkerwijs gepaard met een positief effect op de reactiviteit, zoals door Alapour en Karam ten onrechte wordt beweerd voor de absorptie van neutronen in de laag-energetische resonanties van ^{238}U in een snelle reactor.

   A. Alapour en R.A. Karam, "The Effects on Reactivity Coefficients of Spectral Shifts Induced by Doppler Broadening," *Nucl. Sci. Eng.*,**79**, 278 (1981)

3. Monte-Carlo-berekeningen van Dancoff-factoren in onregelmatige geometrieën gaan voorbij aan het feit dat zulke factoren per definitie niet nauwkeurig kunnen worden uitgerekend in een onregelmatige geometrie.

   S. Fehèr et al., "Monte Carlo Calculation of Dancoff Factors in Irregular Geometries," *Nucl. Sci. Eng.*, **117**, 227 (1994)

4. Het efficiënte gebruik van neutronen in een CANDU-reactor heeft een positieve koelwatertemperatuurcoëfficient tot gevolg.

5. Hoewel goede nucleaire gegevens essentieel zijn voor de validatie van reactorfysische programma's, zijn ze volkomen onbelangrijk voor de verificatie van deze programma's.

6. Wanneer men de radioactiviteit in de omgeving voor generaties in de verre toekomst wil beperken is het zaak het aanwezige uraniumerts te gebruiken.

   N. Holloway, "Uranium: don't leave it in the ground!," *Atom*, **404**, 15 (1990)

7. "Computational benchmarks" zouden meer gericht moeten zijn op het kwantificeren en kwalificeren van verschillen dan op het vaststellen van de mate van overeenkomst.

8. Het "rim"-effect is een randverschijnsel.

9. De eerste experimentele bevestiging van het Doppler-effect is te danken aan de Nederlandsche Rhijnspoor.

10. Alleen computers zijn eigenwijzer dan onderzoekers.

11. De aanleg van de Betuwelijn voorkomt spoorvorming op Nederlandse snelwegen.

Willy de Kruijf, 8 november 1994

aan mijn ouders

Contents

Chapter 1

Introduction

In the first attempts to estimate the possibilities of achieving a nuclear chain reaction on the basis of natural uranium, one of the important issues was the amount of resonance absorption by ^{238}U [1,2]. The fast neutrons from fission have to slow down to thermal energies where they induce fission of ^{235}U. It is just in this epithermal energy range that ^{238}U has nuclear resonances. The absorption of neutrons in these nuclear resonances is called resonance absorption. The resonance absorption in uranium is so high that it is either necessary to use enriched uranium as is done in light water reactors or to use moderators such as graphite or heavy water that absorb few thermal neutrons.

A problem which was first raised by Bohr is the increase of resonance absorption due to the Doppler broadening of the resonances with increasing temperature [3]. This might stop the nuclear chain reaction because of the deposition of heat in uranium. However, the Doppler effect is more a benefit than a problem because the fuel temperature effect, which mainly consists of the Doppler effect, is the only prompt feedback effect on the nuclear chain reaction in nuclear reactors [4]; there is no time delay between the deposition of fission heat in the fuel and the neutronic feedback. The Doppler effect is inherent which means that it is totally reliable; it is impossible to assign some kind of failure probability to it.

The Doppler effect is very important for the dynamic behaviour of a nuclear reactor both under normal and under abnormal (accident) conditions. The background to study the Doppler effect in this work lies in the fact that it is essential for the limitation of fast reactivity initiated transients [4–6]. A transient is the general term for practically all events in which the rate of heat release does not balance the rate of heat removal. Reactivity initiated transients form a special group of transients in which the inadvertent introduction of reactivity causes the transient. These transients may lead to an excursion of reactor power for which the period is so small that mechanical shutdown devices cannot limit the power

before it reaches destructive levels. Moreover, the moderator temperature effect can be neglected in view of the time constants for heat transfer from the fuel to the coolant. So, the Doppler effect, or rather the fuel temperature effect, is the only phenomenon which limits the initial power peak in such a transient.

Although we focus on the Doppler effect in a Pressurized Water Reactor (PWR), our calculations can easily be extended to any thermal reactor type. In a PWR the uncontrolled withdrawal of control rods, the control rod ejection, and the inadvertent dilution of the soluble boron concentration form reactivity initiated transients [5].

The strong spatial dependence of the power distribution asks for a three-dimensional treatment of reactivity initiated transients. With the developments in whole-core three-dimensional calculations [7–9], whole-core time-dependent problems can be treated in an efficient and accurate way. However, little attention has been paid to how the fuel temperature should be defined for an arbitrary radial temperature profile in a fuel pin. This profile is nearly parabolic for a stationary situation, but varies during transients. Computer codes do not model this temperature profile in the neutronics calculation, but use an effective fuel temperature [7,10,11]. However, the effective fuel temperatures have mainly been studied for a parabolic temperature profile [12–17], and even then different expressions to calculate the effective fuel temperature are found. The calculation of these effective fuel temperatures is the main topic in this work. In fact, the resonance absorption has to be calculated accurately for an arbitrary temperature profile in the fuel pin. Then, it has to be compared with the resonance absorption in a fuel pin with a homogeneous temperature to obtain the effective fuel temperature.

A precise calculation of the effective fuel temperature is not only important for the analyses of transients, but also for the calculation of stationary situations. Although the determination of the effective fuel temperature is a secondary effect for these calculations, an accurate determination of these effective fuel temperatures might be important to improve these calculations even further in view of the high accuracy which is achieved nowadays in calculations of stationary situations [18].

It is not necessary to consider the whole reactor core for the analysis of the Doppler effect. We have studied the Doppler effect in a pin cell, which is the smallest possible unit cell in a nuclear reactor. Figure 1.1 shows such a pin cell.

However, does the fuel temperature effect in pin-cell calculations agree with the fuel temperature effect in reality? Chapter 4 deals with this problem, and, moreover, an analysis of the fuel temperature effect is presented. Such an analysis gives an idea of the importance of different contributions, and is very useful in determining sources of discrepancy between different codes or data libraries.

Because the influence of the radial temperature profile is a second-order effect in relation with the quantities that are usually studied in reactor physics, the calculational method has to be very accurate. Besides, it is not possible in available
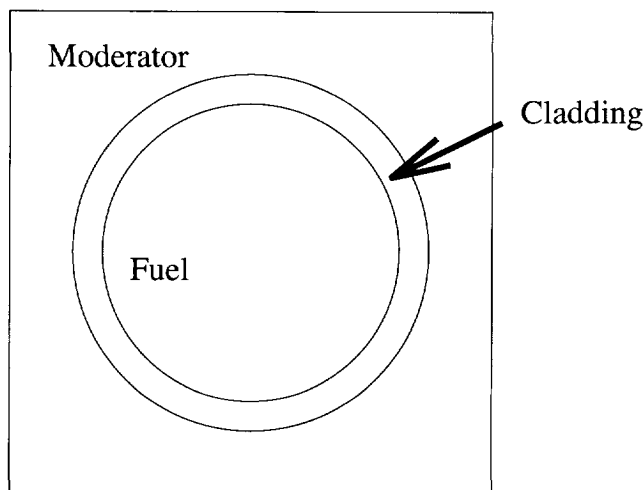
Figure 1.1: *Pin cell.*

computer codes to model a radial temperature profile in the fuel pin. For these purposes the code ROLAIDS-CPM has been developed. Because the detailed space- and energy-dependence of the neutron flux cannot be measured in sufficient detail, Monte Carlo calculations have been used to verify the calculational model of ROLAIDS-CPM. This is presented in chapter 5.

Because the larger part of the Doppler effect in thermal nuclear reactors is usually caused by ^{238}U, we focus on this isotope in chapter 6. The primary goal of this chapter is to clarify the background of different expressions which are used nowadays and to get more insight into the resonance absorption in a fuel lump with a certain temperature profile. The latter is achieved by studying the effect of simple temperature profiles in both a slab and a pin of ^{238}UO$_2$. Simple transient calculations have been done to study the influence of different expressions for the effective fuel temperature.

Another point which does not get attention in routine transient calculations is the power distribution in the fuel pin. This power distribution is not only determined by the neutron flux distribution in the fuel pin, but also by the distributions of the fissionable nuclides in the fuel pin. It may sharply increase towards the surface of the fuel pellet due to the buildup of plutonium [19,20]. Nevertheless, this power distribution is often assumed to be flat in transient calculations. The radial power distribution strongly depends on the radial distributions of the resonance absorption rates in a fuel pin. Because of the detailed calculations of these spatial distributions with ROLAIDS-CPM, it is possible to calculate the radial distributions of the nuclides very precisely. Measurements of the nuclide distributions

offer the opportunity to compare the calculational results with experimental data [20]. These radial burnup calculations are presented in chapter 7, together with a discussion about the effective fuel temperature in fuel with a certain burnup.

First, however, a short theoretical introduction on resonance absorption is presented in chapter 2, followed by a description of the calculational methods in chapter 3.

Chapter 2

An introduction on the theory of resonance absorption

2.1 Introduction

The goal of this chapter is to familiarize the reader with the theory of resonance absorption. This is done on the basis of relatively simple physical models.

2.2 Nuclear resonances

Discrete energy levels of a nucleus lead to sharp peaks in the neutron interaction cross section of the nucleus for specific centre-of-mass (CM) kinetic energies E_C. This behaviour of the cross section is called a nuclear resonance. The concept of a nuclear resonance is treated here on the basis of the Breit-Wigner model for a single radiative capture resonance.

When the influence of other levels is neglected, the value of the microscopic radiative capture cross section σ_γ for a resonance is given by the single level Breit-Wigner formula [21]:

$$\sigma_\gamma(E_C) = \frac{\lambda_C^2}{4\pi} g \frac{\Gamma_n \Gamma_\gamma}{(E_C - E_0)^2 + \left(\frac{\Gamma}{2}\right)^2}, \tag{2.1}$$

where λ_C is the wavelength of the incident neutron in the centre-of-mass system, g the statistical spin factor, Γ the total level width, Γ_γ the energy-independent partial level width for gamma emission, Γ_n the neutron level width, and E_0 the

resonance energy. With:

$$x = 2\frac{(E_C - E_0)}{\Gamma},\tag{2.2}$$

$$\Gamma_n = \Gamma_{n0}\left(\frac{E_C}{E_0}\right)^{\frac{1}{2}},\tag{2.3}$$

and

$$\sigma_0 = \frac{\lambda_0^2}{\pi}\frac{\Gamma_{n0}}{\Gamma_0}g,\tag{2.4}$$

the single level Breit-Wigner cross section is given by:

$$\sigma_\gamma(E_C) = \sigma_0\frac{\Gamma_\gamma}{\Gamma}\left(\frac{E_0}{E_C}\right)^{\frac{1}{2}}\frac{1}{1+x^2},\tag{2.5}$$

where the energy-dependence of Γ has been neglected.

The dependence of the cross section of a nucleus on the incident energy of a neutron can be very complicated due to the occurrence of many nuclear resonances. In figure 2.1 the radiative capture cross section of ^{238}U between 1 eV and 1 keV is given as an example (1 b = 10^{-28} m^2).
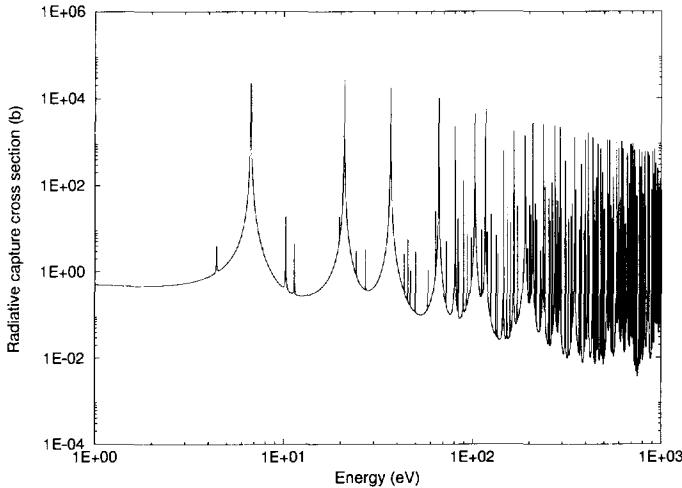

Figure 2.1: *Capture cross section of* ^{238}*U between 1 eV and 1 keV at T=0 K (Joint Evaluated File 2 (JEF2) data).*

The energy range where the single resonances cannot be distinguished experimentally is called the unresolved resonance range. Logically, the lower-energy range is referred to as the resolved resonance range.

Reactor physicists use evaluated nuclear data files as basic input data for their calculations. In these files the resonance parameters, which are necessary to reproduce the nuclear cross sections, are given. Different formalisms, of which the single level Breit-Wigner is the most simple, are used to represent the resonance behaviour [22]. Because multilevel effects are important for reactor physics calculations [23], multilevel formalisms are in widespread use nowadays.

2.3 Doppler broadening

Because the cross section depends on the CM energy, the thermal motion of the nuclei has to be taken into account. The cross section is a function of the relative velocity $| \vec{v} - \vec{V} |$, where $\vec{v}$ is the velocity of the neutron, and $\vec{V}$ is the velocity of the nucleus. This is in analogy with the well known acoustic Doppler effect where the observed frequency of a sound source depends on the relative speed between source and observer.

The effective cross section for a neutron of velocity v is defined as the cross section that gives the same reaction rate for stationary nuclei as the actual cross section gives for moving nuclei. This effective cross section is defined as [24]:

$$\bar{\sigma}(v, T) = \frac{1}{v} \int d^3V \mid \vec{v} - \vec{V} \mid \sigma(\mid \vec{v} - \vec{V} \mid) P(\vec{V}, T), \qquad (2.6)$$

where $P(\vec{V}, T)$ is the nuclear velocity distribution at temperature T. For many cases of interest this velocity distribution can be taken as the Maxwell-Boltzmann distribution:

$$P(\vec{V}, T) = \left(\frac{M}{2\pi k_B T} \right)^{\frac{3}{2}} \exp \left(\frac{-MV^2}{2k_B T} \right), \qquad (2.7)$$

where M is the mass of the nucleus and k_B Boltzmann's constant. To take account of lattice effects an effective Maxwellian temperature might be defined which can be different from the thermodynamic temperature [25]. At high temperatures the effective Maxwellian temperature equals the thermodynamic temperature [26].

The term effective temperature gives rise to some confusion of tongues. It is necessary to distinguish between the effective Maxwellian temperature and the effective fuel temperature which is the subject of this thesis. Lattice effects are not treated in this thesis.

When the single level Breit-Wigner formula is substituted in equation 2.6, and a few approximations are made, the Bethe-Placzek cross section is obtained for the neighbourhood of the resonance [27]. With:

$$\zeta = \frac{\Gamma}{\Gamma_D}, \Gamma_D = \left(\frac{4E k_B T}{A} \right)^{\frac{1}{2}} \approx \left(\frac{4E_0 k_B T}{A} \right)^{\frac{1}{2}}, \qquad (2.8)$$

where Γ_D is called the Doppler width, and A is the nuclear mass in units of the neutron mass (almost equal to the nuclear mass number), the Bethe-Placzek cross section [28] is given by:

$$\sigma_\gamma(E, T) = \sigma_0 \frac{\Gamma_\gamma}{\Gamma} \psi(\zeta, x), \qquad (2.9)$$

where

$$\psi(\zeta, x) = \frac{\zeta}{2\sqrt{\pi}} \int_{-\infty}^{\infty} dy \frac{\exp\left[-\frac{1}{4}(x - y)^2 \zeta^2\right]}{1 + y^2}. \qquad (2.10)$$

The Bethe-Placzek cross section is very useful in analysing Doppler broadening. An interesting point is that the area under the Bethe-Placzek cross section is independent of the temperature [26].

Figure 2.2 shows the 6.7 eV capture resonance of ^{238}U at different temperatures. With this figure the term Doppler broadening becomes clear.
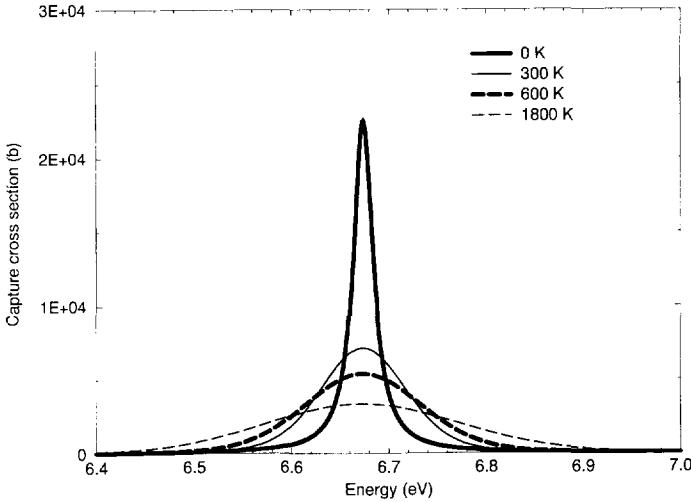
Figure 2.2: *Nuclear capture resonance of ^{238}U at 6.7 eV for different temperatures.*

It should be noted that the Doppler effect in reactor physics does not refer to the Doppler broadening of the resonances as such, but to the change of resonance absorption due to this Doppler broadening. The latter effect is explained later in this chapter. First, some general aspects of neutron slowing down and resonance absorption in a nuclear reactor are treated.

2.4   Slowing down of neutrons

The purpose of a moderator in a nuclear reactor is to slow down the neutrons to thermal energies where they have a high probability to induce fission. In the energy range where most of the Doppler effect occurs, slowing down takes place by elastic scattering collisions. This means that slowing down is most effective on light nuclides because the average energy loss in a collision with a heavier nuclide is less. In this section the slowing-down process is studied in an infinite homogeneous medium.

First, some important physical quantities are introduced. The macroscopic cross section is defined as:

$$\Sigma = N\sigma, \tag{2.11}$$

where N is the nuclide density. The macroscopic total cross section is then given by:

$$\Sigma_t = \Sigma_a + \Sigma_s, \tag{2.12}$$

where Σ_a is the absorption cross section, and Σ_s is the scattering cross section. The neutron flux per unit energy interval $\phi(E)$ is given by:

$$\phi(E) = vn(E), \tag{2.13}$$

where $n(E)$ is the neutron density per unit energy interval.

With these notations, the neutron balance in an infinite homogeneous medium reads:

$$\Sigma_t(E)\phi(E) = \int_0^\infty dE' \, \Sigma_s(E' \to E)\phi(E') + S(E), \tag{2.14}$$

where $\Sigma_s(E' \to E)$ is the differential macroscopic cross section for scattering from energy E' to energy E, and $S(E)$ is a homogeneously distributed neutron source. With the assumptions of elastic scattering, isotropic scattering in the CM coordinate frame, and stationary nuclei, the following slowing-down equation is obtained:

$$\Sigma_t(E)\phi(E) = \sum_i \int_E^{\frac{E}{\alpha_i}} dE' \, \frac{\Sigma_{s_i}(E')\phi(E')}{(1 - \alpha_i)E'} + S(E), \tag{2.15}$$

where $\alpha = \left(\frac{A-1}{A+1}\right)^2$, and where the index i indicates different nuclides. The left-hand side of equation 2.15 is just the collision rate per unit volume per unit energy, which is called the collision rate density.

A useful quantity in slowing-down calculations is the slowing-down density $q(E)$ which is defined as the number of neutrons per unit volume per unit time slowing down past energy E.

Equation 2.15 can be solved analytically in the absence of neutron absorption [28]. Far below source energies the collision rate density is given by:

$$\Sigma_t(E)\phi(E) = \Sigma_s(E)\phi(E) = \frac{q(E)}{\xi E} = \frac{q}{\xi E},\qquad(2.16)$$

where $\xi(= 1 + \frac{\alpha}{1-\alpha}\ln\alpha)$ is the average lethargy gain $\overline{\Delta u}$ per collision, with the lethargy variable u defined as:

$$u = \ln\left(\frac{E_{ref}}{E}\right),\qquad(2.17)$$

where E_{ref} is some reference energy. The neutron flux is given by:

$$\phi(E) = \frac{q(E)}{\Sigma_s(E)\xi E}.\qquad(2.18)$$

In the absence of absorption and leakage the neutron slowing-down density is of course constant, but equation 2.18 can also be applied when part of the neutrons are absorbed at higher energies without disturbing the asymptotic flux behaviour at energies just above a specific energy range.

Because $\Sigma_s(E)$ and $q(E)$ are constant between the resonances, the neutron flux in the epithermal range above a specific energy range is described by:

$$\phi(E) = \frac{C}{E},\qquad(2.19)$$

$$\phi(u) = C \equiv \phi_u,\qquad(2.20)$$

where $\phi(u)$ is the flux per unit lethargy, and where the flux per unit lethargy above the resonances ϕ_u is often assumed to be 1 cm^{-2} s^{-1} in calculations.

2.5 Resonance absorption and Doppler effect

The concept of resonance absorption is treated here on the basis of a rather approximate method, which elucidates the most important aspects. First, some useful quantities are defined.

2.5.1 Definitions

For this purpose an infinite homogeneous medium is considered. The absorption rate A_i per unit volume in a particular energy range i is given by:

$$A_i = \int_{E_i}^{E_{i-1}} dE\, \Sigma_a(E)\phi(E).\qquad(2.21)$$

The subscript of the energy variable increases with decreasing energy (increasing lethargy).

Resonance absorption is often characterized by the effective resonance integral I_i which is defined as:

$$I_i = \int_{E_i}^{E_{i-1}} dE \sigma_a(E) \frac{\phi(E)}{\phi_u}, \tag{2.22}$$

where the asymptotic flux above E_{i-1} is given by equation 2.20. The total effective resonance integral I is the effective resonance integral for all resonance neutron capture [26]. The reaction rate density can be calculated from the effective resonance integral by multiplying it with the asymptotic flux per unit lethargy (equation 2.20) and the nuclide density.

The absorption probability is obtained by dividing equation 2.21 by the slowing-down density just above the energy range $q(E_{i-1})$. The escape probability p_i for this specific energy range, which might encompass one single resonance, is then given by:

$$p_i = 1 - \frac{1}{q(E_{i-1})} \int_{E_i}^{E_{i-1}} dE \Sigma_a(E) \phi(E), \tag{2.23}$$

where it is assumed that the energy E_{i-1} lies below the source energies. The escape probability $p(E)$ to the energy E, which again lies below the source energies, is given by:

$$p(E) = 1 - \frac{1}{S_0} \int_{E}^{E_{max}} dE \Sigma_a(E) \phi(E), \tag{2.24}$$

where S_0 is the source density integrated over energy, and E_{max} the maximum source energy. Note that the escape probability $p(E)$ in an infinite medium is just equal to the slowing-down density $q(E)$ normalized to S_0.

Because most of the absorption takes place in the resonances, the escape probability to thermal energies $p(E_{thermal})$ is called the resonance escape probability p. This resonance escape probability is used to calculate the multiplication factor k, which is the ratio between neutron production and neutron loss. The multiplication factor for an infinite medium k_∞ is given by the four-factor formula [24]:

$$k_\infty = \eta f p \epsilon, \tag{2.25}$$

where η is the number of neutrons produced per thermal neutron absorbed in the fuel, f the number of thermal neutrons absorbed in the fuel divided by the total number of thermal neutrons absorbed (thermal utilization factor), and ϵ the total number of neutrons produced by fission divided by the number of neutrons produced by thermal fission.

A very important quantity in reactor physics is the reactivity ρ, which describes the departure of k from unity:

$$\rho = \frac{k-1}{k}.\qquad(2.26)$$

The influence of the fuel temperature T_F on the reactivity can be described in terms of a fuel temperature coefficient α_F:

$$\alpha_F = \frac{\partial \rho}{\partial T_F} = \frac{1}{k^2}\frac{\partial k}{\partial T_F}.\qquad(2.27)$$

The definition and analysis of this coefficient for pin-cell calculations on an infinite lattice is the subject of chapter 4.

In the next subsections the calculation of the neutron flux in the presence of nuclear resonances is treated in both a homogeneous and a heterogeneous medium.

2.5.2   Homogeneous medium

Let us consider a mixture of a light moderator and a heavy resonance absorber. The total cross section of the moderator $\Sigma_t^M(E)$ is assumed to be equal to the energy-independent potential scattering cross section $\Sigma_p^M = \sigma_p^M N_M$, where σ_p is the microscopic potential scattering cross section and the sub- or superscript M denotes the moderator. The total cross section of the resonance absorber $\Sigma_t^A(E)$ is assumed to be equal to the absorption cross section $\Sigma_a^A(E) = \sigma_\gamma^A N_A$, where the sub- or superscript A denotes the absorber. Because the average energy loss in a scattering collision with the moderator is much larger than the width of the resonance, the neutron flux in the first term on the right-hand side of equation 2.15 can be replaced by the asymptotic ϕ_u/E flux. The neutron flux, which results from the evaluation of equation 2.15, is given by:

$$\phi(E) = \frac{\phi_u \Sigma_p^M}{(\Sigma_p^M + \Sigma_a^A(E))E}.\qquad(2.28)$$

This equation shows the flux dip which occurs near resonance energies. This phenomenon is known as energy self-shielding.

More elaborate expressions for the flux can be found by taking account of scattering by the absorber. Different approximations are made which depend on the width of the resonance in comparison with the energy loss in a scattering collision with the absorber. This leads to the so-called narrow-resonance, wide-resonance, and intermediate-resonance approximations for the flux [29].

The flux from equation 2.28 is used here to illustrate the Doppler effect. With the Bethe-Placzek cross section from equation 2.9 the effective resonance integral

is given by:

$$I_i = \int dE \frac{N_M \sigma_p^M \sigma_0 \psi(\zeta, x)}{\left(N_M \sigma_p^M + N_A \sigma_0 \psi(\zeta, x)\right) E} \approx \frac{\Gamma N_M \sigma_p^M}{E_0 N_A} J(\zeta, \beta), \qquad (2.29)$$

where $J(\zeta, \beta)$ is given by:

$$J(\zeta, \beta) = \int_0^\infty dx \frac{\psi}{\psi + \beta}, \qquad (2.30)$$

and

$$\beta = \frac{N_M \sigma_p^M}{N_A \sigma_0}. \qquad (2.31)$$

The value of J increases as the temperature increases [26] which means that the resonance absorption increases with temperature. This is the Doppler effect in reactor physics. Note that both for $\beta \rightarrow \infty$ (infinite dilution) and for $\beta \rightarrow 0$ (only absorption) the resonance absorption rate does not depend on the temperature.

A qualitative way to explain the Doppler effect is based on the complete neglect of scattering in a certain energy range. This might be done for the centre of a purely absorbing resonance where the cross section is very high. Then, all neutrons with energies in this energy range are absorbed. The absorption is simply linear with the width of this so-called black energy range, because the rate of supply of neutrons does not depend on the resonance cross section for a narrow resonance. As temperature increases, the resonance broadens and so does the black energy range. The decrease of the cross section in the centre of the resonance has no effect on the absorption of neutrons, but the increase of the cross section in the wings of the resonance certainly has. One might say that these wings become more "grey"; more neutrons are absorbed.

2.5.3   Heterogeneous Medium

In a heterogeneous medium the neutron flux is also space- and angle-dependent. The resonance absorption calculations are generally based on a collision probability approach. The energy-dependent volume-averaged flux in a certain zone is given by:

$$\Sigma_{t,i}(E) V_i \phi_i(E) = \sum_j V_j P_{j,i}(E) S_j(E), \qquad (2.32)$$

where V_i is the volume of zone i, $P_{j,i}(E)$ is the probability that a neutron from zone j has its next collision in zone i, and $S_j(E)$ is the volume-averaged slowing-down source in zone j. As the slowing-down source is located in the moderator zones, the neutron flux in the fuel decreases towards the centre of the fuel lump. This phenomenon is known as spatial self-shielding.

The general procedure in reactor physics calculations is to assume uniform and isotropic sources in the different zones. With these last assumptions the following reciprocity relation [30] can be used:

$$\Sigma_{t,i}(E)V_i P_{i,j}(E) = \Sigma_{t,j}(E)V_j P_{j,i}(E). \tag{2.33}$$

This relation is very useful in treating heterogeneous media.

A lot of effort has been done to establish equivalence relations between the effective resonance integral in a homogeneous medium and that in a heterogeneous medium. A more extensive treatment of the general theory can be found in references 24, 26, 29, and 30. Here, we will show how such an equivalence can be established in our simple model.

Only two zones are taken into account: one fuel (absorber) zone with volume V_F, and one moderator zone with volume V_M. With the same assumptions regarding the cross sections as in the previous subsection, with the asymptotic ϕ_u/E flux in the moderator, and by using the reciprocity relation equation 2.33, the neutron flux in the fuel ϕ_F is given by:

$$\phi_F(E) = \frac{\phi_u P_{FM}(E)}{E}, \tag{2.34}$$

where $P_{FM}(E)$ is the probability for a neutron from the fuel to have its next collision in the moderator. In the case of an isolated fuel lump this is just the escape probability $P_{esc}(E)$.

The escape probability can be written in terms of the escape cross section σ_e:

$$P_{esc}(E) = \frac{\sigma_e(E)}{\sigma_e(E) + \sigma_t^A(E)}. \tag{2.35}$$

When equation 2.35 is substituted in equation 2.34 it can be seen from a comparison with equation 2.28 that a heterogeneous lattice with a given $N_A\sigma_e$ has the same resonance integral as a homogeneous mixture with a given $\Sigma_p^M = N_A\sigma_e$. The value of σ_e depends on the approximation which is used for the escape probability. This approximation has to be in the form of equation 2.35 but with an energy-independent σ_e. For example, Wigner's rational approximation reads:

$$P_{esc}(E) = \frac{\frac{S_F}{4V_F}}{\frac{S_F}{4V_F} + \Sigma_t^A(E)}, \tag{2.36}$$

where S_F is the surface area of the fuel lump. The escape cross section is then given by:

$$\sigma_e = \frac{S_F}{4V_F N_A}. \tag{2.37}$$

When a lattice is considered the escape probability has to be corrected for the probability that a neutron which escapes the fuel has the next collision in another fuel lump. This lump shadowing effect, which reduces the resonance integral, is called the Dancoff effect. The value of σ_e has to be corrected for the Dancoff effect. When Wigner's rational approximation is used, the corrected escape cross section is given by [24]:

$$\sigma_e = \frac{S_F(1 - C_D)}{4V_F N_A},$$
(2.38)

where C_D is the Dancoff-Ginsberg factor [31].

A basic assumption in the models which treat the fuel as one lump is that the macroscopic cross section does not vary over the fuel lump. It is just this variation of the macroscopic cross section over the fuel pin that is important for studying the influence of a temperature profile. So, these models cannot be used in the present study; the detailed space- and energy-dependent neutron flux has to be calculated. The next chapter deals with these calculational methods.

Chapter 3

Calculational methods

3.1 Introduction

The calculational methods which are applied in this work are briefly discussed in this chapter to enable a better understanding of the results in the next chapters. This is done on the basis of figure 3.1 which displays the calculational scheme.

The figure clearly demonstrates the complicated structure of the calculational scheme. This has the advantage that different calculational routes can be used to tackle the same problem. Especially for verification purposes this feature is very useful as is shown in chapter 5.

At the top of figure 3.1 the evaluated nuclear data file (ENDF) is shown. These evaluated nuclear data files are the basis for all reactor physics calculations. In section 3.2 a description is given of the way these evaluated nuclear data files are processed with the code system NJOY [32] to obtain input-libraries for different reactor physics codes.

Then, section 3.3 deals with the most straightforward approach to a reactor physics problem: Monte Carlo simulation, for which MCNP [33] has been used (chapter 5). These calculations become more and more popular as the performance of computers improves. However, for accurate calculations of for example the fuel temperature effect these calculations consume a lot of time, even for a simple pin cell. So, deterministic methods are necessary.

In section 3.4 ROLAIDS-CPM [34] is described. We have developed it to do accurate slowing-down calculations in a one-dimensional geometry (chapters 5, 6, and 7) with the possibility to treat an arbitrary temperature profile.

Section 3.5 deals with slowing-down calculations (chapter 5) and k-effective calculations (chapters 4 and 7) as they are done with the one-dimensional discrete ordinates code XSDRN [35]. This code does not use energy-pointwise cross
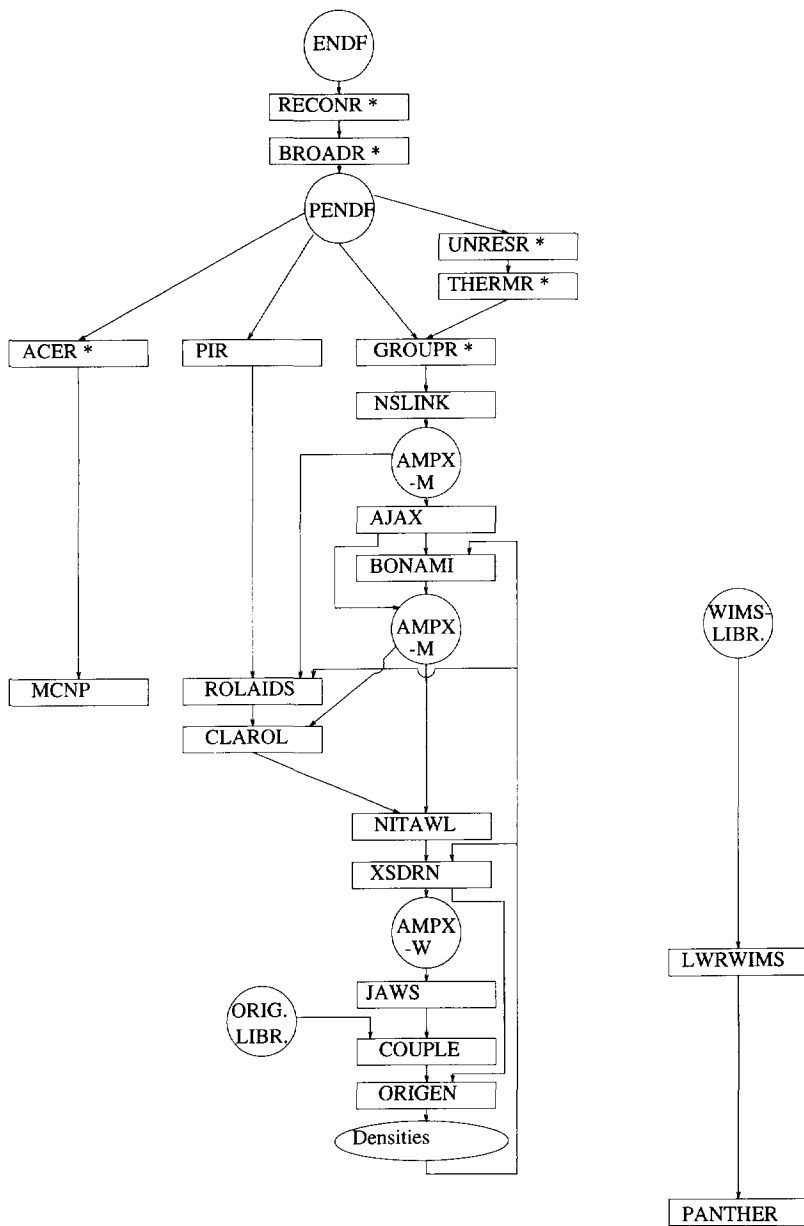
23

Figure 3.1: *Calculational scheme; modules from the NJOY code system are indicated with* *.

sections but so-called multigroup cross sections. The energy range is divided in different energy groups for which effective cross sections have to be computed in advance.

In section 3.6 the burnup calculations with ORIGEN [36] (chapter 7) are described. Special attention is given to the calculation of the radial distributions of the nuclide densities in a fuel pin.

Transient calculations are done with PANTHER [7] (chapters 6 and 7). PANTHER uses two-group cross sections which have been calculated by the light water reactor assembly code LWRWIMS [37], described in section 3.7. LWRWIMS calculates volume-averaged cross sections for a whole fuel assembly which is the smallest unit for reloading fuel in a reactor. A fuel assembly contains many fuel pins (e.g. 17 x 17). Section 3.8 deals with PANTHER.

3.2   Processing of cross sections

The NJOY code system is used to process the evaluated nuclear data files. This system consists of several modules (indicated in figure 3.1 with *). First, the energy-pointwise cross sections are reconstructed from the resonance parameters by RECONR. The resonances are generally represented by multi-level formalisms [22]. The energy grid is chosen in such a way that within a given tolerance the cross section can be obtained by linear interpolation. Then, the cross sections are Doppler broadened (see equation 2.6) by BROADR. The effective Maxwellian temperature is assumed to be equal to the thermodynamic temperature.

The pointwise evaluated nuclear data file (PENDF) produced by BROADR is used to make input libraries for three different calculational branches. First, ACER generates an input library for the Monte Carlo code MCNP. Secondly, PIR [34], which is not a module of NJOY, simply converts the format of the pointwise nuclear data on the PENDF to the format which is required for the slowing-down code ROLAIDS-CPM. Thirdly, GROUPR uses simple weighting fluxes to calculate multigroup cross sections. Before GROUPR, selfshielding in the unresolved resonance range is treated by UNRESR, and thermal scattering cross sections are produced by THERMR. UNRESR and THERMR are not necessary to prepare a multigroup library for slowing-down calculations. NSLINK puts the multigroup cross sections on a so-called AMPX-M(aster) multigroup library for further use by other codes.

3.3   Monte Carlo calculations

MCNP is a Monte Carlo code for coupled neutron and photon calculations with a continuous representation of the energy. We apply it to solve the time-independent

neutron transport equation:

$$\vec{\Omega} \bullet \nabla \varphi(\vec{r}, E, \vec{\Omega}) + \Sigma_t(E, \vec{r})\varphi(\vec{r}, E, \vec{\Omega}) = \qquad\qquad (3.1)$$
$$\int_0^{4\pi} d\Omega' \int_0^\infty dE' \Sigma_s(E' \to E, \vec{\Omega}' \to \vec{\Omega})\varphi(\vec{r}, E', \vec{\Omega}') + s(\vec{r}, E, \vec{\Omega}),$$

where $\vec{\Omega} = \frac{\vec{v}}{|v|}$ characterizes the direction of the neutron, φ is the angular neutron flux, $\Sigma_s(E' \to E, \vec{\Omega}' \to \vec{\Omega})$ the double differential scattering cross section for scattering from E' to E and $\vec{\Omega}'$ to $\vec{\Omega}$, and s the angular neutron source.

As in this work Monte Carlo codes are often used to establish reference results [38–40]. Possible limitations of MCNP are important in this context. Two important limitations are given here. First, the treatment of the unresolved resonances is not very thorough, but this does not influence slowing-down calculations in the resolved resonance range. Secondly, an assumption made in MCNP for the sampling of nuclide velocities and the neglect of upscattering above a certain energy boundary affect resonance absorption rates and thus the Doppler effect. Because of its importance these effects are shortly discussed here. More details can be found in references 41, 42 and 43.

A general view in reactor physics is that upscattering can be neglected above a certain incident neutron energy. MCNP neglects the velocity of the target for neutron energies above 400 $k_B T$ (except ^{1}H). However, the comparison should be based on the momentum instead of on the energy. So, the motion of heavy nuclides is still important at neutron energies where the motion of light nuclides can be neglected.

Even when the thermal motion of the nuclei is taken into account, MCNP makes an important assumpion which will be shortly explained here. When the energy of the neutron is close to the resonance energy, the double differential cross section in equation 3.1 depends strongly on the angle of scattering. This enhances the upscatter probability for neutrons with energies just below the resonance energy considerably. This effect is neglected in MCNP. In fact, in the sampling procedure for the direction of the nuclide it is assumed that the scattering cross section does not depend on energy. This assumption leads to isotropic sampling of the nuclide direction. Further research is necessary to establish the influence of this assumption on resonance absorption rates and the Doppler effect. This assumption certainly affects the reference status of MCNP and should be kept in mind. However, when very detailed results are required to test calculational methods, reference calculations are indispensable, and MCNP is the best tool available.

Because we want to make a comparison between Monte Carlo results and deterministic results, it is necessary to model a one-dimensional pin cell in MCNP. This is done by approximating the square pin cell from figure 1.1 by a cylindrical

pin cell with equal volume. This approximation is called the Wigner-Seitz approximation [30]. For the calculation of the neutron transport it is necessary to use isotropic reflection at the outer boundary instead of specular reflection. However, version 4.2 of MCNP is not able to treat isotropic reflection at a certain boundary. So, we have produced a version of MCNP which applies isotropic reflection at the outer cylindrical boundary of a pin cell. This has been done by changing the subroutine REFLEC in MCNP. The following lines have been added after label 20:

```
    PHI=RANG()*2*ACOS(-1.)
    CTHEI=SQRT(RANG())
    IF (ANG(3).NE.0) GO TO 25
    UUU=-CTHEI*ANG(1)-SQRT(1-CTHEI**2)*COS(PHI)*ANG(2)
    VVV=-CTHEI*ANG(2)+SQRT(1-CTHEI**2)*COS(PHI)*ANG(1)
    WWW=SQRT(1-CTHEI**2)*SIN(PHI)
    GO TO 27
 25 CONTINUE
```

where CTHEI is the cosine of the angle that the velocity vector of the reflected neutron makes with the inner surface normal, PHI is the angle of this vector in the plane perpendicular to the normal, ANG defines the normal on the surface, and (UUU, VVV, WWW) is the velocity vector of the neutron after reflection.

3.4   Slowing-down calculations with ROLAIDS-CPM

ROLAIDS [44,45] (Resonance OverLap Analysis In Discretely represented Systems) is a one-dimensional slowing-down code which uses energy-pointwise cross sections. It calculates the slowing-down source S_j^i at energy E_i in a specific zone j as:

$$S_j^i \;=\; \sum_k a_{k,j} C_j^k \tag{3.2}$$

$$=\; a_{i,j} C_j^i + \sum_{k<i} a_{k,j} C_j^k, \tag{3.3}$$

where $a_{k,j}$ is the coefficient for the contribution of the collision rate C_j^k in zone j at energy k to the source S_j^i resulting from the evaluation of the slowing-down integral:

$$S_j^i = \sum_m \frac{N_{j,m}}{(1-\alpha_m)} \int_{V_j} \int_{E_i}^{\frac{E_i}{\alpha_m}} \frac{\phi_j(E')\sigma_{sm}(E')}{E'} dE' dV, \tag{3.4}$$

where the subscript m denotes different nuclides.

The first term on the right-hand side of equation 3.3 has been taken separately, because the collision rate at energy i is calculated from the sources at energy i, which are not known yet. For convenience, suppose that the coefficient $a_{i,j}$ in the first term on the right-hand side of equation 3.3 is zero. This is not essential, but facilitates a better understanding of the equations involved. The slowing-down source can now be calculated directly from previously calculated collision rates at higher energies.

Now, the problem is how to calculate the collision rate C_j^i. Originally, this is done with the interface-currents method in ROLAIDS. We will demonstrate this method for a slab-geometry. The superscript i for the energy has been omitted in this demonstration. Figure 3.2 defines the in- and out-going currents for a specific zone j.
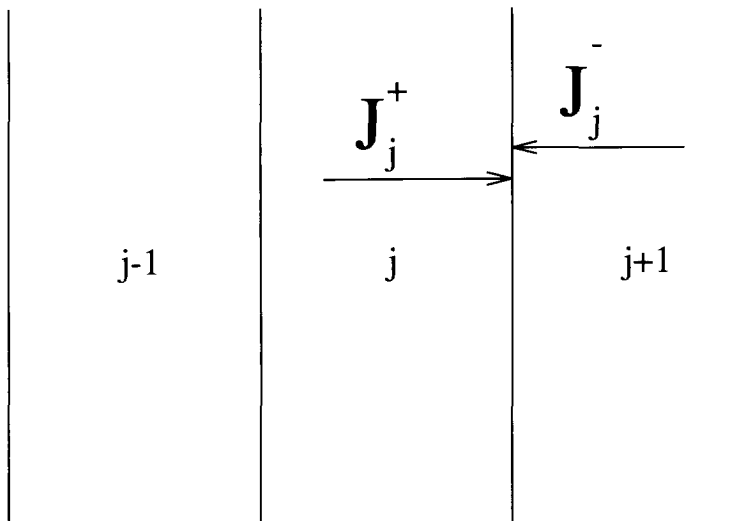
Figure 3.2: *Definition of the in- and out-going currents for zone j.*

The currents J_j^+ and J_j^- are calculated according to:

$$J_j^+ = J_{j-1}^+ T_j + \frac{1}{2} S_j P_j, \tag{3.5}$$

$$J_j^- = J_{j+1}^- T_{j+1} + \frac{1}{2} S_{j+1} P_{j+1}, \tag{3.6}$$

where T_j is the probability for a neutron from a cosine current at one boundary of zone j to arrive without collision at the other boundary of the zone, S_j the known slowing-down source in zone j, and P_j the probability for a neutron from a spatially

flat isotropic source in zone j to escape from this zone without having collided. A cosine current means that the flux is isotropic in the relevant half-space; the angular current density is linear with the cosine of the angle between the direction of the neutron and the normal at the boundary.

Three basic approximations are made in the interface-currents method:

- the scattering sources are assumed to be spatially flat in the zones,

- the scattering sources are assumed to be isotropic in the laboratory system,

- the fluxes at the interfaces between zones are assumed to be isotropic in each half-space.

These assumptions facilitate the calculation of the escape and transmission probabilities.

When the currents have been calculated, the collision rates C_j follow from:

$$C_j = (1 - T_j)J_j^- + (1 - T_j)J_{j-1}^+ + (1 - P_j)S_j. \tag{3.7}$$

Then the neutron flux in zone j is given by:

$$\phi_j = \frac{C_j}{\Sigma_{t_j} V_j}. \tag{3.8}$$

This neutron flux, which is calculated for all energy points i, is used to calculate effective group cross sections σ_{eff}:

$$\sigma_{eff} = \frac{\int_E \int_V \sigma(E)\phi(\vec{r}, E)dVdE}{\int_E \int_V \phi(\vec{r}, E)dVdE}, \tag{3.9}$$

which are used in multigroup codes such as XSDRN, in which the spatial dependence of the neutron flux is calculated more accurately.

Here, we will comment on this multigroup treatment. In fact, the group averaged cross section should depend on the direction of the neutron:

$$\sigma_{eff}(\vec{r}, \vec{\Omega}) = \frac{\int_{E_g}^{E_{g-1}} \sigma(\vec{r}, E)\varphi(\vec{r}, E, \vec{\Omega})dE}{\int_{E_g}^{E_{g-1}} \varphi(\vec{r}, E, \vec{\Omega})dE}. \tag{3.10}$$

This can be seen by integrating equation 3.1 over the energy interval. Only when the neutron flux is isotropic, the effective cross section does not depend on $\vec{\Omega}$, and equation 3.9 is correct. Otherwise, an approximation is made in this multigroup treatment. This approximation gets worse the more $\sigma(E)$ varies over the group energy interval.

Now, the influences of the three basic assumptions in the interface-currents method are discussed.

The assumption of spatially flat sources in the different zones is not a real limitation because the effect of this assumption can be made very small by taking more zones into account.

The assumption of isotropic sources in the LAB-system, however, is a limitation of ROLAIDS, but this assumption is not expected to have much effect in the calculation of resonance absorption effects. The scattering source in the moderator is mainly isotropic because the flux in the moderator is mainly isotropic and the scattering source in the fuel is mainly isotropic because the scattering on the heavy nuclides in the fuel is nearly isotropic. The influence of this assumption can be investigated with multigroup lattice codes which can handle non-isotropic scattering in the LAB-system.

The assumption of cosine currents at the interfaces of the zones is a more serious limitation. When the distribution of the absorption over the fuel pin is wanted, the fuel has to be divided in different zones. The currents at the interfaces of the zones in the fuel do not have a cosine profile at the resonance energies. A finer discretization of the spatial mesh only makes things worse because the assumption is made at every interface.

To overcome the assumption of cosine currents at the interfaces of the zones we have implemented the collision probability method in ROLAIDS, mainly by adding some new subroutines [34]. Therefore, we have given ROLAIDS the extension 'CPM', where 'CPM' stands for Collision Probability Method. ROLAIDS-CPM can solve equation 2.32, where the collision probabilities have been determined for spatially flat and isotropic scattering sources. As in the interface-currents method the neutron source can be computed from the collision rates at higher energies. The collision probabilities in the slab geometry are calculated with exponential integrals [24], while Carlvik's method [46] is used to calculate the collision probabilities in the cylindrical geometry with Bickley functions [47]. Reference 34 gives further details on the calculation of these collision probabilities.

An important new feature of ROLAIDS-CPM is the possibility to use one nuclide at different temperatures in the same problem.

With the collision probability method ROLAIDS-CPM can be used to do a direct calculation of resonance absorption rates from the energy-pointwise cross sections. Since the influence of the assumption of spatially flat scattering sources can be relaxed by taking more zones into account, the only basic assumption is the assumption of isotropic scattering sources in the laboratory system. As stated before, this assumption is expected to have little influence.

Another advantage of the collision probability method is that the group-averaged cross sections are calculated more rigourously. This enables a very direct determination of the accuracy of the multigroup approximation equation 3.9 (chapter 5).

3.5   Multigroup calculations with XSDRN

Reactor physics calculations are often based on multigroup libraries such as an AMPX-M. AJAX is used to pick specific nuclides from these AMPX-M libraries. These libraries are problem independent in as far as the neutron spectrum does not vary very much within each individual energy group. Because of the strong dependence of resonance cross sections on energy, special attention has to be given to the treatment of these resonances. In our scheme (figure 3.1) BONAMI [48] deals with the unresolved resonances, while NITAWL [49,50] calculates self-shielded cross sections for the resolved resonance range. Both BONAMI and NITAWL treat the fuel as one lump which means that the spatial variation of the self-shielding in a fuel pin cannot be treated by these codes. The treatment of the resolved resonances can also be done by ROLAIDS-CPM/CLAROL, in which case NITAWL is only used for a format conversion. Then, it is possible to take the spatial effect of self-shielding into account in a multigroup calculation.

XSDRN does a one-dimensional discrete ordinates (S_N) neutron transport calculation. Two different types of calculations have been done. First, k-effective (k) is calculated by solving equation 3.1 where the source is given by:

$$s(\vec{r}, E, \vec{\Omega}) = \tag{3.11}$$
$$\frac{1}{4\pi k}\chi(\vec{r}, E) \int_0^{4\pi} d\Omega' \int_0^\infty dE'\, \nu(\vec{r}, E')\Sigma_f(\vec{r}, E')\varphi(\vec{r}, E', \vec{\Omega}')$$

where $\chi(E)$ is the neutron spectrum of the fission source, and ν is the average number of neutrons produced per fission. The use of k to create an artificial balance in pin-cell calculations is discussed in chapter 4.

A second type of calculation is the slowing-down calculation for which a fixed source is specified. Only a limited energy range is taken into account to solve equation 3.1.

Important parameters in the XSDRN calculations are the order of the angular quadrature, the spatial mesh, the number of energy groups, and the order of scattering anisotropy. By varying the last one, the influence of the assumption of isotropic sources in ROLAIDS-CPM has been investigated (chapter 5).

3.6   Burnup calculations with ORIGEN

The burnup calculations have been done in a somewhat different way than usual, because the radial distributions of the nuclide densities have been taken into account.

ORIGEN uses effective volume-averaged one-group cross sections in order to solve:

$$\frac{\partial N_i}{\partial t} = \sum_j \gamma_{ji}\sigma_{f,j}N_j\phi_t + \sum_k \sigma_{a,k\to i}N_k\phi_t + \sum_l \lambda_{l\to i}N_l \qquad (3.12)$$
$$-\sigma_{a,i}N_i\phi_t - \lambda_i N_i,$$

where γ_{ji} is the fission yield of nuclide i due to the fission of nuclide j, $\sigma_{a,k\to i}$ is the reaction cross section of nuclide k (e.g. (n,γ), $(n,2n)$) which results in nuclide i, $\lambda_{l\to i}$ is the decay constant for decay from nuclide l to nuclide i, $\sigma_{a,i}$ is the total absorption cross section of nuclide i, and λ_i is the decay constant of this nuclide.

The effective group cross sections are calculated from a spectrum weighting procedure. The neutron energy spectrum in the fuel pin or in a specific zone of the fuel pin is calculated by XSDRN. JAWS picks the desired nuclides from the AMPX-W(eighted) library. Then, COUPLE combines an existing ORIGEN library with the weighted library, and calculates the effective cross sections to be used by ORIGEN. When the radial distributions of the nuclide densities are calculated, a separate burnup calculation has to be done for every zone. During burnup, the spectrum in the fuel pin changes, which implies that the effective cross sections have to be updated. The densities which are calculated by ORIGEN are used in BONAMI, ROLAIDS-CPM, and XSDRN for a new calculation of the neutron spectrum. Nuclides which are not on the AMPX-W library are updated with three-group spectral parameters.

When the fuel pin is considered as one lump, a constant power approximation can easily be used by ORIGEN, but when burnup in specific rings is considered, this poses a problem because the power profile in the fuel pin changes. This is solved by computing this power profile with XSDRN after each burnup step. The cross sections are not updated in this loop.

3.7   Assembly calculations with LWRWIMS

LWRWIMS is a reactor physics code which is specifically used for Light Water Reactor (LWR) assembly representation. It uses a multigroup cross section library with information about resonance integrals in a homogeneous medium. First, shielded cross sections are calculated for the specific problem with an equivalence relation [51,52]. Then, a multigroup collision probability calculation (PERSEUS) is done to collapse the cross sections to a few energy groups which are used by the two-dimensional transport code TWOTRAN (optionally). The TWOTRAN calculations result in two-group assembly-averaged cross sections for different soluble boron concentrations in the moderator, moderator temperatures, and fuel temperatures, which are suitable for use in PANTHER.

3.8 Safety transient analysis with PANTHER

PANTHER is a three-dimensional two-group diffusion code which has the capa-
bility to do safety transient analyses by calculating the time-dependent behaviour
of the neutron flux. Figure 3.3 shows the different functions which are executed
by PANTHER in a time step.
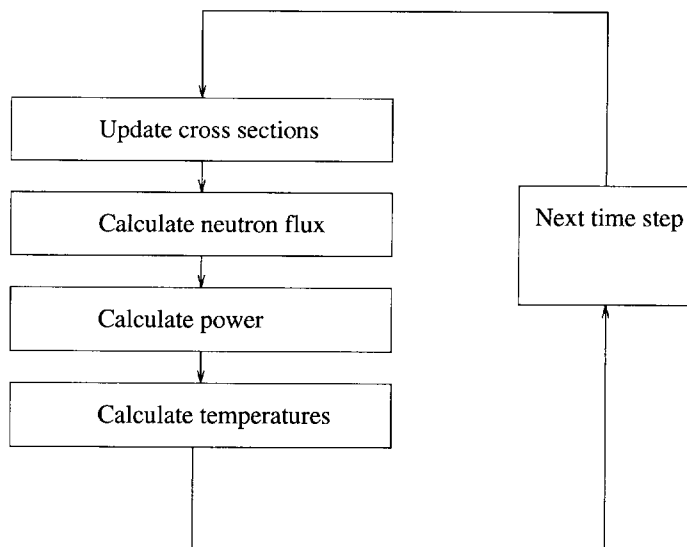
Figure 3.3: *Functions performed by PANTHER in a time step.*

First, PANTHER calculates the macroscopic cross sections for the specific
set of temperatures and densities from the input nuclear data, which have been
supplied by LWRWIMS. Then, it determines the time-dependent behaviour of the
neutron flux in a reactor. Before we turn our attention to these equations some
general remarks are made about the time-dependent behaviour of the neutron flux
in a nuclear reactor.

Part of the neutrons in a nuclear reactor do not arise directly from fission, but
are emitted by delayed neutron precursors. These nuclides are formed by fission.
Because of the delay in the emitting of neutrons, these neutrons are very important
for the control of a nuclear reactor [4,24,53]. Depending on their decay constant,
the precursors are divided in delayed neutron precursor groups for the calculations.

PANTHER uses a nodal scheme to solve the following time-dependent equa-

tion in two energy groups:

$$\frac{1}{v_1}\frac{\partial \phi_1}{\partial t} + L_1 + \Sigma_{r1}\phi_1 = \frac{1}{k_0}\sum_{g=1}^{2}\left[1 - \left(\sum_{d=1}^{D}\beta_{d,g}\right)\right](\nu\Sigma_f)_g\phi_g + \sum_{d=1}^{D}\lambda_d C_d \quad (3.13)$$

$$\frac{1}{v_2}\frac{\partial \phi_2}{\partial t} + L_2 + \Sigma_{r2}\phi_2 = \Sigma_{s_{1,2}}\phi_1, \quad (3.14)$$

where v_g is the neutron velocity in neutron energy group g, L_g is the leakage term for group g, Σ_{rg} is the removal (absorption + outscattering) cross section for group g, k_0 is only used to create an initially stationary situation, D is the number of delayed neutron groups, $\beta_{d,g}$ the delayed neutron fraction for delayed neutron precursor group d and neutron energy group g, λ_d the decay constant for delayed precursor group d, $(\nu\Sigma_f)_g$ the macroscopic neutron yield cross section in group g, C_d the precursor concentration for group d, and $\Sigma_{s_{1,2}}$ is the cross section for scattering from group 1 to group 2. The precursor concentration is given by:

$$\frac{\partial C_d}{\partial t} = \sum_{g}\beta_{d,g}\frac{\nu\Sigma_{f,g}\phi_g}{k_0} - \lambda_d C_d, \quad (3.15)$$

and the leakage term is given as:

$$L_g = \sum_{l}(CC_{g,l}^{l}\phi_{g,l} - CC_g^{l}\phi_g), \quad (3.16)$$

where l denotes the adjacent nodes, ϕ_g is the flux in the node under consideration, $\phi_{g,l}$ is the flux in the adjacent nodes, and CC are the coupling coefficients which are calculated in the analytical nodal scheme. First, the diffusion equations (equations 3.13 and 3.14 with $L_i = \nabla \bullet D_i\nabla\phi_i$) are integrated over the transverse directions in this nodal scheme. This is done for all three directions. Then, these equations are solved analytically by using a quadratic polynomial to represent the transverse leakage. An iterative procedure is used to find the neutron flux.

The neutron flux is used to calculate the total power density in different spatial nodes. Next, this power is used to calculate the new temperatures in a representative pin cell. The power distribution over the fuel pin has to be supplied by the user. This is done by defining the fraction of the total power which is generated in a specific concentric zone. For this purpose it is necessary to do calculations of the radial nuclide distributions in the fuel pin (chapter 7).

The fuel temperatures in the different zones of the fuel pin are obtained by solving the radial heat conduction equation for the fuel pin. Naturally, transport of heat from the cladding to the moderator, and the flow of the moderator through the reactor core are also modelled.

Finally, the temperatures are used to calculate new cross sections for the next time step. The effective fuel temperature in PANTHER is calculated as:

$$T_{\text{F,eff}} = \sum_i w_i T_i, \qquad (3.17)$$

with w_i the weight for the temperature T_i in the concentric ring i. These weights are input parameters, but there is no general rule on what they should be. As stated in chapter 1, the determination of these weights is the main topic of this work. ROLAIDS-CPM has been developed for this purpose. Chapter 6 deals with the determination of these weights for fresh UO_2 fuel. The fact that the effective fuel temperature is given in the form of equation 3.17 is not a strict demand, but it seems a very reasonable form. In this work we have limited ourselves to this expression.

Chapter 4

Definition and analysis of the fuel temperature coefficient[1]

The fuel temperature coefficient of reactivity is an important parameter for the evaluation of transients in thermal nuclear reactors, even though modern computer codes do not directly use it. This chapter deals with the question how to estimate the fuel temperature effect in a certain lattice in a reactor from the results of pin-cell calculations on an infinite lattice.

The fuel temperature coefficient is defined by equation 2.27. The fuel temperature effect of a lattice is often calculated by performing pin-cell calculations of the infinite multiplication factor at different fuel temperatures, and by using equation 2.27 with $k = k_\infty$. The question arises whether this fuel temperature coefficient of reactivity is a suitable measure for the fuel temperature effect of the lattice when it is situated in a reactor core.

Consider a region in a core with the lattice for which pin-cell calculations have been performed. It is possible to define a local multiplication factor (k') of a region in a core by taking account of the neutron leakage:

$$k' \equiv \frac{\text{neutron production rate}}{\text{neutron absorption rate} + \text{net neutron leakage rate}}, \qquad (4.1)$$

where the net neutron leakage rate is defined as the surface integrated difference between the outwards directed and the inwards directed neutron current density at the surface of the region. This net neutron leakage rate might have negative values.

Because $k' \approx 1$ in practical situations, the fuel temperature coefficient of the

---

[1] This chapter is an adapted version of reference 54

region is given by:

$$\alpha'_F = \frac{1}{k'^2} \frac{\partial k'}{\partial T_F} \approx \frac{1}{k'} \frac{\partial k'}{\partial T_F}. \tag{4.2}$$

We turn our attention to the pin-cell calculations. It is common practice in k-effective calculations to multiply the fission source by $\frac{1}{k}$ (equation 3.11). In this way an artificial balance between neutron production and neutron absorption is achieved. An artificial loss or source of neutrons with the neutron spectrum of the fission source is created.

Consider the neutron balance equation for the infinite lattice:

$$\frac{1}{k_\infty} F\phi = M\phi, \tag{4.3}$$

where F is the fission source operator, and M the migration and loss operator.

Define for a lattice at a certain fuel temperature:

$$k'' \equiv \frac{k_\infty}{\overline{k_\infty}}, \tag{4.4}$$

where k_∞ is the infinite multiplication factor at the selected temperature and $\overline{k_\infty}$ is the average k_∞ of calculations at different fuel temperatures. The value k'' will be close to 1, just like k'.

Substitution of equation (4.4) into equation (4.3) results in:

$$\begin{aligned}
\frac{1}{k''} F\phi &= \overline{k_\infty} M\phi \tag{4.5}\\
&= M\phi + (\overline{k_\infty} - 1) M\phi \\
&= M\phi + \frac{(\overline{k_\infty} - 1)}{k_\infty} F\phi \\
&= \left(M + \frac{(\overline{k_\infty} - 1)}{k_\infty} F \right) \phi.
\end{aligned}$$

With this k'' an about stationary situation is simulated where the net neutron leakage rate is given by $\frac{\overline{k_\infty} - 1}{k_\infty} F\phi$. This means that the actual net neutron leakage spectrum of a region in a core is approximated by the spectrum of the neutron fission source. The fuel temperature coefficient of such a region can then be approximated by:

$$\alpha'_F \approx \frac{1}{k'} \frac{\partial k'}{\partial T_F} \approx \frac{1}{k''} \frac{\partial k''}{\partial T_F} = \frac{1}{k_\infty} \frac{\partial k_\infty}{\partial T_F}. \tag{4.6}$$

So, instead of equation 2.27 a more appropriate definition of the fuel temperature coefficient with the value of k from pin-cell calculations appears to be:

$$\alpha_F^* \equiv \frac{1}{k} \frac{\partial k}{\partial T_F}, \qquad (4.7)$$

where $k = k_\infty$ for calculations on an infinite lattice.

This definition of the fuel temperature coefficient is the same as the one that is used in many textbooks [24,30,55,56]. But in these textbooks the definition is based on the fact that the effective multiplication factor is about equal to 1 for practical cases. However, this might not be the case for k from pin-cell calculations. The definition in equation 4.7 is based on the fact that the local k-effective k' is about equal to 1 for practical cases, and on the approximation that the change of k-effective with the fuel temperature for lattices with the actual net neutron leakage spectrum is the same as for lattices with an artificial net neutron leakage spectrum described by the neutron spectrum of the fission source.

This last approximation is tested by doing some calculations on lattices which are characteristic for a PWR.

4.1 Calculations

Mosteller et al. [39] presented a calculational benchmark for the Doppler coefficient of reactivity in an infinite array of infinitely long pin cells which are characteristic for a PWR at beginning of life (BOL). Five different enrichments of uranium have been used, varying from 0.711 weight (wt) % to 3.9 wt %. The calculations of the infinite multiplication factor k_∞ have been done for one fuel enrichment at the time and for a soluble boron concentration of 1400 ppm (parts per million; the ^{10}B-density is $10.21366 \cdot 10^{-6}$ (b cm)$^{-1}$). The calculations of k_∞ have been done for two different fuel temperatures, 600 K and 900 K, corresponding with hot zero power (HZP) and hot full power (HFP), respectively. Since the nuclide densities have been varied with the fuel temperature in this calculational benchmark, the term fuel temperature coefficient of reactivity is used throughout this chapter.

The coefficients α_F^* for the calculational benchmark have been deduced from the MCNP results of Mosteller et al. [39]. The coefficients α_F and α_F^*, which are presented in table 4.1 (in which 1 pcm = 10^{-5}), have been calculated according to:

$$\alpha_F = \frac{1}{k_{hot} k_{cold}} \frac{k_{hot} - k_{cold}}{\Delta T_F}, \qquad (4.8)$$

$$\alpha_F^* = \frac{2}{k_{hot} + k_{cold}} \frac{k_{hot} - k_{cold}}{\Delta T_F}, \qquad (4.9)$$

Table 4.1: *Fuel temperature coefficients of reactivity for calculational benchmark deduced from reference 39 (± 1 standard deviation σ).*

Fuel enrichment (wt %)	k_{cold}	k_{hot}	α_F (pcm/K)	α_F^* (pcm/K)
0.711	0.6638 ± 0.0006	0.6567 ± 0.0008	-5.4 ± 0.8	-3.6 ± 0.7
1.6	0.9581 ± 0.0006	0.9484 ± 0.0006	-3.6 ± 0.3	-3.4 ± 0.4
2.4	1.0961 ± 0.0007	1.0864 ± 0.0007	-2.7 ± 0.3	-2.9 ± 0.4
3.1	1.1747 ± 0.0007	1.1641 ± 0.0006	-2.6 ± 0.2	-3.0 ± 0.4
3.9	1.2379 ± 0.0006	1.2271 ± 0.0006	-2.4 ± 0.2	-2.9 ± 0.3

where k_{hot} and k_{cold} are the multiplication factors at 900 K and 600 K, respectively. An important result is that α_F^* is much less dependent on the fuel enrichment than α_F.

The accuracy of α_F^* is tested by comparing the fuel temperature coefficients for the benchmark problems with the fuel temperature coefficients of lattices which have been made about critical. This has been done by either a buckling correction or an adjustment of the ^{10}B-concentration in the moderator. Using the about-critical lattices, the neutron balance in a core-region with the relevant lattice is simulated. The buckling correction simulates a net leakage into or out of the region with the neutron spectrum of the transverse leakage rate in the pin-cell calculations. This is quite a realistic estimate for the net neutron leakage spectrum between adjacent regions in a reactor core, and for the leakage spectrum out of the core. The change in the ^{10}B-concentration simulates a neutron leakage into or out of the region with the neutron spectrum of the absorption rate in ^{10}B. This is not realistic because of the seemingly large net leakage of thermal neutrons. In spite of this, the case is interesting because the influence of boration on the fuel temperature effect is calculated. For the case with 2.4 wt % enriched fuel the spectra of the simulated net neutron leakage rates belonging to the different introduced changes are given in figure 4.1. It should be noted that $\frac{1}{k}$ times the fission source is normalized to 1 s^{-1}.

The calculational method is shortly described in section 3.5. For the calculations in this chapter a 219-group cross section library [57] is used. Further details on the calculations are given in reference 58.

Table 4.2 shows the results of our calculations. The fuel temperature coefficients for the benchmark problems are presented together with the fuel temperature coefficients of the lattices which have been made about critical by either a buckling correction or an adjustment of the ^{10}B-concentration. For these adjusted lattices only α_F^* is given because this is about equal to α_F.
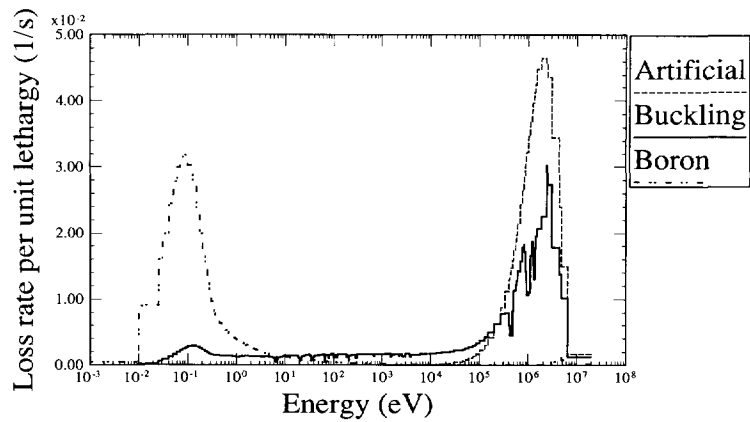
Figure 4.1: *Simulated net neutron leakage spectra for the 2.4 wt % enriched fuel at 600 K. The spectra are given for the original benchmark problems (artificial) and for the problems with the about-critical lattices (buckling, boron).*

Table 4.2: *Fuel temperature coefficients of reactivity for the benchmark problems and of the about-critical lattices as calculated by XSDRN.*

Fuel enrichment (wt %)	Benchmark problem α_F (pcm/K)	Benchmark problem α_F^* (pcm/K)	Buckling correction α_F^* (pcm/K)	^{10}B adjustment α_F^* (pcm/K)
0.711	-5.83	-3.86		
1.6	-3.72	-3.55	-3.54	-3.48
2.4	-3.08	-3.36	-3.39	-3.50
3.1	-2.77	-3.25	-3.29	-3.47
3.9	-2.64	-3.26	-3.27	-3.52

The fuel temperature coefficients of the lattices which have been made about critical by a buckling correction are about the same as α_F^* for the benchmark problems. However, the coefficients α_F for the benchmark problems differ a lot from these fuel temperature coefficients. So, α_F^* as defined by equation (4.7) gives a much better idea of the fuel temperature effect in a lattice than α_F as defined by equation (2.27), when the calculated k is not about equal to 1, as is often the case for an infinite lattice.

The fuel temperature coefficients of reactivity of the lattices which have been made about critical by adjusting the ^{10}B-concentration differ only little from α_F^* for the benchmark problems. So, the fuel temperature coefficient of reactivity α_F^* is almost independent of the ^{10}B-concentration. It should be noted that we used unrealistic large adjustments of the ^{10}B-concentration to make the lattices about critical. We quantify our results in more detail in the next section.

4.2   Analysis of fuel temperature coefficients

Consider the following four-factor formula:

$$k = \eta f a \epsilon^*, \qquad (4.10)$$

where η and f have the same meaning as in equation 2.25, a is the thermal absorption rate in the system normalized to $\frac{1}{k}$ times the fission source, and ϵ^* the non-thermal fission factor. This non-thermal fission factor is the total neutron production rate by fissions divided by the neutron production rate by thermal fissions. The use of ϵ^* is chosen to distinguish the name non-thermal fission factor from the standard name fast fission factor. In an infinite lattice the factor a is about the same as the escape probability to the thermal energy range. The difference is caused by nuclear reactions such as (n,2n).

Equation (4.10) is used because these four factors can be calculated from the XSDRN-output. The different factors for the benchmark problems are given in table 4.3. The energy boundary between the thermal and non-thermal group is at 3.05 eV.

The fuel temperature coefficient of reactivity α_F^* is given by:

$$\alpha_F^* = \frac{1}{k}\frac{\partial k}{\partial T_F} = \frac{1}{\eta}\frac{\partial \eta}{\partial T_F} + \frac{1}{f}\frac{\partial f}{\partial T_F} + \frac{1}{a}\frac{\partial a}{\partial T_F} + \frac{1}{\epsilon^*}\frac{\partial \epsilon^*}{\partial T_F}. \qquad (4.11)$$

The different terms in equation (4.11) for the benchmark problems are given in table 4.4. They are calculated analogously to equation (4.9).

The table shows that the temperature dependence of the a factor is the main contribution to the fuel temperature coefficient of reactivity. This is expected because of the Doppler effect.

Table 4.3: *The different factors in equation (4.10) for the benchmark problems at T=600 K.*

Enrichment (wt %)	η	f	a	ϵ^*	k
0.711	1.2824	0.6005	0.6965	1.2422	0.6663
1.6	1.6202	0.7191	0.6755	1.2198	0.9600
2.4	1.7420	0.7750	0.6580	1.2357	1.0977
3.1	1.8029	0.8067	0.6436	1.2559	1.1756
3.9	1.8486	0.8324	0.6282	1.2817	1.2390

Table 4.4: *The different terms in equation (4.11) for the infinite lattices of the calculational benchmark.*

Enrichment (wt %)	$(\overline{\eta})^{-1}\frac{\Delta\eta}{\Delta T_F}$ (pcm/K)	$(\overline{f})^{-1}\frac{\Delta f}{\Delta T_F}$ (pcm/K)	$(\overline{a})^{-1}\frac{\Delta a}{\Delta T_F}$ (pcm/K)	$(\overline{\epsilon^*})^{-1}\frac{\Delta\epsilon^*}{\Delta T_F}$ (pcm/K)	$(\overline{k})^{-1}\frac{\Delta k}{\Delta T_F}$ (pcm/K)
0.711	0.00	-1.11	-3.00	0.25	-3.86
1.6	0.01	-0.75	-2.93	0.12	-3.55
2.4	0.01	-0.58	-2.89	0.10	-3.36
3.1	0.01	-0.49	-2.87	0.10	-3.25
3.9	-0.06	-0.40	-2.98	0.19	-3.26

It should be noted that the temperature dependences are influenced by the change of the nuclide densities with fuel temperature. The calculations for the lattices of the calculational benchmark have also been done with fixed nuclide densities (taken at $T_F = 900K$).

Figure 4.2 shows α_F and α_F^* for the benchmark problems and α_F^* for the calculation of the benchmark problems with fixed nuclide densities. With fixed nuclide densities the coefficients α_F^* are less negative, especially for low enrichments. The dependence of α_F^* on the fuel enrichment almost disappears. The coefficients α_F^* are now in fact the Doppler coefficients of reactivity.
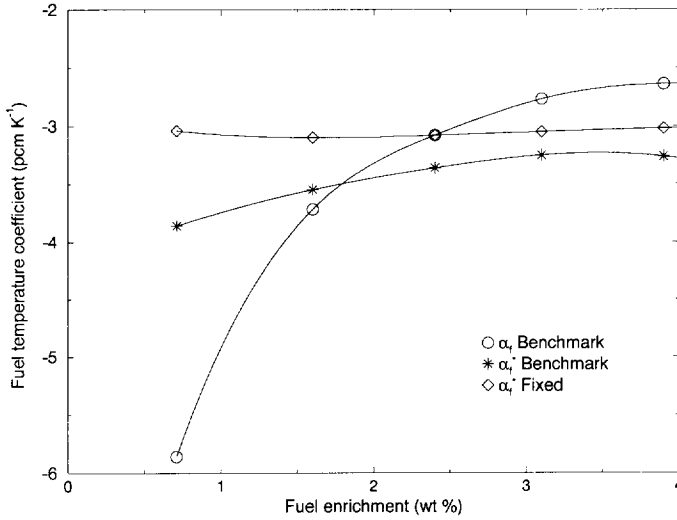
Figure 4.2: *Fuel temperature coefficients α_F and α_F^* for the benchmark problems (benchmark) and α_F^* for the benchmark problems with fixed nuclide densities (fixed).*

Table 4.5 shows the different terms in equation 4.11 for the benchmark problem with fixed nuclide densities. Only the factors a and ϵ^* show a significant temperature dependence. The dependence of ϵ^* on the fuel temperature is not obvious. This term is analysed in detail in the rest of this section. Consider:

$$\frac{1}{\epsilon^*}\frac{\partial \epsilon^*}{\partial T_f} = \frac{n_{\text{prod}}}{n_{\text{prod}} + t_{\text{prod}}}\left(\frac{1}{n_{\text{prod}}}\frac{\partial n_{\text{prod}}}{\partial T_f} - \frac{1}{t_{\text{prod}}}\frac{\partial t_{\text{prod}}}{\partial T_f}\right), \qquad (4.12)$$

where t_{prod} is the neutron production rate by thermal fissions and n_{prod} is the neutron production rate by non-thermal fissions. The sum of these two production rates normalized to the total absorption rate of unity (including leakage for a

Table 4.5: *The different terms in equation (4.11) for the benchmark problems with fixed nuclide densities.*

Enrichment (wt %)	$(\overline{\eta})^{-1}\frac{\Delta\eta}{\Delta T_F}$ (pcm/K)	$(\overline{f})^{-1}\frac{\Delta f}{\Delta T_F}$ (pcm/K)	$(\overline{a})^{-1}\frac{\Delta a}{\Delta T_F}$ (pcm/K)	$(\overline{\epsilon^*})^{-1}\frac{\Delta\epsilon^*}{\Delta T_F}$ (pcm/K)	$(\overline{k})^{-1}\frac{\Delta k}{\Delta T_F}$ (pcm/K)
0.711	-0.03	-0.02	-3.56	0.57	-3.04
1.6	-0.02	-0.01	-3.56	0.49	-3.10
2.4	-0.02	-0.01	-3.58	0.52	-3.08
3.1	-0.02	0.00	-3.61	0.58	-3.05
3.9	-0.02	0.00	-3.65	0.66	-3.02

Table 4.6: *The different terms in equation (4.12) for the benchmark problems with fixed nuclide densities.*

Enrichment (wt %)	$\overline{n}_{prod}$	$\overline{t}_{prod}$	$\frac{\overline{n}_{prod}}{(\overline{n}_{prod}+\overline{t}_{prod})}$	$(\overline{n}_{prod})^{-1}\frac{\Delta n_{prod}}{\Delta T_f}$ (pcm/K^{-1})	$(\overline{t}_{prod})^{-1}\frac{\Delta t_{prod}}{\Delta T_f}$ (pcm/K^{-1})
0.711	0.1290	0.5327	0.1949	-0.68	-3.61
1.6	0.1717	0.7826	0.1799	-0.87	-3.59
2.4	0.2078	0.8839	0.1905	-0.85	-3.60
3.1	0.2378	0.9318	0.2033	-0.78	-3.63
3.9	0.2705	0.9620	0.2194	-0.67	-3.67

finite lattice) is k. Table 4.6 shows the terms in equation 4.12 for the benchmark problems with fixed nuclide densities.

The term $\frac{1}{t_{prod}}\frac{\partial t_{prod}}{\partial T}_{mf}$ is equal to $\frac{1}{\eta}\frac{\partial\eta}{\partial T_f}+\frac{1}{f}\frac{\partial f}{\partial T_f}+\frac{1}{a}\frac{\partial a}{\partial T_f}$ from table 4.5. The term $\frac{1}{n_{prod}}\frac{\partial n_{prod}}{\partial T_f}$ is analysed by looking at the different isotopes of uranium:

$$\frac{1}{n_{prod}}\frac{\partial n_{prod}}{\partial T_f} = \frac{n^5_{prod}}{n_{prod}}\frac{1}{n^5_{prod}}\frac{\partial n^5_{prod}}{\partial T_f} + \frac{n^8_{prod}}{n_{prod}}\frac{1}{n^8_{prod}}\frac{\partial n^8_{prod}}{\partial T_f}, \qquad (4.13)$$

where n^5_{prod} is the neutron production rate by non-thermal fissions of ^{235}U and n^8_{prod} is the neutron production rate by non-thermal fissions of ^{238}U. The temperature dependence of n^8_{prod} appears to be negligibly small. So, only the first term on the right-hand side in equation (4.13) is analysed in table 4.7.

The term $\frac{1}{n^5_{prod}}\frac{\partial n^5_{prod}}{\partial T_f}$ is negative because of the increasing parasitic absorption

Table 4.7: *Analysis of* $\dfrac{n^5_{\text{prod}}}{n_{\text{prod}}} \dfrac{1}{n^5_{\text{prod}}} \dfrac{\partial n^5_{\text{prod}}}{\partial T_f}$ *for the benchmark problems with fixed nuclide densities.*

Enrichment (wt %)	$\overline{n^5_{\text{prod}}}$	$\overline{(n^5_{\text{prod}})^{-1} \frac{\Delta n^5_{\text{prod}}}{\Delta T_f}}$ (pcm/K)	$\overline{n^8_{\text{prod}}}$	$\overline{(n^5_{\text{prod}})(n_{\text{prod}})^{-1}}$
0.711	0.0371	-2.37	0.0919	0.2876
1.6	0.0806	-1.86	0.0911	0.4696
2.4	0.1174	-1.51	0.0903	0.5652
3.1	0.1481	-1.25	0.0897	0.6228
3.9	0.1815	-1.00	0.0890	0.6711

in ^{238}U with increasing temperature. It becomes less negative when the fuel enrichment increases. This behaviour is caused by the increased shielding of the resonances in ^{235}U which causes a larger Doppler effect.

The term $\dfrac{1}{n_{\text{prod}}} \dfrac{\partial n_{\text{prod}}}{\partial T_f}$ (table 4.6) does not monotonously increase with the fuel enrichment because of the multiplication of $\dfrac{1}{n^5_{\text{prod}}} \dfrac{\partial n^5_{\text{prod}}}{\partial T_f}$ by $\dfrac{n^5_{prod}}{n_{prod}}$. This last factor increases with the fuel enrichment.

The dependence of $\epsilon^* = \dfrac{n_{\text{prod}} + t_{\text{prod}}}{t_{\text{prod}}}$ on the fuel enrichment (see table 4.3) can also be understood from tables 4.6 and 4.7. The production rate n^5_{prod} is much more dependent on the enrichment than t_{prod}, while n^8_{prod} is not. This means that for very low enrichments ϵ^* decreases with the fuel enrichment, while for higher enrichments, when n^5_{prod} is more important, ϵ^* increases with the fuel enrichment. The same analysis can easily be done for the dependence of $\dfrac{n_{\text{prod}}}{n_{\text{prod}} + t_{\text{prod}}}$ on the fuel enrichment.

4.3   Conclusions

When pin-cell calculations in infinite lattices are performed, attention should be paid to the definition of the fuel temperature coefficient of reactivity. The fuel temperature coefficient α_F^* $(= \dfrac{1}{k} \dfrac{\partial k}{\partial T_F})$ gives a much better idea of the fuel temperature effect in a lattice than the fuel temperature coefficient α_F $(= \dfrac{1}{k^2} \dfrac{\partial k}{\partial T_F})$. The accuracy of α_F^* depends of course on the actual net neutron leakage spectrum of the region in a reactor core with the lattice that is considered. For the calculational benchmark presented by Mosteller et al. [39] the accuracy of α_F^* is very good

when the net neutron leakage spectrum can be described by a buckling correction, which seems to be very reasonable.

The fuel temperature coefficient of reactivity α_F^* shows that the fuel temperature effect is hardly dependent on the fuel enrichment in the calculational benchmark. The fuel temperature effect is also hardly dependent on the ^{10}B-concentration. These dependences become even less when the nuclide densities are not varied with fuel temperature.

The calculation of different contributions to the fuel temperature coefficient of reactivity is a powerful tool in the analysis of fuel temperature coefficients. An important advantage of calculating different contributions to the fuel temperature coefficient of reactivity is the fact that sources of discrepancies between different codes and/or data can be found more easily. If necessary, the calculation of different contributions can be extended by looking for example to escape probabilities for specific energy groups.

It is obvious that the Doppler effect can very well be studied by considering only a limited energy range: the resolved resonance energy range. An important advantage is that no iterations are necessary to determine k-effective, which speeds up the calculations. Besides, the results are not influenced by second-order effects such as variations in the non-thermal fission factor. Because we concentrate on the Doppler effect, the nuclide densities are kept constant in the calculations presented in the next chapters.

Chapter 5

Verification of resonance absorption calculations [1]

5.1 Introduction

For accurate predictions of temperature effects on resonance absorption in a fuel pin, it is necessary to describe in detail the radial variations of the fuel temperature, the nuclide densities, and the resonance shielding. Because no experimental data are available on the detailed space and energy dependence of resonance absorption in a fuel pin, detailed reference calculations are important for the validation of ROLAIDS-CPM. These reference calculations have been done with the Monte Carlo code MCNP (version 4.2). Although MCNP is used as a reference code, one must be aware of the limitations of this code. These limitations are discussed in section 3.3. Actually, not validation but verification is done by comparing Monte Carlo results with deterministic results. The verification of the resonance absorption calculations with ROLAIDS-CPM is the main goal of this chapter.

We have performed a calculational benchmark which was defined by Tellier *et al.* [38]. This benchmark involves the calculation of resonance absorption by ^{238}U between approximately 2.8 eV and 1.5 keV in a typical PWR pin-cell geometry with cylindrical outer boundary (Wigner-Seitz approximation). The neutrons are assumed to come from a lethargy-independent neutron source between approximately 2 keV and 3.5 keV. The absorption is studied in the relevant 42 groups of the XMAS 172-group energy mesh between 2.8 eV and 1.5 keV and in 10 concentric rings in the fuel pin which have equal volumes. Tellier *et al.* used the Monte Carlo code TRIPOLI for the reference results. The dimensions of the

---

[1] This chapter is an adapted version of reference 59

Table 5.1: *Geometrical dimensions of the pin cell.*

Radius fuel	0.40950 cm
Outer radius cladding	0.47436 cm
Equivalent cell radius	0.71354 cm

Table 5.2: *Nuclide densities.*

Isotope	Region	Density $(10^{24}$ atom/cm$^3)$
^{238}U	Fuel	0.021758
^{16}O	Fuel	0.044925
^{27}Al	Cladding	0.039220
^{16}O	Moderator	0.023857
^{1}H	Moderator	0.047714

pin cell are listed in table 5.1, and the densities of the nuclides are given in table 5.2.

There are several reasons to calculate reference results ourselves with the Monte Carlo code MCNP. First, the same data can be, and have been used in all our calculations. This does not only mean that we have used the same nuclear data file (JEF2) but also that we have processed these data with NJOY (version 91.38) and NSLINK (version 4.1) in such a way that, if possible, the same processed data have been used (see figure 3.1). Secondly, the number of histories can be varied in the Monte Carlo calculations. The total absorption in the TRIPOLI results has a standard deviation of about 0.7 %. This is too large to make a detailed comparison between different codes. The differences between the codes should not get lost in statistics, otherwise one cannot get an idea of the aberration introduced by the calculational method.

We have also studied the absorption in a high-energy group between 1.5 keV and 3.35 keV, which comprises 3 groups from the XMAS energy mesh.

Important for our calculations is that both MCNP and ROLAIDS-CPM approximate the square pin cell by a cylindrical pin cell with isotropic reflection at the outer boundary (Wigner-Seitz assumption).

Basic assumptions which are made in ROLAIDS-CPM are the assumptions of spatially flat and isotropic scattering sources in the different zones. The assumption of spatially flat scattering sources can be examined by varying the number of zones, but the assumption of isotropic scattering sources cannot be examined directly.

ROLAIDS-CPM can also be used to calculate effective cross sections for the

multigroup discrete ordinates code XSDRN. So, by varying the Legendre order of scattering in the multigroup transport calculation the influence of anisotropic scattering sources can be examined. Besides, and more importantly, the ROLAIDS-CPM/XSDRN calculations enable us to establish the accuracy of multigroup transport calculations.

5.2   MCNP results

A private MCNP version (based on version 4.2) which is able to treat isotropic reflection at the cylindrical boundary has been used. The number of histories in the reference MCNP calculation is very high to ensure that the differences between the results of different codes do not get lost in statistics. The number of histories in the reference calculation is about 30 million. The reference results are given in reference 60. Some results are presented in this chapter when comparisons are made with results from other codes. The total absorption by ^{238}U between 2.7679 eV and 3.3546 keV normalized to 1 source neutron is 0.21178 ± 0.00006 (1 σ).

The influence of the Wigner-Seitz approximation has been investigated by a comparison of the reference results with the results of a MCNP calculation for a square cell with specular reflection at the boundaries. The pitch of the square cell is 1.26472 cm. The total absorption by ^{238}U reduces to 0.2091 ± 0.0001. Considering the escape probability p, which is simply 1 minus the total absorption, the difference is about 0.34 %. When this effect of the Wigner-Seitz approximation on the effective multiplication factor is estimated ($\frac{\Delta k}{k} \approx \frac{\Delta p}{p}$), one gets a value of about 340 pcm, which is quite large. This difference is certainly not negligible and should be taken into account when detailed calculations are performed on a cylindrical pin cell. The fact that we can quantify the difference is due to the high statistical accuracy in our results.

Figure 5.1 shows the spectrum of the difference between the absorption by ^{238}U in a square cell and the absorption by ^{238}U in a cylindrical cell.

It is clear that the difference is mainly caused by the high resonances of ^{238}U (see figure 2.1). The fact that the absorption in the cylindrical pin cell is larger can qualitatively be understood by noting that the inwards directed flux at the boundary of an imaginary cylinder in the square lattice geometry is not isotropic because of the Dancoff effect (section 2.5.3). On the average the neutron current near the resonance energies is less directed towards the fuel than a cosine current. This qualitative argument implies that the Wigner-Seitz approximation influences the results more when the Dancoff effect has a larger impact (tightly packed lattices). The Wigner-Seitz assumption is not expected to influence the Doppler effect calculations very much because most of the neutrons which cause the difference in figure 5.1 are absorbed anyway, independent of fuel temperature.
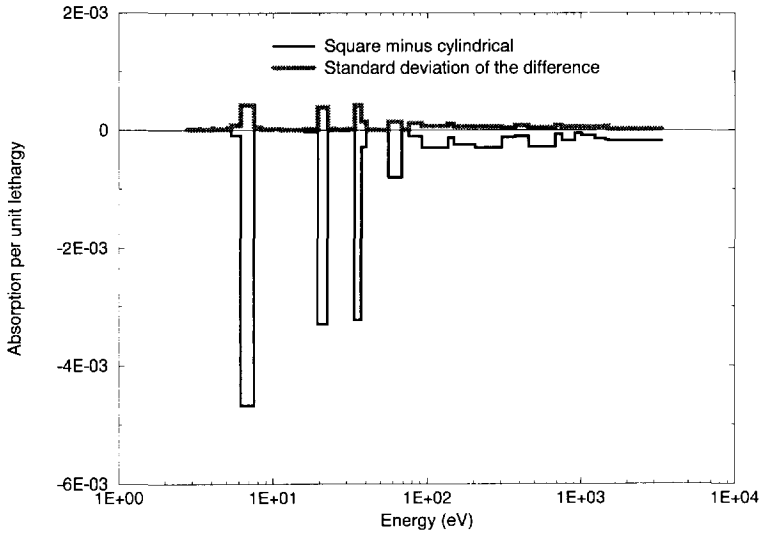
Figure 5.1: *Absorption by* ^{238}U; *difference between the square pin cell and the cylindrical cell.*

5.3   ROLAIDS-CPM results

The standard ROLAIDS-CPM calculations (version 93.15) have been done with 10 zones in the fuel with equal volumes (1 zone for each ring), 1 zone in the cladding, and 1 zone in the moderator. Table 5.3 shows the absorption by ^{238}U in the different rings for the standard ROLAIDS-CPM calculation and for the reference MCNP calculation.

The absorption in the standard ROLAIDS-CPM calculations is somewhat less than in the reference MCNP calculation. The total difference in absorption is about $4 \cdot 10^{-4}$. Although the difference is statistically significant, it is only 0.2 % of the total absorption. This leads to 50 pcm difference in a k-effective calculation, which is small. Therefore, it can be concluded that ROLAIDS-CPM is a suitable code for these resonance absorption calculations. Nevertheless, below we will have a closer look at the remaining differences.

ROLAIDS-CPM assumes spatially flat sources in the different zones. The influence of this assumption can easily be examined by taking more zones into account. The spatial mesh in the fuel is already very fine, but because the flux at the resonance energies sharply decreases in the outer region of the fuel pin, the spatial mesh might not be fine enough in this outer area. So, the outer ring

Table 5.3: *Absorption by* ^{238}U *in the different rings; comparison between MCNP and ROLAIDS-CPM.*

Ring (inner to outer)	ROLAIDS-CPM Standard case	MCNP	
		Reference	Standard deviation
1	$1.5763 \cdot 10^{-2}$	$1.582 \cdot 10^{-2}$	$1 \cdot 10^{-5}$
2	$1.6106 \cdot 10^{-2}$	$1.617 \cdot 10^{-2}$	$1 \cdot 10^{-5}$
3	$1.6509 \cdot 10^{-2}$	$1.657 \cdot 10^{-2}$	$1 \cdot 10^{-5}$
4	$1.6991 \cdot 10^{-2}$	$1.704 \cdot 10^{-2}$	$1 \cdot 10^{-5}$
5	$1.7586 \cdot 10^{-2}$	$1.762 \cdot 10^{-2}$	$1 \cdot 10^{-5}$
6	$1.8351 \cdot 10^{-2}$	$1.842 \cdot 10^{-2}$	$1 \cdot 10^{-5}$
7	$1.9409 \cdot 10^{-2}$	$1.946 \cdot 10^{-2}$	$1 \cdot 10^{-5}$
8	$2.1065 \cdot 10^{-2}$	$2.108 \cdot 10^{-2}$	$1 \cdot 10^{-5}$
9	$2.4543 \cdot 10^{-2}$	$2.448 \cdot 10^{-2}$	$1 \cdot 10^{-5}$
10	$4.5056 \cdot 10^{-2}$	$4.513 \cdot 10^{-2}$	$3 \cdot 10^{-5}$
Total	$2.1138 \cdot 10^{-1}$	$2.1178 \cdot 10^{-1}$	$6 \cdot 10^{-5}$

of the fuel pin has been divided into more zones. Figure 5.2 shows the spectral difference in the absorption by ^{238}U in the whole fuel pin between MCNP results and ROLAIDS-CPM results for two different numbers of zones in the outer ring. It can be seen that the absorption in the wide resonances decreases with the number of zones. Especially for the wide resonances with a large scattering cross section the spatial distribution of the zones in the fuel is important.

The difference in the lowest-energy group is due to a problem with the lower-energy boundary ELO, which has been solved in a newer version of ROLAIDS-CPM (94.18). The flux calculated with previous versions (as in this thesis) is wrong below the energy: $\frac{ELO}{\alpha_{min}}$, where α_{min} is α for the lightest nuclide in the problem (apart from ^{1}H). This error does not influence the results in the next chapters, because ELO is such that the flux is correct in the energy range under consideration.

A further refinement of the spatial mesh hardly influences the results. The assumption of isotropic sources will be dealt with in the next section.

5.4   XSDRN results

XSDRN calculations (SCALE version 4.1) have been done to test the performance of our multigroup transport calculations. In the XSDRN calculations the spatial mesh consists of the same 10 intervals in the fuel as in the standard ROLAIDS-
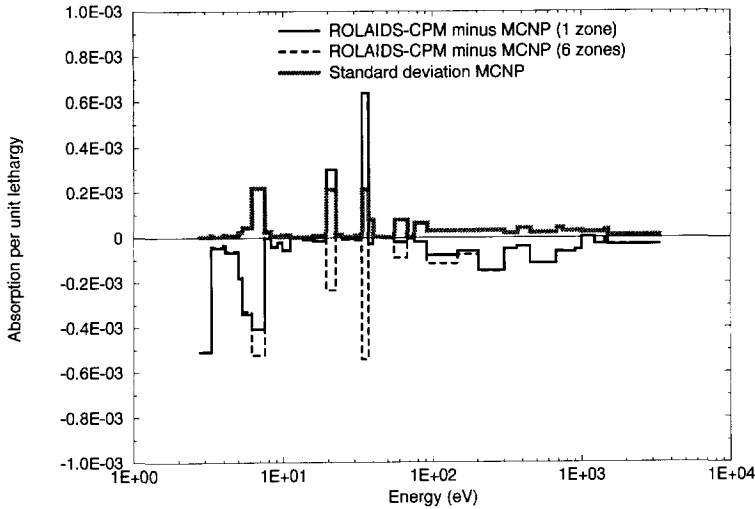
Figure 5.2: *Absorption by ^{238}U; difference between ROLAIDS-CPM and MCNP for different numbers of zones in the outer ring of the fuel.*

CPM calculation, 1 interval in the cladding, and 8 intervals in the moderator which are equidistant. The order of the angular quadrature is 32. The only parameter that has been varied is the Legendre order of scattering (0-3) because isotropic scattering sources are assumed by ROLAIDS-CPM and we want to know the effect of this assumption.

The calculations have initially been done with a multigroup library for the relevant 45 groups from the XMAS 172-group energy mesh. First, the Nordheim integral treatment [50] has been used to calculate effective group cross sections with NITAWL (SCALE version 4.1). However, because NITAWL calculates space-independent group-averaged cross sections, the distribution of the absorption over the fuel pin is calculated completely wrong. This is shown in table 5.4. The table also shows that the results are much better when ROLAIDS-CPM is used to calculate group-averaged cross sections for each ring. So, we will concentrate on the results with ROLAIDS-CPM/XSDRN.

As can be seen in table 5.4, the total absorption by ^{238}U in the ROLAIDS-CPM/XSDRN results is too high. Figure 5.3 shows that the difference with the reference MCNP calculation is mainly at the lower-energy range. Also some difference can be seen in the highest-energy group but this is caused by the fact that ROLAIDS-CPM has only calculated effective cross sections and transfer matrices for ^{238}U. The effective cross sections and transfer matrices for the other

Table 5.4: *Absorption by* ^{238}U *in the different rings; comparison between XSDRN with a 45-group energy mesh (NITAWL or ROLAIDS-CPM) and MCNP.*

Ring (inner to outer)	NITAWL/ XSDRN(45)	ROLAIDS-CPM/ XSDRN(45)	MCNP	
			Reference	Standard deviation
1	$2.0491 \cdot 10^{-2}$	$1.6366 \cdot 10^{-2}$	$1.582 \cdot 10^{-2}$	$1 \cdot 10^{-5}$
2	$2.0652 \cdot 10^{-2}$	$1.6695 \cdot 10^{-2}$	$1.617 \cdot 10^{-2}$	$1 \cdot 10^{-5}$
3	$2.0831 \cdot 10^{-2}$	$1.7083 \cdot 10^{-2}$	$1.657 \cdot 10^{-2}$	$1 \cdot 10^{-5}$
4	$2.1019 \cdot 10^{-2}$	$1.7546 \cdot 10^{-2}$	$1.704 \cdot 10^{-2}$	$1 \cdot 10^{-5}$
5	$2.1219 \cdot 10^{-2}$	$1.8114 \cdot 10^{-2}$	$1.762 \cdot 10^{-2}$	$1 \cdot 10^{-5}$
6	$2.1437 \cdot 10^{-2}$	$1.8848 \cdot 10^{-2}$	$1.842 \cdot 10^{-2}$	$1 \cdot 10^{-5}$
7	$2.1674 \cdot 10^{-2}$	$1.9853 \cdot 10^{-2}$	$1.946 \cdot 10^{-2}$	$1 \cdot 10^{-5}$
8	$2.1944 \cdot 10^{-2}$	$2.1440 \cdot 10^{-2}$	$2.108 \cdot 10^{-2}$	$1 \cdot 10^{-5}$
9	$2.2225 \cdot 10^{-2}$	$2.4724 \cdot 10^{-2}$	$2.448 \cdot 10^{-2}$	$1 \cdot 10^{-5}$
10	$2.2663 \cdot 10^{-2}$	$4.4805 \cdot 10^{-2}$	$4.513 \cdot 10^{-2}$	$3 \cdot 10^{-5}$
Total	$2.1418 \cdot 10^{-1}$	$2.1547 \cdot 10^{-1}$	$2.1178 \cdot 10^{-1}$	$6 \cdot 10^{-5}$

nuclides have been obtained by NJOY, using a 1/E weighting function. Because of the introduction of the neutron source, the flux in the higher-energy range does not resemble a 1/E flux. Therefore, the effective cross sections and especially the transfer matrices should be calculated by weighting them with the calculated flux from ROLAIDS-CPM.

From the considerations on group condensation given in section 3.4 one may suspect that the energy mesh is too coarse in the low-energy range to obtain very accurate results. Therefore, the 45-group energy mesh has been refined and the calculations have been repeated for a 107-group energy mesh which is obtained by inserting extra group boundaries in the energy ranges around the 4 lowest resonances (6.1601 eV - 7.5240 eV, 19.455 eV - 22.603 eV, 33.720 eV - 37.266 eV, and 55.595 eV - 67.904 eV). In these ranges the width of a group is 0.05 eV.

The calculations in the 107-group energy mesh have been done with effective cross sections calculated by ROLAIDS-CPM for each nuclide. The total absorption in the fuel is 0.21199, which is very close to the reference MCNP result. The spectrum of the difference in absorption between the ROLAIDS-CPM/XSDRN results and the reference MCNP results is given in figure 5.4. This difference can only be shown in the 43-group energy mesh, because the MCNP results have been obtained for this energy mesh.

It is clear that the accuracy of multigroup calculations with the discrete ordinates code XSDRN is strongly influenced by the energy mesh. However, routine
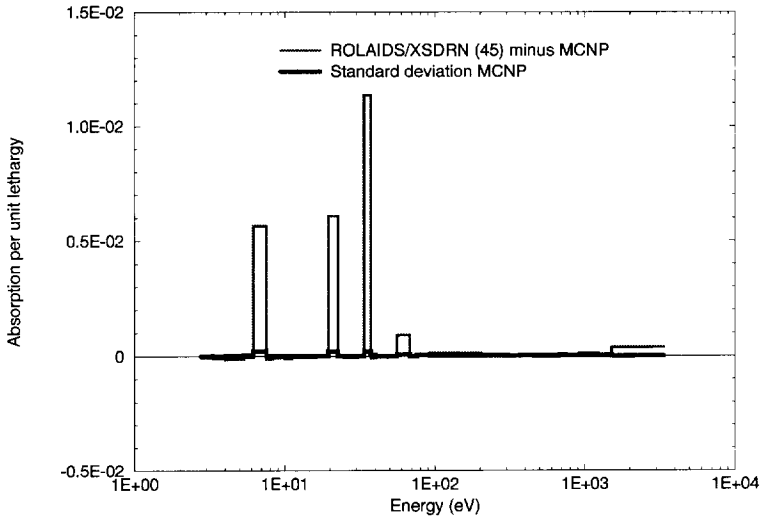
Figure 5.3: *Absorption in the fuel; difference between ROLAIDS-CPM/XSDRN with a 45-group energy mesh and MCNP.*
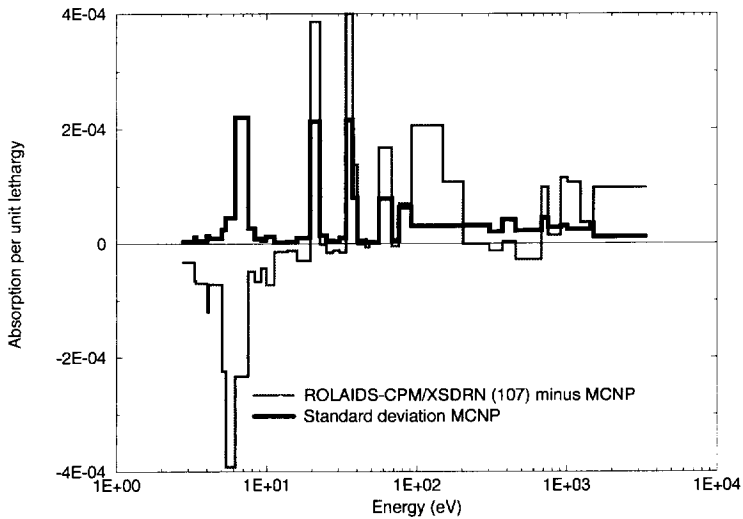

Figure 5.4: *Absorption in the fuel; difference between ROLAIDS-CPM/XSDRN results with a 107-group energy mesh and reference MCNP results.*

reactor physics calculations are done with a fixed broad energy mesh. So, to establish the accuracy of such calculations one should know the aberration that is introduced by the broad energy mesh and the Wigner-Seitz assumption.

The influence of assuming isotropic scattering sources in ROLAIDS-CPM can be studied by varying the Legendre order of scattering in the XSDRN calculations. Although the calculations have been done with 107 energy groups, figure 5.5 gives the difference between the P_0 approximation and the P_3 approximation in the 43-group (MCNP) energy mesh to enable a direct comparison with figure 5.2.
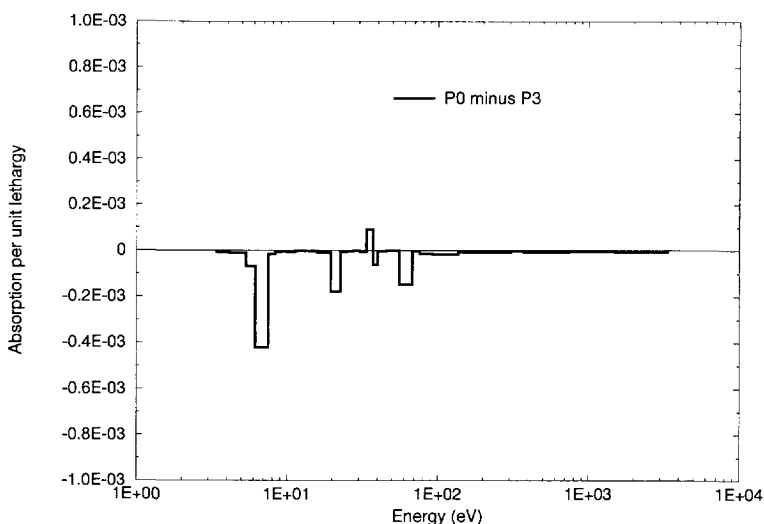
Figure 5.5: *Absorption in the fuel; difference between the P_0 approximation and the P_3 approximation (calculated with 107 groups, given in 43 groups).*

Apparently, the difference mainly occurs in the lower-energy range. However, because the angular dependence of the scattering density will strongly vary with energy around resonance energies, the difference between different orders of scattering should be calculated with a fine energy mesh. We only have such a fine energy mesh in the lower-energy range. From a comparison of figures 5.5 and 5.2 it is clear that the differences in the lower-energy range are of the same order of magnitude in the two figures. This is very important for the verification of ROLAIDS-CPM. The differences which occur can be ascribed to the assumption in the calculational model.

The results show that the anisotropy of the scattering sources is not important. So, ROLAIDS-CPM can very well be used for LWR lattice calculations. A more detailed comparison can be found in reference 60.

5.5   Conclusions

Very accurate Monte Carlo calculations are extremely important for a detailed comparison between different codes. The statistical uncertainty in our Monte Carlo calculation with MCNP is so small that differences with other codes do not get lost in statistics.

ROLAIDS-CPM is a suitable deterministic code for accurate calculations of the resonance absorption in a fuel pin. Not only the total absorption, but also the distribution of the absorption over the fuel pin is calculated accurately. The remaining differences with the MCNP results for the cylindrical cell are very small.

The multigroup discrete ordinates calculations with XSDRN appear to be very dependent on the energy mesh that is used. The XMAS 172-group energy mesh, of which 45 groups cover the energy range for our resonance absorption calculations, does not lead to accurate results. With a new 107-group energy mesh (instead of 45) very accurate ROLAIDS-CPM/XSDRN results have been obtained.

However, both ROLAIDS-CPM and XSDRN use the Wigner-Seitz assumption. A comparison between Monte Carlo calculations in a square pin cell and a cylindrical pin cell with the Wigner-Seitz approximation shows that the resulting error cannot be neglected in general. Especially in lattices in which the Dancoff effect has a large impact on the angular distribution of the neutron flux the Wigner-Seitz assumption influences the results.

A more general conclusion of these benchmark calculations is that validation should not only be aimed at producing "correct" results but also at quantifying the aberration that is introduced by the calculational method and at determining the phenomena that influence this aberration. Seemingly accurate benchmark results may well be due to cancellation of errors.

Chapter 6

The effective fuel temperature in fresh UO$_2$ fuel

6.1 Introduction

The effective fuel temperature is an important parameter for the calculation of transients in a nuclear reactor. This effective fuel temperature is used to take account of the neutronic feedback. At the moment there is no consensus on how this feedback fuel temperature should be calculated for an arbitrary radial temperature profile in a fuel pin. More than 20 years ago some papers were published on the subject of a radial temperature profile in a fuel pin [12–17]. It should be noted that the main purpose of these papers was the determination of the effective fuel temperature for the stationary situation with a well established radial temperature profile in the fuel pin. Only for such a fixed temperature profile the feedback fuel temperature can be described in terms of a surface and a central fuel temperature. The limited applicability of such a description is not generally recognized; such expressions are sometimes used in transient calculations [61] in which the fuel temperature profile changes. What one actually needs in transient calculations is an expression for the effective fuel temperature $T_{F,eff}$ as a function of the fuel temperatures in the zones (T_i) such as equation 3.17.

Two starting-points can be found in literature. First, Dresner [16] arrived at the average fuel temperature as effective fuel temperature. Secondly, Rowlands [14] indicated a chord weighting method. These methods are treated in section 6.2. On the basis of a literature survey it is shown that both methods can be derived from the same basic principles, but with different assumptions for the absorption in the fuel pin. To determine the accuracy of these expressions, it is necessary to do calculations with different temperature profiles. Even though it will appear

59

that the theoretical expressions are not correct for arbitrary temperature profiles, the derivation in section 6.2 is useful because it shows the origin of feedback expressions which are in use nowadays.

In section 6.3 a literature survey of calculations and experiments on nonuniform fuel temperature distributions is given. Calculations on arbitrary nonuniform temperature profiles from which a set of weights for equation 3.17 can be deduced have not been found in literature. Therefore, these calculations had to be done with ROLAIDS-CPM.

First, in section 6.4 calculations for a series of temperature profiles in a $^{238}UO_2$ slab are presented which have been done to get more insight into the physics of the problem. The influence of a temperature profile appears to be quite complicated. So, it is necessary to use a brute-force approach to derive a set of weights for equation 3.17. In section 6.5 calculations on a $^{238}UO_2$ pin are described. These calculations result in a brute-force expression for the effective fuel temperature for this specific fuel pin. Then, the influence of different expressions for the effective fuel temperature on a reactivity initiated transient is presented in section 6.6. Some general conclusions are given at the end of this chapter in section 6.7.

6.2   Derivation of theoretical expressions

The problem of the influence of a temperature profile in a fuel lump was studied as early as in 1954 by Roe [62], who looked at the resonance absorption by a single purely absorbing Breit-Wigner resonance in a slab with a nonuniform temperature distribution. The neutron flux in the moderator is assumed to be isotropic and flat with respect to lethargy. Essential in the treatment of the problem is the neglect of neutron scattering. Roe studied the ψ-function for an arbitrary temperature profile. Using the notation of chapter 2, this is given by:

$$\overline{\psi} = \frac{1}{a} \int_0^a \psi(\zeta(z), x) dz, \tag{6.1}$$

where a is the width of the slab, and z is the spatial coordinate. Roe used the condition that:

$$\int_{-\infty}^{\infty} \psi^2(\zeta_{\text{eff}}, x) dx = \int_{-\infty}^{\infty} \overline{\psi}^2 dx, \tag{6.2}$$

where ζ_{eff} is the value of ζ for the effective fuel temperature. Under this condition he found that the effective fuel temperature is somewhat lower than the average fuel temperature. Approximately, it can be decuded from:

$$\theta_{\text{eff}} = \overline{\theta} - \frac{3}{2} \frac{(\overline{\theta^2} - \overline{\theta}^2)}{1 + 4\overline{\theta}}, \tag{6.3}$$

where $\theta = \dfrac{1}{\zeta^2} = \dfrac{4E_0 k_B}{\Gamma^2 A} T$.

Keane [63] studied the same problem by considering only neutrons impinging normally on the slab. The absorption probability P_A for a neutron in a purely absorbing slab can be written as:

$$P_A(x) = 1 - \exp\left[-N\sigma_0 \int_0^a dz\psi(\zeta(z), x)\right], \qquad (6.4)$$

where N is the nuclide density of the absorber in the slab. By assuming a parabolic temperature profile in the slab, Keane found an analytical function χ for the average ψ-function in the slab:

$$\frac{1}{a}\int_0^a dz\psi(\zeta(z), x) = \chi(\zeta_{max}, x, \tau), \qquad (6.5)$$

where ζ_{max} is the value of ζ for the maximum (central) slab temperature, and $\tau = \dfrac{T_s}{T_c - T_s}$, with T_s the surface temperature, and T_c the central temperature.

By studying the behaviour of the χ-function and comparing it with the behaviour of $\psi(\zeta, x)$, Keane found that for a resonance with large $N\sigma_0 a$ (high absorption) the effective temperature is approximately given by the volume averaged value of the parabolic temperature profile:

$$T_{F,eff} = T_s + \frac{2}{3}(T_c - T_s). \qquad (6.6)$$

For resonances with small $N\sigma_0 a$ Keane arrived at the same equation as Roe had studied. So, the effective fuel temperature in a purely absorbing slab can approximately be taken as the volume averaged fuel temperature.

Reichel and Keane [12] investigated the effect of a parabolic temperature profile in a cylinder. Figure 6.1 shows an arbitrary chord with length L and its projection Y on the diametral plane.

Now, let us consider the temperature profile along the chord. The temperature in the fuel pin is given by:

$$T(r) = T_s + (a^2 - r^2)\frac{T_c - T_s}{a^2}, \qquad (6.7)$$

where a is the radius of the cylinder, and r is the radial distance from the centre of the fuel pin.

With $r^2 = a^2 + y^2 - yY$, and $y = \frac{l}{L}Y$, where l is the distance along the chord L, and y is the corresponding distance along the projection Y, the temperature along the chord is given by:

$$T(l) = T_s + \frac{(T_c - T_s)Y^2}{a^2}\left(\frac{l}{L} - \frac{l^2}{L^2}\right). \qquad (6.8)$$

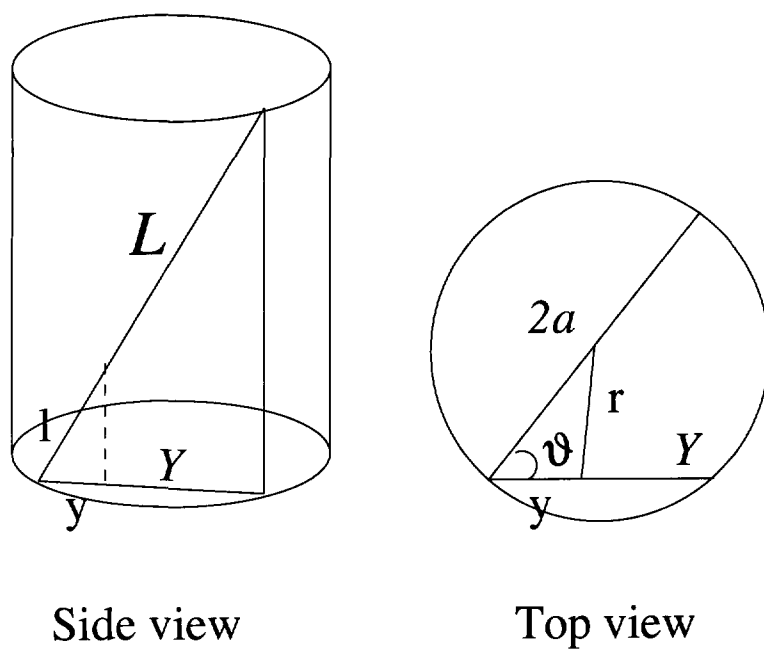Side view   Top view

Figure 6.1: *Projection (Y) of chord (L) on diametral plane.*

This is a parabolic temperature profile with maximum:

$$T_c'(Y) = T_s + \frac{(T_c - T_s)Y^2}{4a^2}. \tag{6.9}$$

A neutron which enters the cylinder along this chord can be considered as a neutron which enters normally on a slab with width L. In analogy with the situation for a slab the average value of ψ is given by:

$$\frac{1}{L} \int_0^L \psi(\zeta(l), x) dl = \chi(\zeta_{max}', x, \tau'), \tag{6.10}$$

where ζ_{max}' is the value of ζ for the maximum chord temperature (equation 6.9), and τ' is given by:

$$\tau' = \frac{4a^2\tau}{Y^2}. \tag{6.11}$$

The effective temperature for the chord L is just the average temperature of the chord L in analogy with the situation for the slab:

$$T_{F,\text{eff}}(Y) = T_s + \frac{2}{3}(T_c' - T_s) = T_s + \frac{Y^2}{6a^2}(T_c - T_s). \tag{6.12}$$

To arrive at an effective temperature for the whole cylinder, the resonance absorption has to be averaged over all neutron paths or chords through the cylinder. Again, neutron scattering in the fuel is neglected. Equations 6.9 up to 6.11 show that the average ψ-function along an arbitrary chord L does not depend on L itself but on Y. So, the averaging procedure can be done by considering the distribution of the projected chord lengths $p(Y)$.

By assuming isotropic incidence of the neutrons the chord length distribution is given by [12]:

$$p(Y)dY = \cos\vartheta d\vartheta, \tag{6.13}$$

where ϑ $(0 \leq \vartheta \leq \frac{\pi}{2})$ is the angle between the inner surface normal and the projection of the chord on the diametral plane (see figure 6.1).

Rowlands [14] made some interesting remarks on the work of Reichel and Keane. First, he stated that without scattering in the fuel it is not important in which way the different temperature zones in a slab are ordered. So, the result of Keane that the effective slab temperature is the average slab temperature is valid for a large class of temperature distributions. Then, Rowlands indicated a best averaging procedure for the effective temperature in a lump as:

$$T_{F,\text{eff}} = \int dL f(L) \frac{\int_0^L dl T(l)}{L}, \tag{6.14}$$

where $f(L)$ is the chord length distribution for the body, and where $T(l)$ is the temperature distribution along the chord L.

However, because in general the temperature distribution along a chord is not uniquely determined by the chord length, we feel that equation 6.14 should be extended. Instead of integrating over all possible chord lengths, one should integrate over all possible chords. Then, the equation reads:

$$T_{\text{F,eff}} = \int_S dS \int_{\vec{n} \bullet \vec{\Omega} > 0} d\Omega g(\vec{r}_s, \vec{\Omega}) \frac{\int_0^{L(\vec{r}_s, \vec{\Omega})} dl\, T(l)}{L(\vec{r}_s, \vec{\Omega})}, \qquad (6.15)$$

where S is the surface of the fuel lump, $\vec{n}$ the inner surface normal at S, $\vec{\Omega}$ a unit vector at the postion $\vec{r}_s$ on the surface and $g(\vec{r}_s, \vec{\Omega})$ is the probability distribution for the chords, and $L(\vec{r}_s, \vec{\Omega})$ is the length of the chord. For isotropic incidence of the neutrons and with $\phi(u) = 1$ outside the fuel lump, $g(\vec{r}_s, \vec{\Omega})$ is given by:

$$g(\vec{r}_s, \vec{\Omega}) = \frac{\vec{n} \bullet \vec{\Omega}}{\pi S}. \qquad (6.16)$$

Now, with the help of the above described theory, we look at the problem from a very basic point of view. This is done to arrive at simple theoretical models, and to relate other results to these models. As above, scattering in the fuel is neglected, which means that we can study the problem by considering the probability distribution for the chords $g(\vec{r}_s, \vec{\Omega})$, which is assumed to be energy-independent. We equate the absorption in the lump with a given temperature profile with the absorption in the lump with the homogeneous effective fuel temperature:

$$\int_S dS \int_{\vec{n} \bullet \vec{\Omega} > 0} d\Omega g(\vec{r}_s, \vec{\Omega}) \int_0^{L(\vec{r}_s, \vec{\Omega})} dl\, A(l, T_{\text{F,eff}}) = \qquad (6.17)$$

$$\int_S dS \int_{\vec{n} \bullet \vec{\Omega} > 0} d\Omega g(\vec{r}_s, \vec{\Omega}) \int_0^{L(\vec{r}_s, \vec{\Omega})} dl\, A(l, T(l)),$$

where $A(l, T)$ is the absorption rate density at postion l with temperature T.

It is assumed in our analysis that the effective fuel temperature along a chord equals the average fuel temperature along this chord. This assumption is an extension of Rowlands' statement that this is true for all those temperature distributions which can be rearranged to form a parabolic temperature profile. It is felt that this extension does not have a very firm base, but in view of the simplicity of our models it is certainly justifiable.

First, the situation for a slab is considered. The absorption $\int_0^L dl\, A(l, T(l))$ for any chord in a slab is assumed to be equal to $\int_0^L dl\, A(l, \overline{T(L)})$, where the average fuel temperature along a chord $\overline{T(L)}$ equals the volume averaged fuel temperature

$\overline{T_F}$. So, the effective fuel temperature for a slab is just the volume averaged fuel temperature: $T_{F,eff} = \overline{T(L)} = \overline{T_F}$. The weights for equation 3.17 are simply given by the relative widths of the different zones in a slab. This result is completely independent of the chord length distribution through the slab.

The situation is more complicated for a cylinder. Again, it is assumed that the absorption for a chord with a specific temperature profile is the same as for this chord with the average temperature. So, we can simplify equation 6.17 by recalling that in the case of a radial temperature profile the average temperature along a chord is a function of the projected chord length Y. So:

$$\int_0^{2a} dY p(Y) \int_0^Y dy A(y, T_{F,eff}) = \int_0^{2a} dY p(Y) \int_0^Y dy A(y, \overline{T(Y)}). \quad (6.18)$$

However, the average temperature of a chord depends on the value of Y (equation 6.12). The problem is how the different chords should be weighted. Two extreme situations are considered: very high absorption and very low absorption.

For high resonance cross sections the absorption mainly occurs near the surface of the fuel pin. The mean free path $(1/\Sigma_t)$ is very small. Thus, the absorption is relatively independent of the chord length. Then, all chords get equal weights, and with the assumption that the absorption is linear with the fuel temperature one arrives at:

$$T_{F,eff} = \int_0^{2a} dY p(Y) \overline{T(Y)}, \quad (6.19)$$

which is in fact the model of Rowlands. The effective fuel temperature which is calculated with this method is called the chord averaged fuel temperature.

Equation 6.19 has been evaluated numerically for isotropic incidence of the neutrons by applying a similar method as is used for the determination of the collision probabilities for cylindrical geometry in ROLAIDS-CPM [34]. Because of symmetry the integration can be done by drawing parallel lines in the diametral plane, as is shown in figure 6.2.

The integration interval is split into intervals $r_j < r < r_{j+1}$. Within every interval the Gaussian quadrature method is used to calculate the fraction of the relevant area which is taken up by specific fuel zones. This fraction is weighted by the ratio $(r_{j+1} - r_j)/a$ to obtain the weights for equation 3.17.

Table 6.1 shows the values of the weights for equation 3.17 when a cylinder is divided into 10 zones with equal volumes. The calculation has been done with 1000 integration intervals and with 5 Gauss-points per interval.

Before proceeding to the case of low absorption, it is indicated here how this model of high absorption has actually been used in literature. Rowlands [14] used equation 6.14 to arrive at an expression for the effective fuel temperature in a fuel pin with a parabolic temperature profile:

$$T_{F,eff} = T_s + \frac{4}{9}(T_c - T_s). \quad (6.20)$$
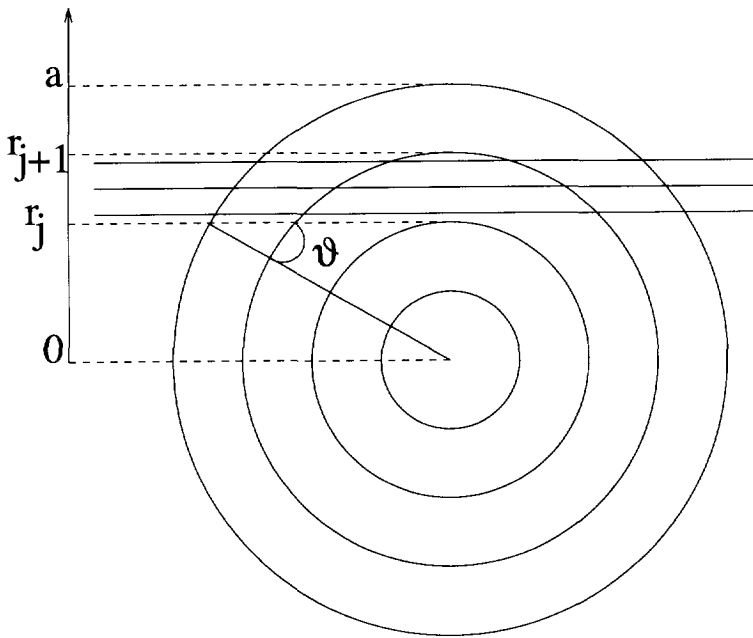
Figure 6.2: *Model to calculate the weights for different zones according to equation 6.19.*

Table 6.1: *Weights for equation 3.17 for 10 zones with equal volumes in a cylinder; numerically evaluated from equation 6.14 (chord averaged fuel temperature).*

Zone i (inner to outer)	Weight w_i
1	0.079560
2	0.081776
3	0.084304
4	0.087240
5	0.090726
6	0.094994
7	0.100461
8	0.107987
9	0.119917
10	0.153034

This is just about the value that is found in references 12 and 13, where equal weights for different chords were used.

Now, low absorption in the cylinder is considered. For low resonance cross sections the absorption along a chord is proportional to the chord length ($1 - \exp(-\Sigma_t L) \approx \Sigma_t L$). When the absorption is linear with the fuel temperature, this results in:

$$T_{\text{F,eff}} = \frac{\int_0^{2a} dY\, p(Y)\, Y\, \overline{T(Y)}}{\int_0^{2a} dY\, p(Y)\, Y}. \tag{6.21}$$

For isotropic incidence of the neutrons this is just the volume averaged fuel temperature $\overline{T_F}$. So, the weights for equation 3.17 are given by the relative volumes of the different zones in a cylinder.

This was also found by Dresner [16] who considered the problem of an arbitrary temperature profile in an isolated purely absorbing lump. Here, it is indicated how Dresner arrived at the same result as we get when we assume low absorption in the fuel lump. It will be shown that Dresner's treatment is not correct for high absorption.

By assuming a uniform and isotropic neutron flux outside the fuel lump ($\phi(u, \vec{\Omega}) = 1/(4\pi)$) the effective resonance integral I is given by:

$$NIV = \tag{6.22}$$

$$\int_{res} du \int_s dS \int_{\vec{n}\bullet\vec{\Omega}>0} d\Omega \frac{\vec{n}\bullet\vec{\Omega}}{4\pi} \left(1 - \exp\left(-N\sigma_0 \int_0^{L(\vec{r}_s,\vec{\Omega})} \psi(\theta,x)dl\right)\right).$$

Then, Dresner used an inequality to arrive at:

$$I \leq \frac{S}{4NV} \int_{res} du \left(1 - \exp\left(-N\overline{L}\sigma_0\overline{\psi(\theta,x)}\right)\right). \tag{6.23}$$

Because the difference between the right-hand sides of equations 6.22 and 6.23 is very small, Dresner drops the smaller than sign. Then, by considering the specific case of a cylinder with a parabolic temperature profile, he found that the average value of ψ can be approximated by the value of ψ at the volume averaged fuel temperature.

However, it can be seen that this procedure is not correct when the absorption is high, because then the exponential terms hardly affect the effective resonance integral, and the right-hand sides of equations 6.22 and 6.23 are almost the same for all temperatures. The temperature effect on the contrary is determined by the variation of the exponential terms in these equations. So, actually Dresner assumed low absorption.

Although two theoretical expressions are available to calculate the effective fuel temperature, these expressions can be derived from the same basic principles

with different assumptions for the amount of absorption. Both the volume averaged fuel temperature and the chord averaged fuel temperature seem to be useful.

It is obvious that many assumptions were made in the derivation of the two expressions. So, it is interesting to check the validity of these expressions against detailed calculational results or measurements presented in literature. The theory described above helps to understand and to analyse these results.

6.3 Literature survey of calculations/experiments

A Monte Carlo study of the effective fuel temperature by Olhoeft [17], in which 10 radial zones were used to represent an almost parabolic temperature distribution, showed that the effective fuel temperature in UO_2 is below the average fuel temperature $(\overline{T} = T_s + 0.5(T_c - T_s))$. The effective fuel temperature is given by:

$$T_{F,eff} \approx T_s + 0.4(T_c - T_s). \tag{6.24}$$

The comparison is complicated due to the fact that the exact temperature distribution is not given, but these results seem to indicate that the chord averaged fuel temperature is better than the volume averaged fuel temperature.

Arnold and Dannels [64] did Monte Carlo calculations on the resonance absorption in $^{238}UO_2$ pins for different homogeneous fuel temperatures to deduce Doppler coefficients for each radial region. By using a folding process they found for the effective fuel temperature in a fuel pin with a parabolic temperature profile:

$$T_{F,eff} = T_s + 0.35(T_c - T_s). \tag{6.25}$$

However, the folding process has no theoretical background at all. So, the above result is very suspicious.

Van Binnebeek [15] did calculations on the influence of a parabolic temperature profile in a fuel pin with two methods. In the first method, he divided a cylinder in two different zones to represent different parabolic temperature profiles. In fact, in this way the weights for these zones are calculated. Unfortunately, he presented the effective temperature in terms of T_s and T_c for specific resonances without exactly reporting the dimensions of the different zones. In his second method he used the exact parabolic profile. This method led to expressions for the effective fuel temperature which are always close to the volume averaged temperature or to the chord averaged temperature. Unfortunately, he only gave this last conclusion without reporting results for specific resonances or energy ranges. However, his conclusions confirm that both theoretical expressions are useful.

Authors [65,66] who investigated the effect of a radial temperature distribution in fast reactors found that the effective fuel temperature can be taken as the average fuel temperature. This is in agreement with our theoretical model because of the

low resonance cross sections in the high-energy range, which is the important energy range in fast reactors.

The only measurements on the effect of a nonuniform temperature distribution known to us are the measurements of Pettus and Baldwin on thorium-metal and thorium-dioxide rods [67]. Pettus and Baldwin concluded that the effective fuel temperature can be taken as the average fuel temperature. However, their mea- surements are not accurate enough to reject the chord averaged fuel temperature as effective fuel temperature.

It is very difficult, if not impossible, to measure the effect of a nonuniform temperature distribution accurately. It is much more simple to perform resonance absorption calculations in which it is possible to look closely at specific resonances or energy ranges. Unfortunately, in the past these calculations were done to express the effective fuel temperature in terms of a central and surface fuel temperature. This is useless in transient calculations.

So, to establish the accuracy of the expressions from section 6.2, it is necessary to do accurate calculations on different temperature distributions. This is done with artificial temperature profiles to facilitate the physical explanations of the results. First, we consider the situation for a slab where both theoretical expressions predict that the effective fuel temperature is equal to the volume averaged fuel temperature.

6.4 Effective fuel temperature in a UO$_2$ slab.

We have done slowing-down calculations with ROLAIDS-CPM (version 93.15) for a ^{238}UO$_2$ slab with a temperature distribution which is described by a step profile.

As can be seen in figure 6.3, the slab consists of 2 different temperature regions which have the same volumes. The volume averaged fuel temperature is always equal to 900 K. This means that one single temperature (for example in the outer region) defines the temperature profile. Deviations of the effective fuel temperature from the volume averaged fuel temperature can directly be related to this temperature. Although the step profile is unrealistic, this model is very useful because of its simplicity.

We have used the JEF2 nuclear data files, which we have processed with NJOY (version 91.88).

Because the resonance parameters can differ a lot, the capture of neutrons has been studied in 4 specific resonances for which some important parameters are listed in table 6.2. This table also shows the energy ranges for which the capture rates have been calculated. Above each energy range the neutron flux is assumed to be $1/E$.

These resonances are characterized by either large (6.7 eV and 36.7 eV) or small σ_0 values (377 eV and 518 eV), and by either large (36.7 eV and 518 eV) or
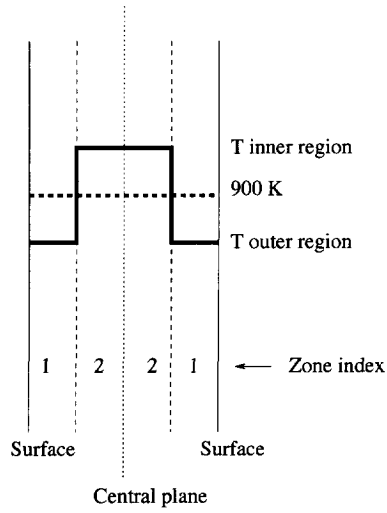
Figure 6.3: *Temperature regions in the slab.*

Table 6.2: *Properties of nuclear resonances of ^{238}U.*

Resonance energy (eV)	Γ_γ (eV)	$\frac{\Gamma_n}{\Gamma_\gamma}$	σ_0 (b)	Energy range (eV)
6.6740	$2.300 \cdot 10^{-2}$	0.065	24020	4 - 9
36.682	$2.289 \cdot 10^{-2}$	1.491	42915	32 - 42
376.9	$2.300 \cdot 10^{-2}$	0.049	326	370 - 380
518.4	$2.312 \cdot 10^{-2}$	2.183	3481	505 -525

Table 6.3: *Nuclide densities.*

Isotope	Region	Density (10^{24} atom/cm^3)
^{238}U	Fuel	0.022448
^{16}O	Fuel	0.045870
^{16}O	Moderator	0.023398
^{1}H	Moderator	0.046796

small neutron widths (6.7 eV and 377 eV).

The widths of the ^{238}UO$_2$ slabs are 1 cm, and they are separated by 5 cm water to isolate these slabs. The densities of the nuclides are given in table 6.3.

Figures 6.4 up to 6.7 show the effective capture resonance integral as a function of the temperature in the outer region of the slab T_{outer}. The effective capture resonance integrals for uniform temperatures $T_{uniform}$ are also given in these figures to enable a graphical determination of effective fuel temperatures. This effective fuel temperature is defined as the uniform temperature for which the neutron capture is equal to the neutron capture for a specific temperature profile. So, graphically the effective fuel temperature is determined by taking the point of interest on the solid line, drawing a horizontal line towards the dotted line, and, finally, drawing a vertical line towards the x-axis, where the effective fuel temperature can be read. The theoretical expressions predict a horizontal line in these figures.

When the dotted line is sharply rising in these figures, the variation in effective fuel temperature is small. When the figure is symmetric around $T_{outer} = 900$ K, the position of the temperature zones in the slab is not important. This is expected when scattering in the fuel is not important (377 eV resonance). When the effective resonance integral is larger when the highest temperature of the two is in the outer zone of the slab, the outer zone of the slab is more important. This causes the asymmetry in the figures, and shows that scattering is important for these resonances. It leads to a higher weight for this zone when the effective fuel temperature is given in the form of equation 3.17. The results clearly show that this form is not generally valid. Otherwise, the effective resonance integral would be linearly dependent on T_{outer} when the effective resonance integral is linearly dependent on the effective fuel temperature (figures 6.4 and 6.5).

Figures 6.4 up to 6.7 show complicated dependences of the effective resonance integral on the outer fuel temperature, although simple step profiles have been used. The purpose of this section is to determine the background of these complicated dependences in order to get more insight into the physics of the problem.

The theoretical considerations in the previous sections have generally been based on the assumption that the neutrons come from the moderator. So, it is

Figure 6.4: *Effective capture resonance integral for the 6.7 eV resonance (step profile ($\overline{T} = 900K$) or uniform temperature).*

Figure 6.5: *Effective capture resonance integral for the 36.7 eV resonance (step profile ($\overline{T} = 900K$) or uniform temperature).*

Figure 6.6: *Effective capture resonance integral for the 377 eV resonance (step profile ($\overline{T} = 900K$) or uniform temperature).*
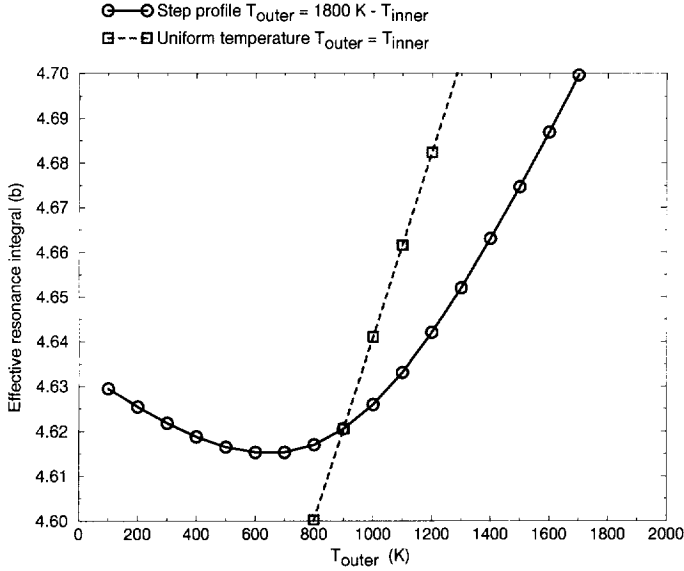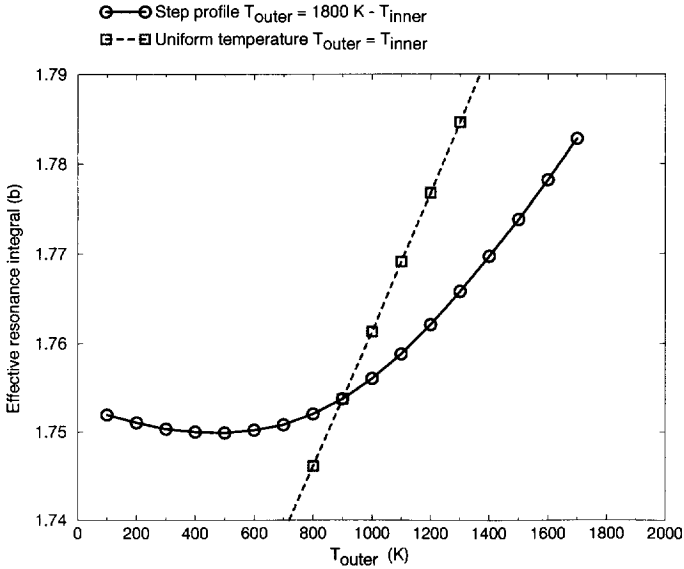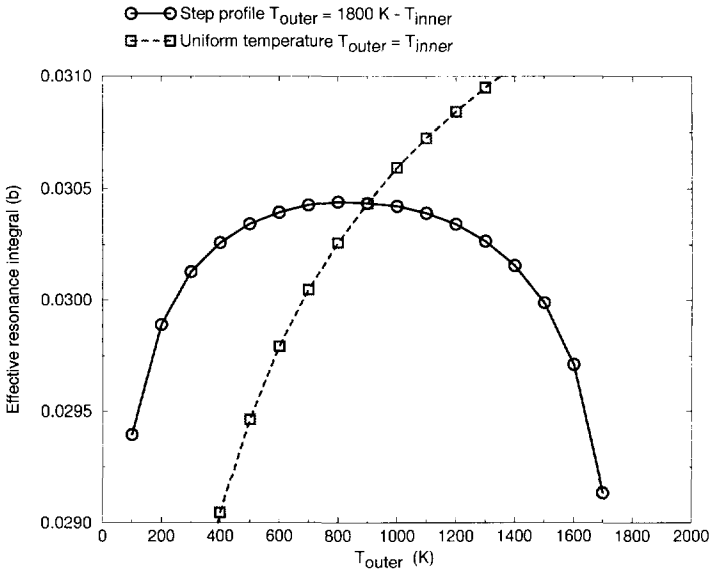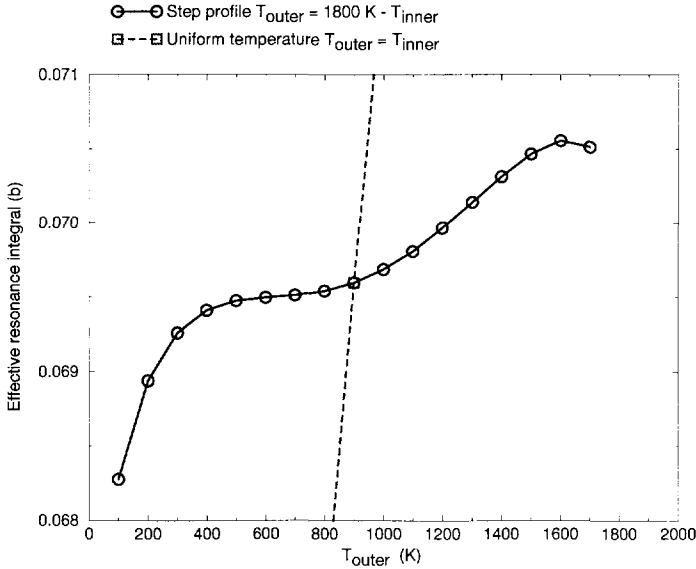

Figure 6.7: *Effective capture resonance integral for the 518 eV resonance (step profile ($\overline{T} = 900K$) or uniform temperature).*

Figure 6.8: *Effective capture resonance integral for the 6.7 eV resonance for neutrons which had their last scattering collision in the moderator (step profile or mixture of two temperatures)* ($\overline{T} = 900K$).

worthwhile to study the effective resonance integrals for neutrons which had their last scattering collision in the moderator. These effective resonance integrals are shown as solid lines in figures 6.8 up to 6.11 (ROLAIDS-CPM version 93.17).

Figures 6.8 up to 6.11 also show complicated dependences which for the resonances with large neutron widths are even largely different from the dependences in figures 6.4 up to 6.7. For these resonances with large neutron widths it is very important to take scattering sources in the fuel into account. As an example the 36.7 eV resonance is studied in more detail. Figure 6.12 shows the absorption of neutrons which had their last scattering collision in the outer zone of the fuel slab.

The effective resonance integral in figure 6.12 increases with T_{outer} because the scattering source increases. This causes the asymmetry in figure 6.5. The results for the other resonances can be analysed along the same line. The ultimate effect of the increase of the scattering source in the outermost zone does not only depend on the ratio Γ_n / Γ_γ, but for example also on the width of the slab, on the ratio V_M / V_F, on the moderator density, on the admixed nuclides in the fuel (oxygen in our case), and on the width of the resonance in comparison with the lethargy gain in a collision with ^{238}U.

Now, we turn our attention to the figures 6.8 up to 6.11. We consider only those neutrons which had their last scattering collision in the moderator. An important result is that the curves are not symmetric. They would be if scattering in the fuel
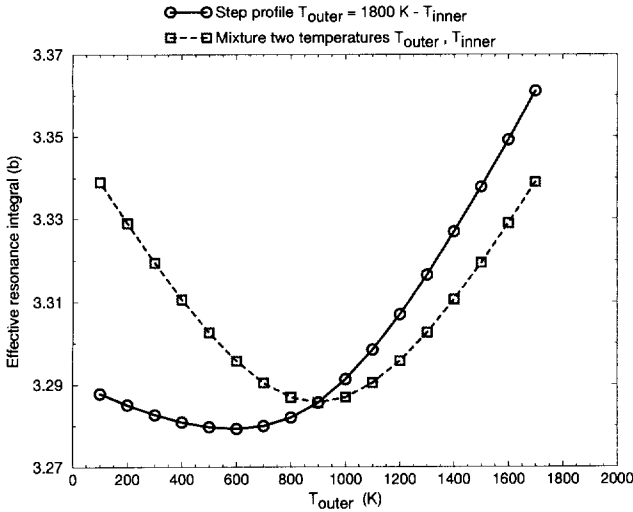
Figure 6.9: *Effective capture resonance integral for the 36.7 eV resonance for neutrons which had their last scattering collision in the moderator (step profile or mixture of two temperatures)* $(\overline{T} = 900K)$.

Figure 6.10: *Effective capture resonance integral for the 377 eV resonance for neutrons which had their last scattering collision in the moderator (step profile or mixture of two temperatures)* $(\overline{T} = 900K)$.

Figure 6.11: *Effective capture resonance integral for the 518 eV resonance for neutrons which had their last scattering collision in the moderator (step profile or mixture of two temperatures) ($\overline{T} = 900K$).*
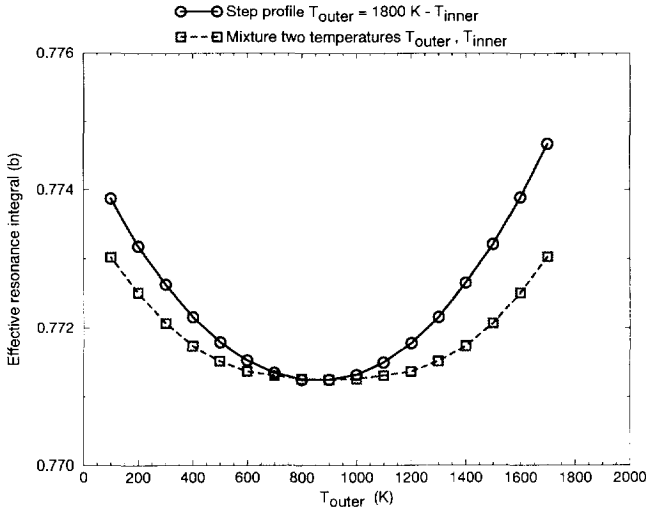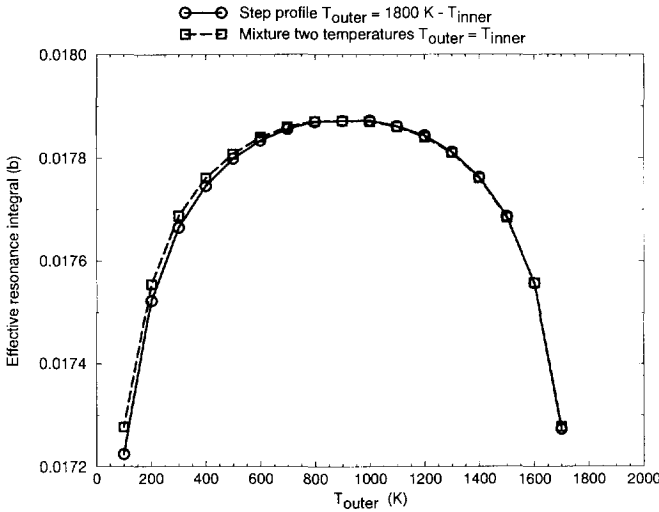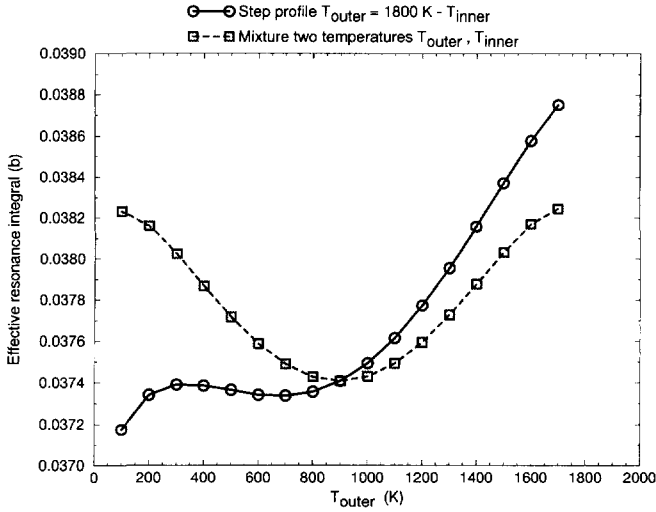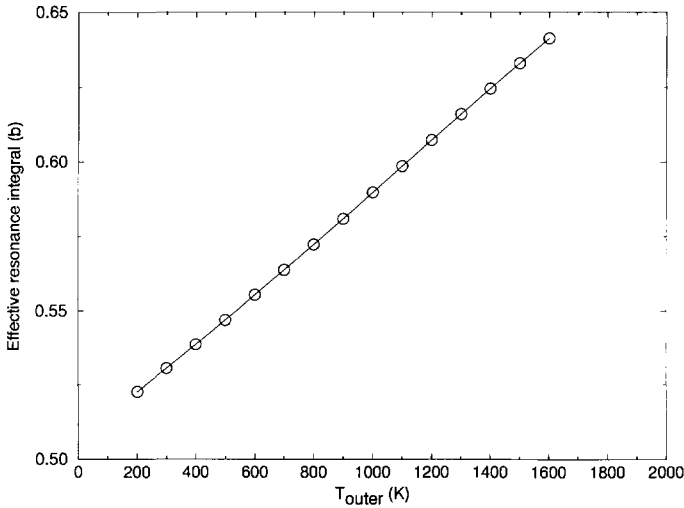

Figure 6.12: *Effective capture resonance integral for the 36.7 eV resonance for neutrons which had their last scattering collision in the outer zone of the fuel.*

can be neglected because then the order of the different temperature regions does not affect the total capture of neutrons in the slab. Indeed, figure 6.10 is almost symmetric because scattering in the fuel is not important for the 377 eV resonance.

The spatial effect of having two different temperature regions can be studied further by considering a mixture with nuclides at two different temperatures. In fact, the two temperature regions are homogeneously mixed. This is physically complete nonsense, but it helps to understand our results. The resonance integrals for these mixtures are also shown in figures 6.8 up to 6.11 as a function of one of the temperatures in the mixture (dotted curves). These curves are of course symmetric.

Now, let us first consider the curves for the mixture. The combination of temperatures itself gives rise to an increase in the absorption rate for three out of four resonances. However, for the low resonance with a small cross section and a small neutron width (377 eV) the absorption decreases.

This different behaviour has been investigated for the almost purely absorbing resonances at 6.7 eV and 377 eV by studying the mean free path ($= 1/\Sigma_t$) in the fuel. This has been done for the uniform temperature 900 K, and for a mixture of nuclides with temperatures 200 K and 1600 K. Figures 6.13 and 6.14 show the results.
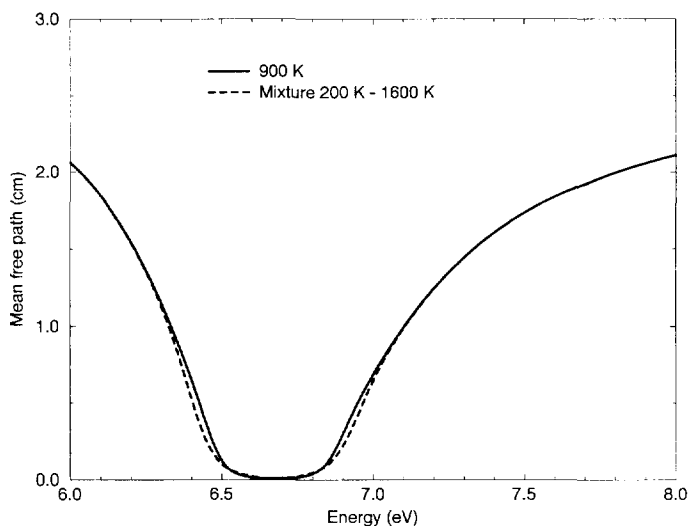
Figure 6.13: *Mean free path for the 6.7 eV resonance.*

Because the centre of the 6.7 eV resonance is black for the neutrons, the temperature does not influence absorption in the centre of this resonance. Only the wings of the resonance are important, and in these wings the mean free path is
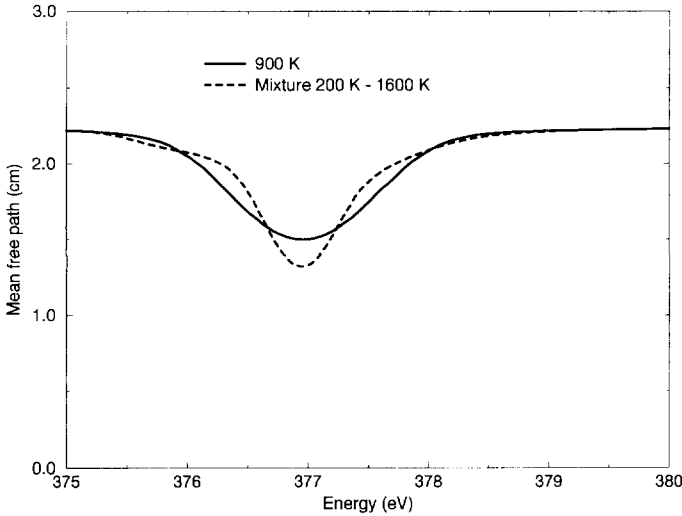
Figure 6.14: *Mean free path for the 377 eV resonance.*

smaller for the mixture of nuclides due to the high temperature of one component of the mixture. So, this explains why the absorption is higher for the mixture of nuclides for the 6.7 eV resonance.

The situation for the 377 eV resonance is completely different, because now the whole resonance energy range has to be considered. The absorption for the mixture of nuclides is higher in the centre of the resonance and in the outer wings of the resonance, but it is lower in between. In total, this leads to lower absorption for the mixture of nuclides.

In this way, the difference between the absorptions for mixtures of nuclides at different temperatures and at the same temperature can be studied. The results for a specific resonance will depend on the nuclide density and on the width of the slab, because they determine the "blackness" of the slab.

Now, we look at the effect of having two temperature zones instead of one zone with a mixture of the two temperatures. For this purpose we consider the 6.7 eV resonance and the 36.7 eV resonance, because for these resonances this effect is completely different (see figures 6.8 and 6.9). First, we consider the first collision absorption probability for a neutron which impinges normally on a slab with two temperature zones (figure 6.3):

$$P_A(x) = \frac{\Sigma_{a,1}}{\Sigma_{t,1}}(1 - \exp[-\mu_1]) + \frac{\Sigma_{a,2}}{\Sigma_{t,2}}(\exp[-\mu_1] - \exp[-(\mu_1 + 2\mu_2)])$$

$$+\frac{\Sigma_{a,1}}{\Sigma_{t,1}}(\exp[-(\mu_1 + 2\mu_2)] - \exp[-(2\mu_1 + 2\mu_2)]), \qquad (6.26)$$

where μ is the optical width ($= \Sigma_t d$) of a zone.

Without scattering in the slab the positions of the temperature zones in the slab do not influence the absorption probability for a neutron. The difference occurs because the ratio between the absorption cross section and the total cross section depends on the fuel temperature. When this ratio is larger, the fuel zone is more effective in absorbing the neutrons. When the most effective zone is on the outside of the slab, the absorption is higher. So, we have to study the energy-dependent ratio between the absorption cross section and the total cross section. These ratios are given in figures 6.15 and 6.16.
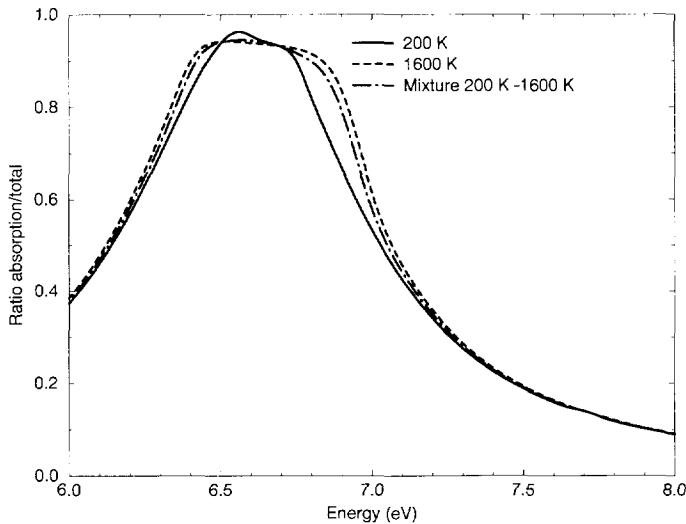
Figure 6.15: *Ratio between absorption cross section and total cross section for the 6.7 eV resonance.*

For the 6.7 eV resonance the zone at 1600 K is more effective in absorbing the neutrons than the zone at 200 K. So, the effective resonance integral in figure 6.8 is much higher when the highest temperature is at the outer boundary of the slab. The curve is asymmetrical.

For the 36.7 eV resonance the zone at 1600 K is more effective in absorbing neutrons with energies above the resonance energy, but it is less effective in
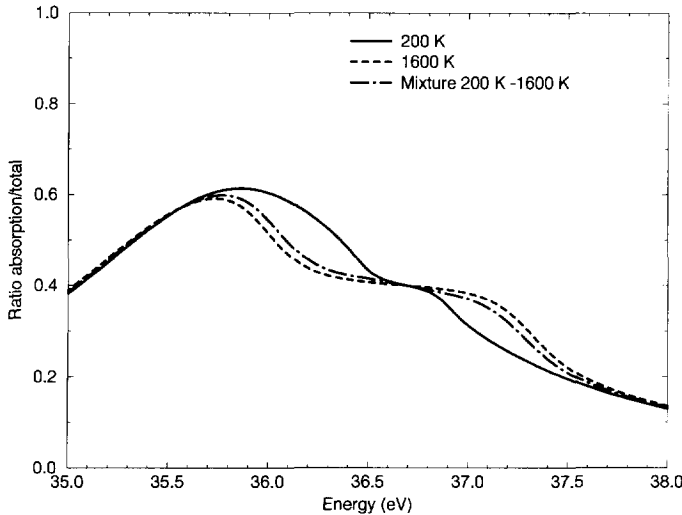
Figure 6.16: *Ratio between absorption cross section and total cross section for the 36.7 eV resonance.*

absorbing neutrons with energies below the resonance energy. This results in an almost symmetric dependence of the effective resonance integral on T_{outer}. The asymmetric behaviour shown in figure 6.16 is due to the phenomenon of scattering interference [26] which plays a prominent role for the strongly scattering resonance.

The considerations above show that it is very difficult to estimate the effect of a specific temperature profile on the resonance absorption without actually doing calculations. However, with our approach described above it is possible to give a qualitative explanation of the effect of a temperature profile.

Now, we turn our attention to the even more complicated problem of an arbitrary temperature profile in a fuel pin.

6.5   Effective fuel temperature in a UO$_2$ pin

6.5.1   Calculational Model

In this section a brute-force set of weights is determined for the 10 zones of the fuel pin defined in chapter 5 (table 5.1). The nuclide densities are given in table 6.4.

First, the cylinder has been divided in two temperature regions (step profile). Now, unlike in the previous section, the widths of these regions have also been

Table 6.4: *Nuclide densities.*

Isotope	Region	Density (10^{24} atom/cm^3)
^{238}U	Fuel	0.022448
^{16}O	Fuel	0.045870
^{27}Al	Cladding	0.055000
^{16}O	Moderator	0.023398
^{1}H	Moderator	0.046796

varied. The step profiles are characterized by the temperature in the outer zone(s) of the fuel T_{outer}, the difference ΔT between the temperature T_{inner} in the inner zone(s) and T_{outer}, and the number of zones with T_{outer} (1 up to 9). So, for every combination of T_{outer} and ΔT, given in table 6.5, 9 slowing-down calculations have been done. Also, resonance absorption rates in the fuel pin for homogeneous fuel temperatures have been calculated to enable the determination of effective fuel temperatures. This set of temperature profiles is rather arbitrary. In practice one would rather use the temperature profiles occurring during a transient. However, as in the previous section, the step profiles are very useful to analyse our results.

Table 6.5: *Combinations of outer fuel temperatures T_{outer} and temperature differences ΔT (indicated by 'x').*

ΔT	T_{outer}			
	600 K	900 K	1200 K	1500 K
100	x	x	x	x
200	x	x	x	x
300	x	x	x	x
600	x	x	x	x
900	x	x	x	x
-100		x	x	x
-200		x	x	x
-300		x	x	x
-600			x	x
-900				x

The spatial mesh in ROLAIDS-CPM is the same as for the standard calculation in section 5.3.

6.5.2   Results for the Whole Slowing-Down Energy Range

The neutron capture in the slowing-down energy range (2.7679 eV - 3.3546 keV) has been computed to enable the determination of an effective fuel temperature for every step profile.

By means of the least squares method a set of weights for the 10 different zones to calculate the effective fuel temperature according to equation 3.17 has been determined. The values for this brute-force set of weights are shown in table 6.6. In theory one would expect that the weights add up to 1, but because of the applied least squares method this is not necessary for our set of weights. Indeed, the calculated weights do not add up to 1 which means that an error is made when uniform temperatures are considered in the fuel pin. However, this error is very small since the sum of the weights is 1.0045.

Table 6.6: *Weights for equation 3.17 for the whole slowing-down energy range from the ROLAIDS-CPM calculations.*

Zone i	Weight w_i
1	0.0832
2	0.0853
3	0.0866
4	0.0891
5	0.0919
6	0.0958
7	0.1006
8	0.1074
9	0.1171
10	0.1475

In figure 6.17 a comparison is shown between the effective fuel temperature as it follows from the brute-force set of weights and the effective fuel temperature as it follows from a direct comparison of neutron capture rates. In fact, the accuracy of the least squares fit is displayed.

The weights in table 6.6 are very similar to the weights in table 6.1, although the difference between the weights for the inner zones and the weights for the outer zones is somewhat smaller. Figure 6.18 indeed shows that the chord averaged fuel temperature (table 6.1) agrees much better with the calculated effective fuel temperature than the volume averaged fuel temperature does.

In view of the results in the previous section it might be interesting to use not only the temperatures in the zones as parameters; figures 6.4 up to 6.7 clearly indicate that the effective fuel temperature cannot always be given in the form of
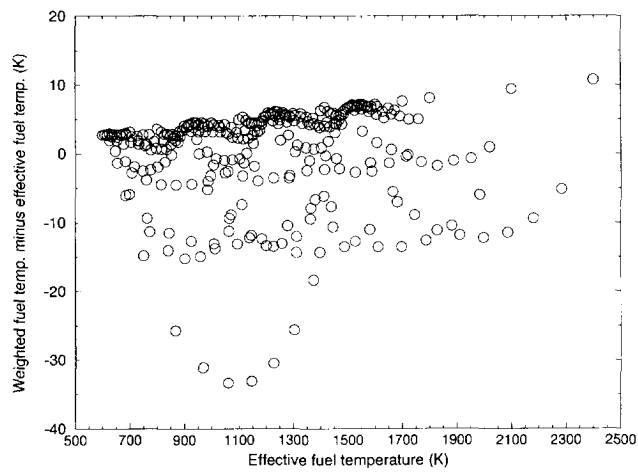
Figure 6.17: *Difference between weighted fuel temperature (table 6.6) and effective fuel temperature.*
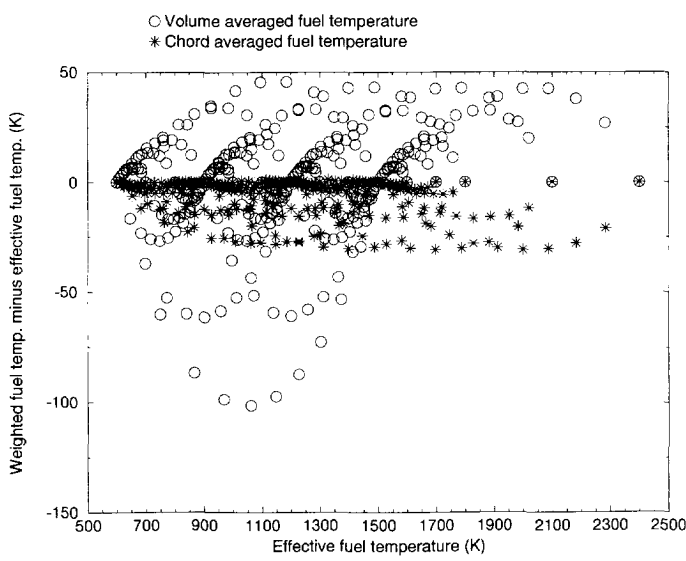
Figure 6.18: *Difference between the weighted fuel temperatures from the theoretical expressions and the effective fuel temperatures.*

equation 3.17. Therefore, other parameters have to be introduced which describe the temperature profile. In our case the temperature difference $|\Delta T|$ has been used as an extra parameter. So:

$$T_{\mathrm{F,eff}} = \sum_i w_i T_i + w_\Delta |\Delta T|. \qquad (6.27)$$

The new set of weights is given in table 6.7. The weights for the different zones are almost equal to the weights in table 6.6; they are only a little lower. The sum of the weights is 0.9978. Figure 6.19 shows that with the extra parameter $|\Delta T|$ the least squares fit improves with a factor 2 to 3. This indicates that when for realistic temperature profiles the effective fuel temperature cannot be calculated with sufficient accuracy using equation 3.17, other parameters can be introduced to improve the calculation of the effective fuel temperature.

Table 6.7: *Weights for equation 6.27 for the whole slowing-down energy range from the ROLAIDS-CPM calculations.*

Zone i	Weight w_i
1	0.0752
2	0.0853
3	0.0866
4	0.0891
5	0.0919
6	0.0958
7	0.1006
8	0.1074
9	0.1171
10	0.1488
$|\Delta T|$	0.0249

We have used a weighted fuel temperature which is a linear combination of the temperatures in the different zones. This is not strictly necessary. Other feedback formalisms might be more accurate. One might for example use a weighted fuel temperature which is a function of $\sqrt{T_i}$.

In practice, however, this procedure or the introduction of extra parameters are probably superfluous in view of other uncertainties in the calculation of the transient. It might only be interesting for very accurate reference results, but in this case extra slowing-down calculations during the transient calculation will probably be more effective to establish the effective fuel temperature.
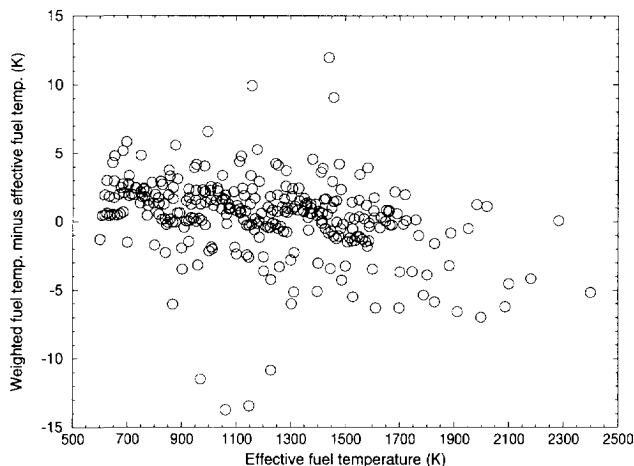
Figure 6.19: *Difference between weighted fuel temperature with extra parameter* $|\Delta T|$ *and effective fuel temperature.*

6.5.3   Results for Specific Energy Ranges or Resonances

The theoretical expressions predict two limiting situations for the effective fuel temperature. It is expected that the volume averaged effective fuel temperature is valid for the high-energy range, where the resonances are low, while the chord averaged effective fuel temperature is valid for the low-energy range, where the resonances are high.

To check this expectation, the neutron capture rates in small energy ranges instead of the neutron capture rates in the whole slowing-down energy range are considered. By comparing the normalized absorption rates (normalized to one neutron slowing down past the highest energy boundary), and by performing a least squares fit, the weights for the temperatures in the 10 different zones which yield the most accurate neutron capture rates for a particular energy range can be established. The weights are shown for several energy ranges in table 6.8. The three lowest energy ranges each encompass one single resonance.

These results are quite striking. The fact that the effective fuel temperatures for the whole slowing-down energy range agree well with the chord averaged fuel temperatures is coincidence, because the effective fuel temperatures for the low wide resonances do not show agreement with this chord averaged fuel temperature. Especially for the 36.7 eV resonance the weight for the outer zone is much larger. This can qualitatively be understood by looking at figure 6.5, since this figure

Table 6.8: *Weights for equation 3.17 for specific energy ranges from the ROLAIDS-CPM calculations.*

Energy range (eV)	Zone i	Weight w_i	Energy range (eV)	Zone i	Weight w_i
6.1601 - 7.5240	1	0.071	148.63 - 203.99	1	0.090
	2	0.075		2	0.090
	3	0.077		3	0.092
	4	0.080		4	0.094
	5	0.084		5	0.097
	6	0.090		6	0.099
	7	0.099		7	0.102
	8	0.111		8	0.106
	9	0.131		9	0.111
	10	0.193		10	0.118
19.455 - 22.603	1	0.073	748.52 - 914.24	1	0.098
	2	0.076		2	0.097
	3	0.077		3	0.098
	4	0.079		4	0.100
	5	0.083		5	0.101
	6	0.089		6	0.102
	7	0.097		7	0.103
	8	0.108		8	0.103
	9	0.128		9	0.103
	10	0.200		10	0.091
33.720 - 37.266	1	0.055	1234.1 - 1433.8	1	0.099
	2	0.059		2	0.098
	3	0.061		3	0.099
	4	0.065		4	0.100
	5	0.071		5	0.101
	6	0.079		6	0.102
	7	0.091		7	0.103
	8	0.108		8	0.103
	9	0.141		9	0.102
	10	0.277		10	0.089

shows a strong asymmetric dependence of the effective resonance integral on the fuel temperature in the outer zone.

The results for the higher-energy ranges show quite a good agreement with the volume averaged fuel temperature.

The values of the weights depend on the choice of our temperature profiles. Actually, one should use the temperature profiles which occur during a transient to find an accurate feedback expression for a specific lattice.

It must be concluded that a brute-force method is the only way to establish an expression for the effective fuel temperature for a specific pin cell in a thermal reactor. However, the question arises how the expressions for the effective fuel temperature influence the transient. In the next section an attempt is made to answer this question for two specific transients.

6.6   Fast reactivity initiated transients with different expressions for the effective fuel temperature

6.6.1   Introduction

Nowadays, different expressions for the effective fuel temperature such as a volume averaged fuel temperature, a combination of surface and central fuel temperature, or a weighted fuel temperature (equation 3.17) for which the unknown weights have to be specified by the user, are used in transient calculations. In this section three expressions for the effective fuel temperature have been used to study the influence on fast reactivity initiated transients. The first expression is defined by equation 3.17 with the brute-force weights given in table 6.6, the second by a volume averaged fuel temperature, and the third by the combination of surface and central fuel temperature given in reference 61:

$$T_{\mathrm{F,eff}} = T_s + 0.3(T_c - T_s). \tag{6.28}$$

6.6.2   Definition of Transients

The light water reactor lattice code LWRWIMS (version 3A, data library wen35) (section 3.7) is used to obtain two-group cross sections for different fuel temperatures, moderator temperatures, and boron concentrations. The model consists of an infinite lattice of pin-cells which have been defined in section 5.1 and for which effective fuel temperatures have been calculated in the previous section. Instead of aluminium, zirconium has been used as cladding material. A fuel enrichment of 2.1 wt % is assumed. The energy boundary between the two energy groups is at 4 eV. Because we focus on the effects of the effective fuel temperature in the epithermal energy range, the variation of the thermal group cross section with fuel

temperature is neglected (taken at 1000 K). Although we have only calculated the effective fuel temperature for capture by ^{238}U, this effective fuel temperature is used for all reaction rates in the non-thermal energy group. In principle, transient codes should have the possibility to input different effective fuel temperatures for different energy groups and maybe even reaction rates.

The transient calculations have been done with PANTHER (version 3.0) (section 3.8). Again, an infinite lattice of pin cells is used, but the pins have a finite axial length of 3.6 m. Axially, the pins are divided in 12 equidistant nodes, numbered from bottom to top. Radially, one fuel assembly (17 x 17 pins) is modelled as one node. A gap is modelled between the fuel pellet and the cladding. The outer radius of the gap is 0.4155 cm. The fuel is radially divided in 10 fuel zones with equal volumes. When the effective fuel temperature is given by equation 6.28, we use an extra very thin outer fuel zone to calculate the surface fuel temperature and an extra very thin inner fuel zone to calculate the central fuel temperature. The thermophysical properties of the fuel, gap, and cladding (zircaloy) are listed in reference 61.

An important aspect in the model is the radial distribution of the fission power in the fuel rod. The influence of this distribution will be considered in more detail in the next chapter. Here, a flat power distribution is assumed which is very reasonable for fresh fuel. The power distribution is in fact governed by the thermal flux distribution in the fresh fuel pin.

The transients start at hot zero power (HZP) or at hot full power (HFP) conditions. The nominal power of one fuel assembly is 17.7 MW. The HZP transients start at 10^{-6} times nominal power. The inlet moderator temperature is 565 K, the inlet flow is 82 kg/s per fuel assembly, and the pressure is 155 bar. This pressure is kept constant during the transients which implies that the density of the moderator is determined by the temperature.

The transients are initiated by the linear withdrawal of an absorber in 0.1 seconds. The reactivity inserted is 1303 pcm or 1.92 \$ ($\rho = 1$ \$ is equivalent with $\rho = \beta$) for the HZP transient ($\Sigma_{a,1} = 1 \cdot 10^{-3}$ cm^{-1}, $\Sigma_{a,2} = 1 \cdot 10^{-1}$ cm^{-1}), and about 943 pcm or 1.39 \$ for the HFP transient ($\Sigma_{a,1} = 7 \cdot 10^{-4}$ cm^{-1}, $\Sigma_{a,2} = 7 \cdot 10^{-2}$ cm^{-1}). The initial boron concentration, which is important because of the moderator temperature effect, is 661 ppm for the HZP transient and about 540 ppm for the HFP transient.

6.6.3 Transient Calculations

Two fuel temperatures are important during the transient: the average fuel temperature, and the effective fuel temperature. When the average fuel temperature is used as effective temperature, these temperatures are of course identical. Otherwise, these temperatures differ.

First, we consider the HZP transient. The behaviour of the volume averaged fuel temperature in the HZP transient is shown in figure 6.20, and the behaviour of the effective fuel temperature is shown in figure 6.21. Figure 6.22 shows the radial temperature profile in the fuel pins at a fixed axial position in the core at different times during the transient.

For comparable radial temperature profiles slowing-down calculations with ROLAIDS-CPM have been done to calculate the real effective fuel temperature. Table 6.9 gives these effective fuel temperatures as well as the temperatures calculated with the brute-force set of weights and the volume averaged fuel temperature. Besides, the effective fuel temperature has also been calculated with a renormalized set of brute-force weights, for which the total sum is 1. This ensures that uniform temperature profiles are calculated correctly. This table shows that the effective temperatures as they are calculated with the brute-force set of weights are quite accurate, even though these weights were calculated with a set of step profiles. The renormalized set of weights produces very accurate effective fuel temperatures for this transient. This is caused by the small temperature differences in the transient in comparison with the step profiles.

On the basis of figures 6.20 up to 6.22 the influence of different expressions for the effective fuel temperature on this specific HZP transient is explained hereafter.
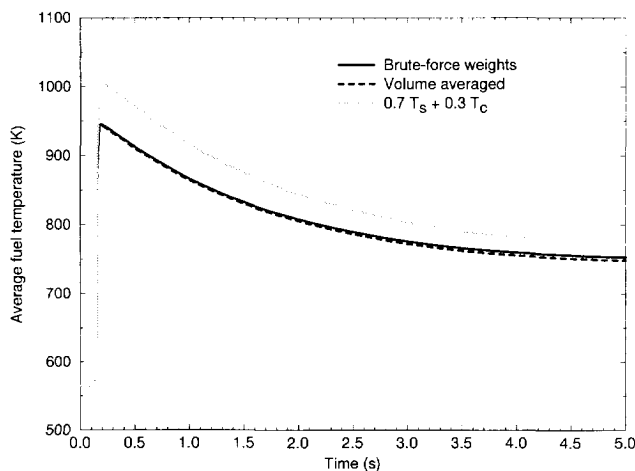
Figure 6.20: *Volume averaged fuel temperature in axial node 6 during the HZP transient.*

Because the transient starts at HZP the temperature profile is flat initially. Then, after about 0.15 seconds, the temperature increases fast. Even when the

Figure 6.21: *Effective fuel temperature in axial node 6 during the HZP transient.*

Figure 6.22: *Fuel temperature profiles in axial node 6 at different times during the HZP transient (effective fuel temperature = average fuel temperature).*

Table 6.9: *Effective fuel temperature at several times during the HZP transient as calculated directly with ROLAIDS-CPM, effective fuel temperature as calculated with the brute-force set of weights, the normalized brute-force set of weights, and the volume averaged fuel temperature.*

	Time				
	0.0 s	0.19 s	0.5 s	2.0 s	20 s
Temperature zone 1	565.0	965.0	995.0	965.0	885.0
Temperature zone 2	565.0	965.0	995.0	930.0	855.0
Temperature zone 3	565.0	965.0	990.0	890.0	830.0
Temperature zone 4	565.0	965.0	980.0	860.0	805.0
Temperature zone 5	565.0	965.0	960.0	825.0	760.0
Temperature zone 6	565.0	965.0	935.0	790.0	755.0
Temperature zone 7	565.0	965.0	900.0	760.0	730.0
Temperature zone 8	565.0	955.0	855.0	730.0	710.0
Temperature zone 9	565.0	930.0	810.0	700.0	685.0
Temperature zone 10	565.0	875.0	760.0	680.0	665.0
Direct ROLAIDS-CPM	565.0	946.7	903.4	798.3	758.6
Brute-force weights	567.6	950.9	907.8	801.9	762.2
Normalized brute-force weights	565.0	946.6	903.8	798.4	758.8
Volume weighted	565.0	951.5	918.0	813.0	770.0

average fuel temperature reaches its highest value ($t = 0.19$ s), the temperature profile is almost flat with a slightly lower temperature in the outer zones of the fuel. However, because of the steep temperature gradient near the fuel surface, the fuel surface temperature is much lower (figure 6.22). The feedback expression which uses the surface and central fuel temperature underestimates the fuel temperature effect. This implies that the power is overestimated which causes the high maximum volume averaged fuel temperature in figure 6.20. After the sharp increase in fuel temperature, the fuel temperature decreases, and the fuel temperature profile changes from a flat temperature profile to a parabolic temperature profile. At this moment differences show up between the transient with the effective fuel temperature from the brute-force set of weights and the transient with the volume averaged effective fuel temperature. For a given parabolic temperature profile the volume averaged effective fuel temperature would be about $\frac{1}{20}(T_c - T_s)$ larger than the brute-force effective fuel temperature. Otherwise, for a given effective fuel temperature the volume averaged fuel temperatures would differ by the same amount. The difference is not so high here, because the difference in fuel temperature leads to a difference in moderator temperature which influences the reactivity. Eventually, the introduced reactivity has to be balanced by the temperature effect (fuel and moderator). Without moderator temperature effect the effective fuel temperatures would be equal in the final stationary situation for different feedback expressions. Without fuel temperature effect the volume averaged fuel temperatures would be equal for different feedback expressions.

It is obvious that an expression for the effective fuel temperature which uses a combination of surface and central fuel temperature may lead to large errors. Although this expression is conservative in the analysed HZP transient, this is not a general feature. So, we strongly discourage the use of such expressions.

Now, we consider the HFP transient. The volume averaged fuel temperatures and effective fuel temperatures are shown in figures 6.23 and 6.24. Figure 6.25 shows the temperature distribution at different times during the transient.

Figure 6.25 shows that the temperature profile is parabolic initially. Then, it becomes somewhat more flat, and finally it is parabolic again. Absolutely however, the temperature increase is larger in the centre of the fuel pin even in the beginning of the transient. Thus, the effective fuel temperature with the brute-force set of weights results in a smaller fuel temperature effect than the volume averaged fuel temperature as effective fuel temperature.

So, by studying the temperature profiles which occur during a transient, the influence of expressions for the effective fuel temperature can be investigated.

Although the analysed transients are certainly not representative for all reactivity initiated transients, they illustrate the differences which may occur when different expressions for the effective fuel temperature are used. Further research should be done to quantify the errors involved with, for example, the volume averaged effective fuel temperature. We recommend to do more reference calculations
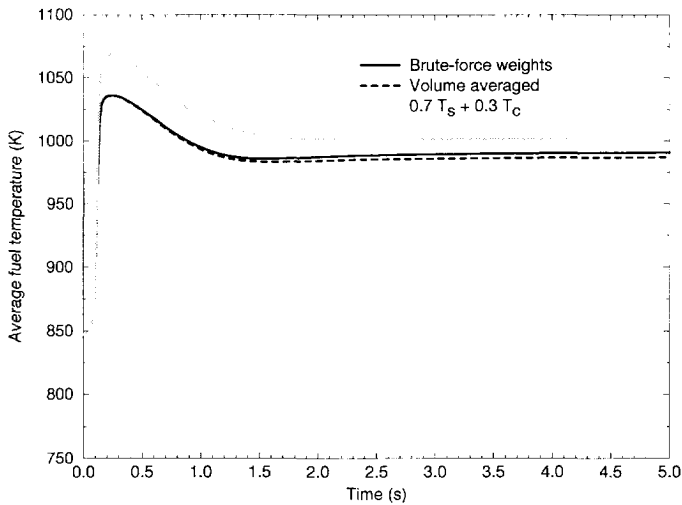
Figure 6.23: *Volume averaged fuel temperature in axial node 6 during the HFP transient.*
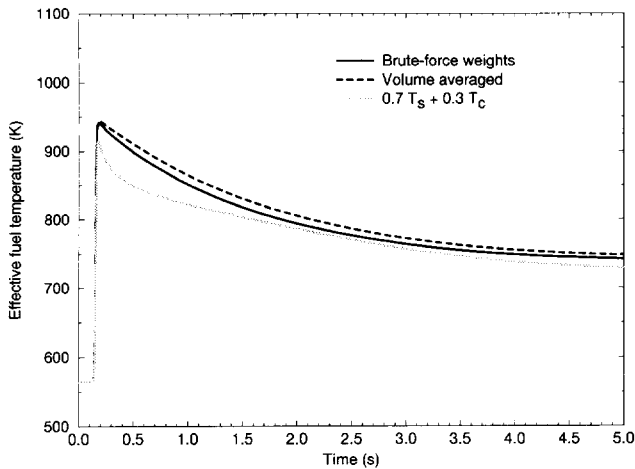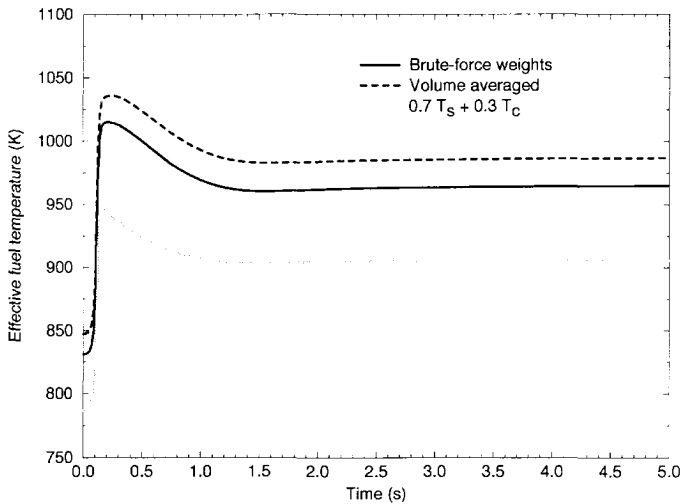

Figure 6.24: *Effective fuel temperature in axial node 6 during the HFP transient.*
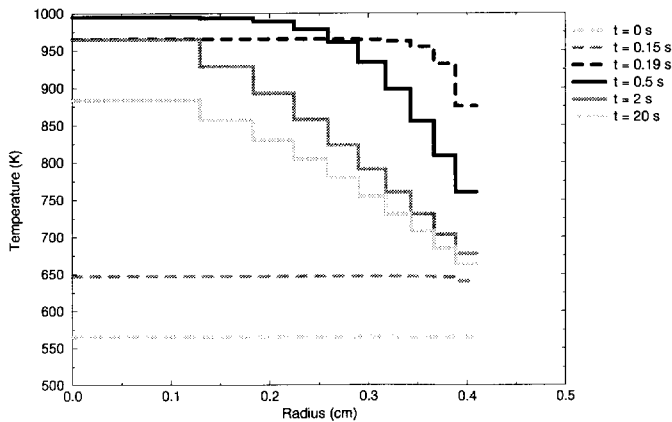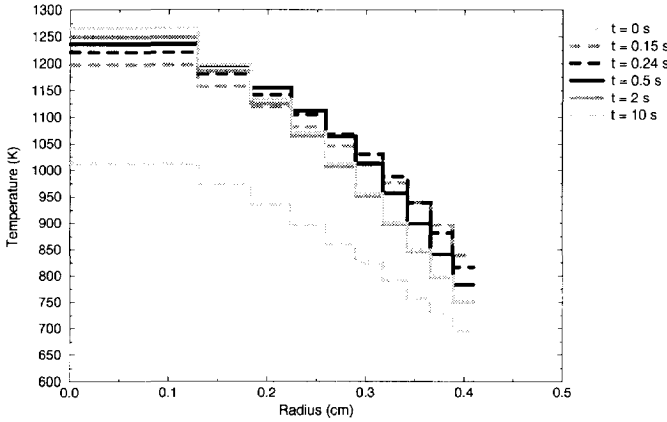
Figure 6.25: *Fuel temperature profiles in axial node 6 at different times during the HFP transient (effective fuel temperature = average fuel temperature).*

with the actual temperature profile and moderator density during the transient (see table 6.9).

6.7   Conclusions

Two theoretical expressions for the effective fuel temperature in a fuel pin with an arbitrary temperature distribution have been derived: the volume averaged effective fuel temperature, and the chord averaged effective fuel temperature. The derivation has been based on a literature survey. The following assumptions have been made in the derivation:

- neglect of scattering in the fuel

- the effective temperature for a chord through the cylinder is equal to the average temperature along this chord

- isotropic incidence of the neutrons on the fuel pin

The difference between the two expressions lies in the amount of assumed absorption. This determines how the different chords through the cylindrical fuel pin should be weighted. Low absorption leads to the volume averaged fuel temperature as effective fuel temperature. High absorption leads to the situation in which every chord gets the same weight; this effective fuel temperature is called the chord averaged fuel temperature.

Calculations on a $^{238}UO_2$ slab with a step temperature profile show that deviations from the theoretical expressions, which both predict the volume averaged fuel temperature as effective fuel temperature for a slab, depend on the specific resonance and are complicated. For an accurate calculation of effective fuel temperatures brute-force methods are necessary. The results can be analysed qualitatively by considering the origin of the neutrons which are absorbed; i.e., the zone in which they had their last scattering collision. For resonances which are almost purely absorbing the results can be analysed by considering only the neutrons which had their last scattering collision in the moderator. The influence of a combination of temperatures in the fuel can be investigated by studying the cross section or the mean free path of a homogeneous mixture of these temperatures. The influence of the spatial distribution of zones with different temperatures can be investigated by looking at the energy-dependent ratio of the absorption cross section and the total cross section. The larger this ratio, the more effective a fuel zone is in absorbing neutrons.

Calculations on a $^{238}UO_2$ pin show that the effective fuel temperature for the whole slowing-down energy range agrees well with the chord averaged effective fuel temperature. However, this is pure coincidence because for specific resonances the agreement is not good. The effective fuel temperatures in the high-energy range are about equal to the volume averaged fuel temperatures. The effective fuel temperatures in the low-energy range do not agree with any of the theoretical expressions. They depend strongly on the temperature in the outer zone of the fuel pin. The results for separate energy ranges imply that for transient calculations with many energy groups it is important to take the variation of the effective fuel temperature with the energy group into account.

Obviously, brute-force methods are necessary to calculate effective fuel temperatures. These methods can be applied in two different ways. First, by calculating effective fuel temperatures for a set of temperature profiles an expression for the effective fuel temperature can be found. This set of temperature profiles should be more extended and more realistic than our set of step profiles. Secondly, slowing-down calculations during the transient produce the most accurate results. In this way the exact temperature profiles are used in the slowing-down calculations. This method is especially useful for reference calculations. It can also be used to obtain conservative results by studying the effective fuel temperature for different radial temperature profiles which occur during the transient of interest.

Transient calculations show that a feedback expression based on a combination of surface and central fuel temperature gives deviating results. The brute-force expression and the volume averaged effective fuel temperature produce about similar results. Reference calculations with the actual temperature profile during the HZP transient show that the brute-force set of weights produces accurate effective fuel temperatures. We recommend to do these reference calculations for specific problems. The influence of the expressions for the effective fuel

temperature can also be analysed by studying the temperature profiles which occur during the transient.

Chapter 7

Influence of radial burnup on the Doppler effect

7.1 Introduction

An accurate calculation of the Doppler effect in transients is complicated when the burnup of fuel is taken into account. In fact, it is even complicated to calculate resonance absorption rates, because the resonance overlap of the different nuclides has to be taken into account. We do not consider this particular problem in this chapter, although ROLAIDS-CPM is very well suited to treat this matter. Here, we are primarily concerned about the influence of a different radial power profile due to the burnup.

The radial power profile in the fuel pin strongly depends on the distributions of the fissile nuclides in the fuel pin. Especially the distributions of the fissile plutonium isotopes are important, because these distributions sharply increase towards the surface of the fuel pellet [19,20]. The radial power profile influences the radial temperature profile and thereby the transient. So, accurate burnup calculations which take into account the radial effects are necessary. Fuel performance codes use experimental data to describe the dependences of plutonium densities on the radial position [68], but these densities can also be obtained from burnup calculations [69]. When no experimental data is available, one must rely on these calculations. Because the radial variations in the nuclide densities are mainly caused by the radial variations in resonance absorption rates, ROLAIDS-CPM is very suitable to do these calculations together with XSDRN and the burnup code ORIGEN. With the collision probability method in ROLAIDS-CPM this can be done more accurately than with the interface-currents method (see section 3.4), because the collision probability method enables us to use a very fine spatial

mesh. Section 7.2 presents the comparison of calculations with measurements of
the volume averaged nuclide concentrations and with measurements of the radial
distributions of some elements [20]. Then, in section 7.3 a representative peaked
power profile is used to study the influence of this peaked power profile on the
transients described in the previous chapter.

A further complication is the calculation of the effective fuel temperature for
given radial distributions of the nuclides. Slowing-down calculations which take
into account the radial distributions of the nuclides are necessary to calculate
effective fuel temperatures. This is briefly discussed in section 7.4. Some general
conclusions are given in section 7.5.

7.2   Radial distributions of the nuclide densities in the fuel

The calculational scheme for the burnup calculations has been given in section
3.6. The cell calculation uses 172-group AMPX-M libraries based on JEF2
data [70] and pointwise data from JEF2 (processed with NJOY 91.91) for the
ROLAIDS-CPM (version 93.15) calculation. ORIGEN (SCALE 4.1) uses the
updated ORIGEN-S working libraries [71]. The dimensions of the pin cell, the
initial nuclide densities, and the power history are specified in references 20 and
72. The list of nuclides which have been considered in the pin-cell calculation with
XSDRN is given in table 2 of [71]. For the resonance treatment with BONAMI
and ROLAIDS-CPM, only the initial fuel nuclides and the important plutonium
isotopes (^{238}Pu, ^{239}Pu, ^{240}Pu, ^{241}Pu, ^{242}Pu) are taken into account.

The isotopic composition of PWR fuel at a cumulative burnup of 44.34
MWd/kgU has been calculated. By the way, this is asked for phase Ib of the
burnup credit criticality benchmark [72]. The number of burnup steps is 70, and
the cross sections are updated 18 times. The power profile is updated after every
burnup step for the calculation of the radial distributions of the nuclide densities.

An important assumption is that the different isotopes do not migrate in the
fuel pin, which is very reasonable for the isotopes we are interested in. However,
migration of especially the fission products might influence the neutron spectrum
in the fuel pin and in this way the burnup of other nuclides. The importance of
this effect is not known and might be a subject in further research.

First, it is investigated how the total isotopic composition of the fuel is affected
when the radial distributions of the nuclide densities are taken into account. Table
7.1 shows the total nuclide densities for some important isotopes as they have
been measured [20] and calculated. For this purpose 10 concentric fuel zones with
equal volumes are used in the calculations. One calculation has been done without
taking into account the radial distributions of the nuclides and one calculation

Table 7.1: *Volume averaged nuclide densities in the PWR fuel pin sample with 44.34 MWd/kgU.*

Nuclide	Reference value $(\frac{mg}{g\ fuel})$	Calculated with radial distributions $(\frac{mg}{g\ fuel})$	Calculated without radial distributions $(\frac{mg}{g\ fuel})$
^{234}U	0.12	0.12	0.12
^{235}U	3.54	3.27	3.26
^{236}U	3.69	3.62	3.62
^{238}U	824.9	824.2	824.2
^{238}Pu	0.2688	0.2434	0.2428
^{239}Pu	4.357	4.303	4.319
^{240}Pu	2.543	2.534	2.550
^{241}Pu	1.020	0.981	0.984
^{242}Pu	0.8401	0.8209	0.8184

has been done with these radial distributions. For the calculation in which the radial distributions of the nuclides are taken into account 10 separate ORIGEN calculations have to be done; one for each zone.

The results hardly depend on whether the radial distributions of the nuclide densities are taken into account. So, for regular burnup calculations it seems justified to neglect these effects.

Because the radial variations of the nuclide densities mainly occur near the surface of the fuel pin, a different spatial mesh has been chosen to compare our results with measurements. This spatial mesh is given in table 7.2.

The calculated total nuclide densities are about the same as in table 7.1. The calculated radial distributions of the most important nuclides are given in table 7.3.

Some important aspects of these results are discussed here. First, the ^{235}U distribution is somewhat strange. The concentrations are a little bit higher in the outer thin rings of the fuel. This is a consequence of the constant power approximation during a burnup step, which underestimates the flux in the outer zones of the fuel pin.

Secondly, the buildup of plutonium in the outer zones of the fuel pin is quite large. This is caused by the strong spatial effect of the resonance self-shielding. In figure 7.1 the radial distribution of plutonium as it has been calculated is compared with the distribution as it has been measured with Electron Probe Micro Analysis (EPMA)[20].

The agreement is very good except for the outermost zones. However, it should be noted that in our calculations the dimensions of the pellet do not change. In reality, changes in the pellet structure occur which complicate the comparison.

Table 7.2: *Spatial mesh to study the radial distributions of the nuclide densities.*

Zone	Outer radius (mm)
1	2.5
2	3.5
3	4.0
4	4.3
5	4.5
6	4.6
7	4.68
8	4.74
9	4.77
10	4.7815

Table 7.3: *Radial distributions of important isotopes.*

Zone (inner to outer)	Density						
	^{235}U $(\frac{mg}{g\ fuel})$	^{238}U $(\frac{mg}{g\ fuel})$	^{238}Pu $(\frac{mg}{g\ fuel})$	^{239}Pu $(\frac{mg}{g\ fuel})$	^{240}Pu $(\frac{mg}{g\ fuel})$	^{241}Pu $(\frac{mg}{g\ fuel})$	^{242}Pu $(\frac{mg}{g\ fuel})$
1	3.448	828.8	0.223	3.665	2.398	0.772	0.623
2	3.297	827.7	0.232	3.773	2.361	0.829	0.686
3	3.175	826.2	0.242	3.953	2.349	0.903	0.763
4	3.095	824.2	0.251	4.218	2.393	0.991	0.850
5	3.043	821.2	0.262	4.663	2.534	1.121	0.970
6	3.017	816.5	0.275	5.362	2.810	1.311	1.140
7	3.013	809.6	0.293	6.423	3.258	1.594	1.388
8	3.025	797.0	0.324	8.317	4.072	2.103	1.834
9	3.050	779.1	0.369	10.969	5.209	2.833	2.480
10	3.072	761.8	0.413	13.449	6.277	3.537	3.111
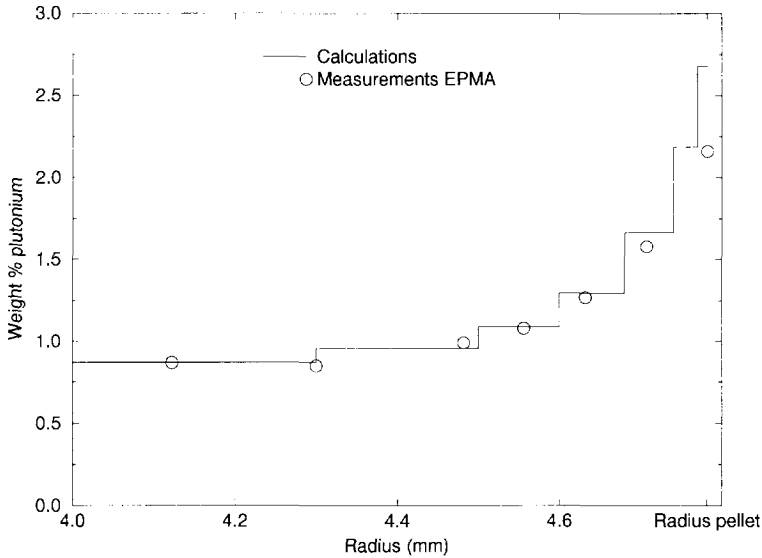
Figure 7.1: *Plutonium distribution in the outer region of the fuel pin.*

The distributions of [239]Pu and [241]Pu lead to a power profile which sharply increases towards the fuel pellet surface. Figure 7.2 shows the power density in the outer zones for fuel at different burnup stages.

The influence of the power profile on a transient will be treated in the next section. Here, some supplementary comments on fuel behaviour will be made.

The power profile is important for the radial temperature profile. This radial temperature profile does not only determine the neutronic feedback but it is also important for the mechanical and chemical phenomena in the fuel.

This is for example the case for the study of the release of fission products. This is often related to the average burnup of fuel in the pellet [20], but in fact the burnup near the surface of the pellet is important, because there the release of fission products occurs. To illustrate this effect of migration of fission products, figure 7.3 shows the distribution of xenon in the outer region of the fuel pin. Xenon migrates from the outer fuel region towards the gap.
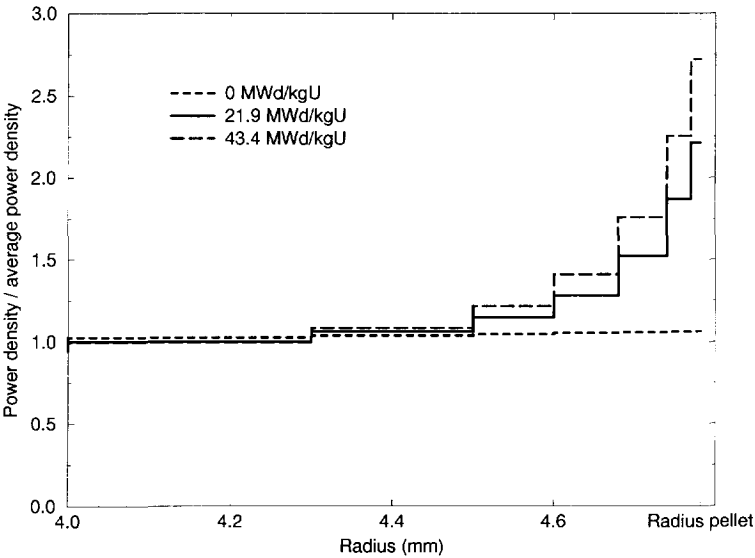
Figure 7.2: *Power density profile in the outer region of the fuel pin.*
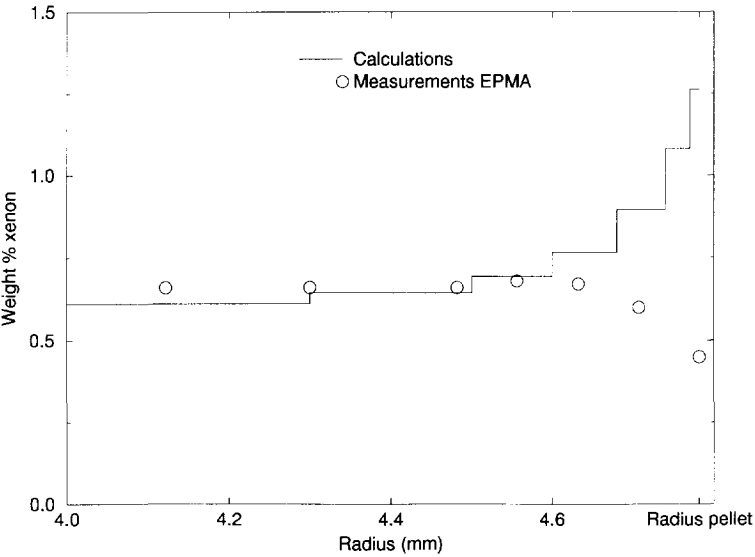
Figure 7.3: *Xenon distribution in the fuel pin.*

7.3   Fast reactivity initiated transients with a peaked power profile

In this section the fast reactivity initiated transients from section 6.6 are reconsidered, but now with a peaked power profile in the fuel pin. These transients were originally defined for fresh fuel, but because we want to study the direct influence of a power profile we use exactly the same cross section set as in the previous chapter. We have chosen for a peaked power profile which is comparable with the power profile for the fuel at 21.9 MWd/kgU (figure 7.2).

Because we want to have a strict separation of the influence of the expression for the effective fuel temperature and the influence of the power profile, we use the volume averaged fuel temperature as effective fuel temperature in this section. One may estimate the influence of different feedback expressions from the temperature profiles which occur during the transients.

For the same reason we have neglected the influence of the burnup on the thermal conductivity of the fuel. It is known that a high burnup leads to a decrease in thermal conductivity which may lead to a thermal barrier at the surface of the fuel pin [73].

Because of the peaked power profile a somewhat different radial mesh is used in the fuel pin. This spatial mesh and the power density in the different rings is given in table 7.4.

Figures 7.4 and 7.5 show the average fuel temperature for a flat power profile and for a peaked power profile in the HZP transient and in the HFP transient, respectively.

The peaked power profile leads to a lower average fuel temperature in the transient because the power is generated more near to the coolant (moderator). So, a flat power profile gives a conservative estimate of the fuel temperatures during the transient. However, not only the fuel temperature may be a limiting parameter, but also the cladding temperature may be the limiting criterion. This is especially the case for a HFP transient [5]. Figure 7.6 shows the difference between the cladding temperature and the coolant temperature for the HFP transient.

The peaked power profile leads to a higher peak cladding temperature. It is thus certainly not conservative with regard to this parameter to assume a flat power profile.

Figures 7.7 and 7.8 show the temperature profiles which occur during the transients with a peaked power profile.

Table 7.4: *Fine radial mesh with the ratio of the power density to the average power density for the peaked power profile.*

Outer radius (mm)	Power density/average power density
1.2950	0.94
1.8313	0.94
2.2429	0.94
2.5899	0.94
2.8956	0.94
3.1720	0.94
3.4261	0.94
3.6627	0.94
3.8135	1.01
3.9135	1.13
3.9935	1.27
4.0535	1.46
4.0835	1.79
4.0950	2.14

Figure 7.4: *Average fuel temperature in axial node 6 during the HZP transient with a flat power profile or a peaked power profile.*

Figure 7.5: *Average fuel temperature in axial node 6 during the HFP transient with a flat power profile or a peaked power profile.*

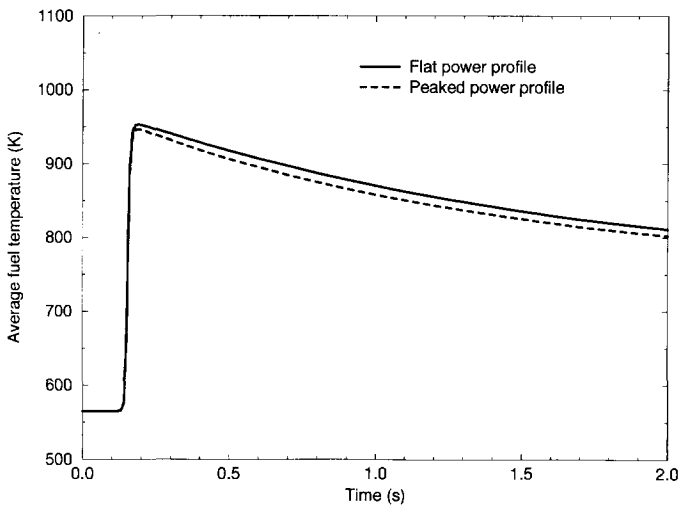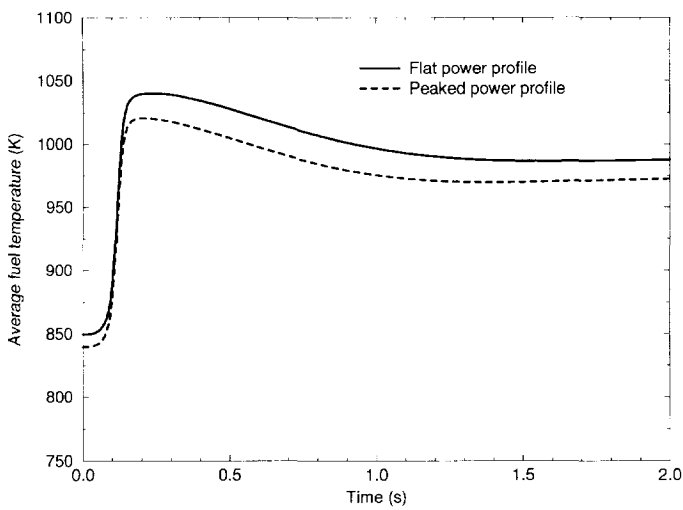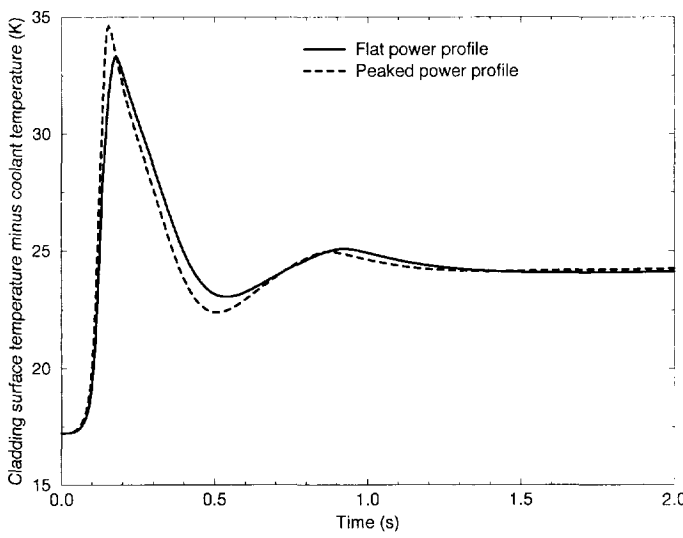Figure 7.6: *Difference between the cladding surface temperature and the coolant temperature in axial node 6 during the HFP transient with a flat power profile or a peaked power profile.*
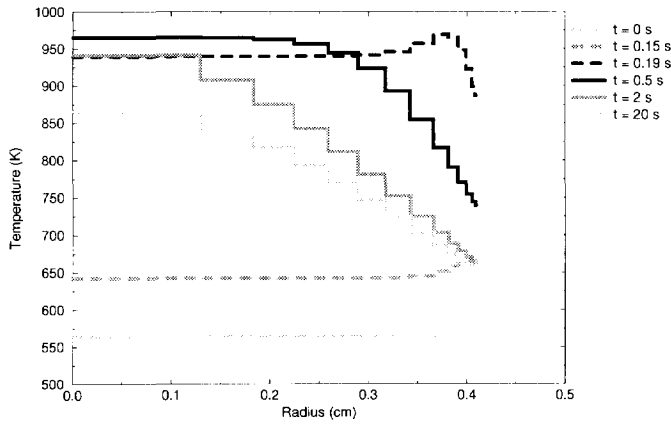
Figure 7.7: *Temperature profiles during the HZP transient with a peaked power profile.*
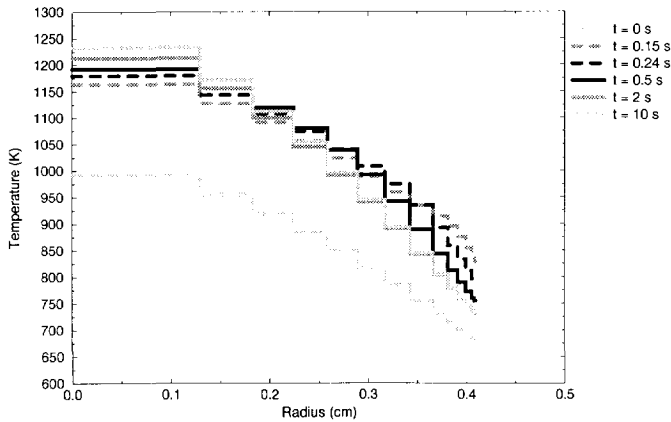
Figure 7.8: *Temperature profiles during the HFP transient with a peaked power profile.*

The differences between the temperature profiles with a flat power profile and the temperature profiles with a peaked power profile are especially visible for the HZP transient. Initially, the peaked power profile leads to a maximum in the fuel temperature near the fuel surface. The effect of another expression for the effective fuel temperature can be estimated by studying the temperature profiles (figures 7.7 and 7.8). An expression for the effective fuel temperature which uses a higher weight for the temperature in the outer zone leads to a larger fuel temperature effect in the beginning of the transient.

It is obvious that the calculation of such an expression for the effective fuel temperature for fuel at a certain burnup is a complicated task due to the radial distributions of the different nuclides. The next section shortly discusses this problem by looking at the different reaction rates in the fuel.

7.4 Reaction rates in fuel with a certain burnup

When the power profile in the fuel pin is known, the question arises how to find an expression for the effective fuel temperature. Evidently, this can be solved by using the brute-force method (section 6.5) for fuel at a certain burnup, but it is much more interesting to establish the effects that are important.

Therefore, the most important reaction rates in the slowing-down energy range in the 44.3 MWd/kgU PWR fuel of the previous section are considered. Table 7.5 shows the different reaction rates at a uniform fuel temperature of 841 K for the energy range between 3.38 eV and 3.35 keV. These reaction rates have been normalized to one neutron slowing down per second in the pin cell. Obviously, the capture rate in ^{238}U dominates.

Table 7.5: *Reaction rates (3.38 eV - 3.35 keV) in 44.3 MWd/kgU PWR fuel at a uniform fuel temperature of 841 K, normalized to 1 neutron slowing down per second in the pin cell.*

Isotope	Reaction rates	
	Capture (s^{-1})	Fission (s^{-1})
^{235}U	$3.3 \cdot 10^{-3}$	$5.9 \cdot 10^{-3}$
^{236}U	$8.5 \cdot 10^{-3}$	
^{238}U	$1.7 \cdot 10^{-1}$	
^{239}Pu	$6.4 \cdot 10^{-3}$	$8.3 \cdot 10^{-3}$
^{240}Pu	$3.1 \cdot 10^{-3}$	
^{241}Pu	$1.3 \cdot 10^{-3}$	$4.2 \cdot 10^{-3}$

Table 7.6 shows the variations of these reaction rates with fuel temperature.

Table 7.6: *Dependence of reaction rates (3.38 eV - 3.35 keV) on fuel temperature for 44.3 MWd/kgU PWR fuel; difference between $T_F = 841$ K and $T_F = 600$ K.*

| | Difference reaction rates | |
Isotope	Capture (s^{-1})	Fission (s^{-1})
^{235}U	$-2.7 \cdot 10^{-5}$	$-3.3 \cdot 10^{-5}$
^{236}U	$1.6 \cdot 10^{-4}$	
^{238}U	$5.1 \cdot 10^{-3}$	
^{239}Pu	$-2.0 \cdot 10^{-5}$	$-3.4 \cdot 10^{-5}$
^{240}Pu	$-4.4 \cdot 10^{-5}$	
^{241}Pu	$-9.0 \cdot 10^{-6}$	$-3.6 \cdot 10^{-5}$

Again, the capture rate in ^{238}U dominates the temperature effect. Moreover, because of the increase of the capture by ^{238}U most other reaction rates even decrease.

It seems justified to calculate the effective fuel temperature by only studying the radial distribution of ^{238}U. Further research on this subject is necessary to confirm this.

In the discussion above the slowing-down energy range, which comprises the important resonances of ^{238}U, has been considered. However, when transient calculations are done with more energy groups, the distributions of other nuclides than ^{238}U might be important to calculate effective fuel temperatures for specific energy ranges.

7.5   Conclusions

Calculations of the radial distributions of the nuclide densities are necessary to determine the power profile in a fuel pin. Important advantages of the treatment of resonance absorption with ROLAIDS-CPM are the detailed calculation of the space-dependence and the correct treatment of the overlap of resonances of different nuclides. Comparisons with experimental results show that these calculations can be done very accurately with ROLAIDS-CPM/XSDRN/ORIGEN.

Further research is necessary to estimate the error that is made in the calculational method. From the results of chapter 5 it is for example known that the ROLAIDS-XSDRN sequence with the XMAS group structure overestimates the resonance absorption by some 2 %, which worsens our comparison with the experimental results. However, our good agreement may partly also be due to some cancellation of errors. The burnup steps, the update steps, and the accuracy of

the reproduction of reaction rates by the one-group cross sections in ORIGEN are important in this context.

ORIGEN cannot treat radial variations of the nuclide densities implicitly, which makes the calculational method very complicated. Further effort would be necessary to implement the treatment of the radial variations of the nuclide densities in our code system for regular use. Changes of the power profile during burnup can then also be taken into account in a more correct way. This will speed up the calculation because then it will not be necessary to do extra pin-cell calculations.

Transient calculations show that a peaked power profile instead of a flat power profile leads to a lower average fuel temperature but to a higher cladding temperature. So, assuming a flat power profile is not conservative for transients in which the cladding temperature is the limiting factor.

Investigations of the Doppler effect in the fuel pin with a high burnup show that the Doppler effect is dominated by the resonance absorption in ^{238}U. So, it is expected that effective fuel temperatures can be computed by only considering the radial distribution of the ^{238}U concentration in the fuel pin.

Epilogue

This thesis deals with the Doppler effect in thermal nuclear reactors. The calculations have been done for pin cells which are characteristic for a Pressurized Water Reactor. However, the calculational methods used in this work can be applied to other types of thermal nuclear reactors such as Boiling Water Reactors, Heavy Water Reactors (CANDU), or graphite moderated reactors (HTR). Also, the results for these other types of thermal nuclear reactors can be analysed in the same way as in this thesis.

The calculations have been done for uranium oxide fuel in this work. Other types of fuel, such as mixed oxide fuel, or fuel with a mixture of actinides, can be analysed as well. The slowing-down code ROLAIDS-CPM is perfectly capable of handling a mixture of fuel nuclides because it treats resonance overlap correctly.

An interesting subject for further research is the treatment of the thermal motion of the heavy nuclides with respect to the scattering collisions (see section 3.3). Definitely, there is the need for a reference code which treats this correctly. Recent calculations [42] indicate that this effect increases resonance absorption in ^{238}U by about 1 % and the Doppler effect by about 9 %. This is quite large and will thus certainly have a large impact on calculations of the Doppler effect in reactor physics.

The methods which are applied in chapter 4 are recommended for the analysis of k-effective values or Doppler coefficients. Results from different reactor physics codes should be analysed in detail as in chapter 5. Very good agreement between k-effective values calculated by different reactor physics codes may well be due to cancellation of errors.

Recent calculations on a parabolic temperature distribution in the fuel pin with the correct treatment of the motion of the heavy nuclides [42], show that the effective temperature can be given as in equation 6.20 [42]. Although this expression cannot be used for arbitrary temperature profiles in a fuel pin, these results indicate that the effect of a temperature profile is not largely different when the motion of the heavy nuclides is modelled correctly. So, ROLAIDS-CPM can very well be used to study the influence of a temperature profile, when the limitations of this code are kept in mind. Reference calculations will be necessary.

It is very important to realize that the effective fuel temperature cannot be given as a combination of surface and central fuel temperature. Transient calculations indicate that the differences between a transient with a volume averaged effective fuel temperature or a transient with an effective fuel temperature calculated with a brute-force set of weights are quite small. So, it might not be necessary to determine a very accurate set of weights for the effective fuel temperature. The effect of a different expression for the effective fuel temperature can simply be analysed by considering the temperature profiles which occur during the transient. The impact of such a different expression on the transient will of course depend on the specific transient.

However, the effect of a temperature profile has only been studied in uranium oxide and only in a fuel pin which is characteristic for a PWR. The effective fuel temperatures for single resonances of ^{238}U depend strongly on the properties of the resonance. So, an important subject for further research is to investigate the influence of a temperature profile in other types of fuel, since nuclear resonances of nuclides other than ^{238}U are then important. Also other fuel pins should be considered, because the diameter of the fuel pin determines the blackness of the fuel pin for specific resonances.

In conclusion, the effect of a temperature profile in a fuel pin has been studied and analysed thoroughly for a specific UO_2 fuel pin. The physical effects which are important are discussed, which enables the understanding of the results. With this in mind, results for other types of fuel and other fuel pins can be analysed and understood more quickly.

We have also considered the radial power profile in the fuel pin. Although the influence of the radial power profile on the transients is small in our situation, the properties of the fuel, the cladding, and the gap might strongly influence this comparison. These properties and how these properties change with burnup lie outside the scope of this thesis, but the combination of fuel performance calculations with radial burnup calculations is certainly a subject for further research.

The calculational methods to calculate the radial power profile are available. However, because of the complicated calculational route which we need in our code system, we recommend to use a burnup code which treats the radial burnup effects implicitly.

Summary

In this thesis the Doppler effect in a thermal nuclear reactor is discussed. The Doppler effect is the phenomenon that the neutron absorption in the nuclear resonances of the fuel nuclides increases when the fuel temperature increases. It is the only feedback effect in a nuclear reactor which is both inherent and prompt. In chapter 2 a short theoretical introduction on resonance absorption and the Doppler effect is given.

Calculations have primarily been done for the Doppler effect in a Pressurized Water Reactor. The Doppler effect has been studied in a pin cell, which is the smallest possible unit cell in a nuclear reactor. Axially, an infinite length is usually assumed in the pin-cell calculations. In a Light Water Reactor such a pin cell consists of the fuel (diameter about 1 cm), the cladding, and an amount of water, which serves both as coolant and as moderator.

The main motivation for this study lies in the behaviour of a nuclear reactor during fast reactivity initiated transients; fast changes in the nuclear power due to a sudden increase of the multiplication factor for the nuclear chain reaction in the reactor, e.g. the ejection of a control rod. These transients are initially limited by the Doppler effect.

Under normal conditions the radial temperature profile in a fuel pin is nearly parabolic. During a transient the radial temperature profile in a fuel pin changes. However, this temperature profile cannot be modelled exactly in reactor physics codes which are used for transient calculations. These codes use effective fuel temperatures for the fuel pins. However, it is not known how effective fuel temperatures should be defined for arbitrary temperature profiles. In this thesis the calculation of these effective fuel temperatures is an important subject.

To do these calculations the slowing-down code ROLAIDS has been adapted. First, the collision probability method has been implemented in this code to enable a very accurate calculation of resonance absorption rates. Secondly, it has been made possible to use different temperatures for one nuclide, which enables the specification of a temperature profile in a fuel pin. The new code ROLAIDS-CPM as well as other codes which have been used in this study are described in chapter 3.

The effect of the fuel temperature on the reactivity is often expressed in terms of the fuel temperature coefficient. In chapter 4 it is shown that this fuel temperature coefficient should be defined from the results of pin-cell calculations by calculating the relative variation of the multiplication factor with the fuel temperature, which is different from the original definition. With the new definition it is shown that the Doppler effect hardly depends on the fuel enrichment for low enriched fuel. Also, the fuel temperature effect is analysed by expressing the multiplication factor as a product of 4 factors (fourfactor formula) and by studying the temperature variation of each of these factors. The main contribution to the fuel temperature effect in UO_2 is the Doppler effect in the slowing-down energy range. So, the fuel temperature effect can be studied in detail by only considering this energy range.

ROLAIDS-CPM has been verified with very accurate Monte Carlo calculations (chapter 5) in a pin cell. The square pin cell is approximated by a cylindrical pin cell with equal volume, because ROLAIDS-CPM can only handle one-dimensional geometries. The influence of this Wigner-Seitz assumption has been calculated with Monte Carlo calculations. The differences between the ROLAIDS-CPM results and the Monte Carlo results are very small, especially in relation with the error that is made by using the Wigner-Seitz assumption. The small differences are caused by the assumptions of flat and isotropic scattering sources in ROLAIDS-CPM.

Calculations with the discrete ordinates transport code XSDRN, a code which does not use an energy-pointwise representation of the cross sections, but in which the energy range is divided in a number of energy groups for which effective cross sections have to be calculated in advance (e.g. by ROLAIDS-CPM), show that the accuracy of the results strongly depends on the energy mesh. Especially the energy mesh for the largest resonances of ^{238}U is important.

In chapter 6 the effective fuel temperature in fresh UO_2 fuel is considered. First, based on a literature survey, two theoretical expressions to calculate the effective fuel temperature for arbitrary temperature profiles are derived. Assuming high absorption leads to the so-called chord averaged fuel temperature, assuming low absorption leads to the volume averaged fuel temperature. It is important to realize that an expression based on a combination of surface and central fuel temperature cannot be used for an arbitrary temperature profile.

Calculations on a UO_2 slab show that the deviations from the theoretical expressions depend on the specific resonance and are very complicated. These deviations have been analysed to enable a better understanding of the results. The results can be understood by studying the mean free path for the resonance energies and by studying the fraction that absorption contributes to the total reaction rate. Obviously, a brute-force approach is necessary to enable the determination of an accurate expression for the effective fuel temperature as a function of the temperatures in the different zones.

Such a brute-force approach is used for calculations on a UO_2 pin. The

effective fuel temperature is defined as a weighted sum of the temperatures in 10 fuel zones with equal volumes. The weights have been determined with the least squares method. The weights for the effective fuel temperature for the whole slowing-down energy range are almost equal to the weights for the chord averaged fuel temperature. However, this appears to be coincidence since the weights for separate large resonances do not agree with this theoretical expression. The effective fuel temperature in the high-energy range is about equal to the volume averaged fuel temperature.

Transient calculations with different expressions for the effective fuel temperature show that the differences are small, except when the effective fuel temperature is defined as a combination of surface and central fuel temperature. Reference calculations with the actual temperature profiles in a transient show that the effective fuel temperatures calculated by the brute-force set of weights are very accurate. It is also shown that the small differences between the transients can be explained by studying the temperature profiles which occur during the transient.

Chapter 7 deals with another non-uniformity in the fuel pin: the power profile. This power profile is peaked towards the surface of the fuel pin due to burnup. Burnup calculations have been done to determine the radial distributions of different isotopes. Comparisons with known experimental results show that these calculations are very accurate for the important isotopes. The calculated power profiles have been used to calculate the influence of such a power profile on the transients from chapter 6. A peaked power profile leads to a lower fuel temperature during the transient, but it causes a higher peak cladding surface temperature.

Samenvatting

In dit proefschrift staat het Doppler-effect in een thermische kernreactor centraal. Dit Doppler-effect is een belangrijk verschijnsel, omdat dit het enige terugkoppel-effect is in een kernreactor dat zowel inherent als instantaan is. Bij een stijgend vermogen in een kernreactor neemt de temperatuur van de splijtstof toe. Door de Doppler-verbreding van nucleaire resonanties van de splijtstof leidt de stijgende temperatuur tot een toename in de absorptiesnelheid van neutronen. Deze toegenomen absorptiesnelheid heeft dan weer een remmende werking op de vermogenstoename. In hoofdstuk 2 wordt voor de niet ingewijde lezer een korte theoretische inleiding over resonantie-absorptie en het Doppler-effect gegeven.

Berekeningen aan het Doppler-effect zijn voornamelijk gedaan voor een drukwaterreactor (PWR). In een drukwaterreactor is de reactorkern opgebouwd uit een aantal splijtstofelementen (b.v. ≈ 200), die op hun beurt bestaan uit een verzameling van splijtstofpennen (b.v. 17 x 17). Een splijtstofpen, die bestaat uit een huls waarbinnen tabletten splijtstof liggen opgestapeld, heeft een lengte van een paar meter en een diameter van ongeveer een centimeter. Tussen de splijtstofpennen bevindt zich het koelwater. Naast de functie van koelmiddel heeft het water nog een andere belangrijke functie, namelijk die van moderator. De neutronen met een hoge energie die bij splijting ontstaan moeten namelijk afgeremd worden tot lage (thermische) energie, waar ze nieuwe splijtingen kunnen teweegbrengen. In dit onderzoek wordt het Doppler-effect bestudeerd in een eenheidscel, die bestaat uit een splijtstofpen met daaromheen een representatieve hoeveelheid water.

De belangrijkste reden om het Doppler-effect in dit onderzoek nader te bekijken is het gedrag van een kernreactor tijdens een snelle vermogenstoename, die bijvoorbeeld veroorzaakt zou kunnen worden door de uitstoot van een regelstaaf. De vermogenstoename in zulke transiënten wordt beperkt door het Doppler-effect.

Onder normale omstandigheden is het temperatuurprofiel in een splijtstofpen vrijwel parabolisch, maar tijdens een transiënt verandert dit profiel sterk. Echter, dit veranderend temperatuurprofiel wordt niet exact gemodelleerd in programma's die het verloop van dergelijke transiënten uitrekenen. Deze programma's gebruiken effectieve splijtstoftemperaturen voor de neutronicaberekening. Het is echter niet bekend hoe de effectieve splijtstoftemperaturen zouden moeten worden

bepaald voor willekeurige temperatuurprofielen. De bepaling van de effectieve splijtstoftemperaturen is dan ook een belangrijk onderwerp in dit proefschrift.

Om deze bepaling nauwkeurig te kunnen doen, is een bestaand programma (ROLAIDS) aangepast. Dit programma beschrijft het gedrag van neutronen tijdens het afremmen van hoge naar lage energie. Naast een verbeterde rekenmethode is het in het verbeterde programma (ROLAIDS-CPM) mogelijk om een temperatuurprofiel in de splijtstofpen te modelleren. ROLAIDS-CPM en de overige programma's die in deze studie zijn gebruikt, worden beschreven in hoofdstuk 3.

Een gebruikelijke manier om het Doppler-effect weer te geven is de splijtstoftemperatuurcoëfficient. In hoofdstuk 4 wordt aangetoond dat voor eenheidscelberekeningen een alternatieve definitie van deze coëfficient moet worden gebruikt om een redelijke afschatting te krijgen van de grootte van het Doppler-effect. Met deze alternatieve definitie blijkt dat het Doppler-effect vrijwel onafhankelijk is van de verrijking voor licht verrijkte splijtstof. Bovendien wordt in hoofdstuk 4 het Doppler-effect bestudeerd door de splijtstoftemperatuurcoëfficient uit te splitsen in verschillende componenten. Verreweg de grootste bijdrage tot deze coëfficient blijkt dan inderdaad het Doppler-effect te zijn in het energiegebied dat met ROLAIDS-CPM kan worden bestudeerd.

Verificatie van ROLAIDS-CPM is gedaan door gedetailleerde berekeningen met dit programma te vergelijken met nauwkeurige Monte-Carlo-berekeningen. Dit wordt beschreven in hoofdstuk 5. Omdat in ROLAIDS-CPM slechts eendimensionale geometrieën kunnen worden gemodelleerd, moet de in werkelijkheid vierkante eenheidscel worden benaderd door een cylindrische eenheidscel. Het effect van deze zogenaamde Wigner-Seitz-benadering is met de Monte-Carlo-methode berekend. De verschillen tussen de resultaten die met ROLAIDS-CPM worden verkregen en de resultaten die met de Monte-Carlo-methode worden verkregen, zijn erg klein, vooral in vergelijking met de fout die door de Wigner-Seitz-benadering wordt gemaakt. Bovendien kunnen deze kleine verschillen worden toegeschreven aan de aannames die in ROLAIDS-CPM worden gemaakt.

De effectieve splijtstoftemperatuur van uraniumoxide (UO_2) wordt bekeken in hoofdstuk 6. Allereerst worden op grond van een literatuuroverzicht twee theoretische modellen afgeleid om de effectieve splijtstoftemperatuur voor een willekeurig temperatuurprofiel in de splijtstof te berekenen. De zogenaamde koordegemiddelde splijtstoftemperatuur wordt verkregen, wanneer veel absorptie wordt verondersteld, en de volumegemiddelde splijtstoftemperatuur wordt verkregen, wanneer weinig absorptie wordt verondersteld. In ieder geval is het belangrijk dat men zich realiseert dat een uitdrukking die gebaseerd is op een combinatie van de temperatuur in het centrum van de pen en de temperatuur aan het oppervlak, zeker niet gebruikt kan worden. Echter, deze uitdrukking wordt wel dikwijls toegepast.

Berekeningen aan een plaatje UO_2 laten zien dat de afwijkingen van de theoretische uitdrukkingen zeer ingewikkeld zijn en sterk afhangen van de nucleaire

resonantie die bekeken wordt. Deze afwijkingen zijn in hoofdstuk 6 verder ge-analyseerd om een beter begrip te krijgen van de effecten die een rol spelen. Het is in ieder geval duidelijk dat de bepaling van een uitdrukking die de effectieve splijt-stoftemperatuur nauwkeurig berekent voor een willekeurig temperatuurprofiel, gebaseerd zal moeten zijn op een grote set berekeningen aan temperatuurprofie-len.

Deze aanpak is dan ook gebruikt om een uitdrukking te vinden voor de ef-fectieve temperatuur in een UO_2-pen. Voor het hele beschouwde energiegebied blijkt deze uitdrukking vrijwel gelijk te zijn aan de koordegemiddelde effectieve splijtstoftemperatuur. Echter, dit is toeval, omdat dit niet meer opgaat voor af-zonderlijke resonanties. Wel geldt dat in het hoge-energiegebied de effectieve temperatuur ongeveer gelijk is aan de volumegemiddelde temperatuur.

Transiëntberekeningen met verschillende uitdrukkingen voor de effectieve temperatuur laten zien dat de verschillen vrij klein zijn, behalve dan voor een effectieve temperatuur die bepaald wordt uit een combinatie van oppervlakte- en centrum-temperatuur. Referentieberekeningen met de temperatuurprofielen die tijdens de transiënt voorkomen, laten zien dat de effectieve temperaturen die be-rekend worden met de door ons bepaalde uitdrukking, zeer nauwkeurig zijn. De kleine verschillen tussen de transiënten kunnen goed worden begrepen door de temperatuurprofielen tijdens de transiënt te bekijken.

In hoofdstuk 7 wordt ten slotte aandacht besteed aan de vermogensverdeling over de splijtstofpen. Wanneer een splijtstofpen pas in de reactor staat, zal deze verdeling nog vrijwel vlak zijn, maar na een tijdje ontstaat er een piek in de ver-mogensverdeling aan de rand van de splijtstofpen ten gevolge van de inhomogene opbouw van het splijtbare plutonium. We hebben berekeningen gedaan om de concentraties van verschillende nucliden als functie van de positie in de splijtstof-pen te bepalen. Deze berekeningen bleken goed overeen te komen met bekende experimentele resultaten. De berekende vermogensprofielen zijn gebruikt om de invloed van deze profielen op de transiënt uit hoofstuk 6 te bepalen. Het gepiekte vermogensprofiel leidt tot een lagere splijtstoftemperatuur, maar tot een hogere temperatuur van de hulswand.

Nomenclature

List of Symbols

a	slab width	m
a	radius	m
a	thermal absorption rate in the system normalized to $\frac{1}{k}$ times the fission source	
$a_{k,j}$	parameter used in slowing-down calculation	
d	zone width	m
f	thermal utilization factor	
$f(L)$	chord length distribution	m^{-1}
g	statistical spin factor	
$g(\vec{r}_s, \vec{\Omega})$	probability distribution for the chords	m^{-2}
k	multiplication factor	
k'	local multiplication factor	
k''	infinite multiplication factor divided by average infinite multiplication factor	
k_0	multiplication factor at time zero	
k_∞	infinite multiplication factor	
k_B	Boltzmann's constant ($k_B = 1.3807.. \cdot 10^{24}$)	$J\,K^{-1}$
l	distance along a chord	m
$\vec{n}$	surface normal (unit vector)	
n_{prod}	neutron produktion rate by non-thermal fissions	s^{-1}
n_{prod}^5	neutron production rate by non-thermal fissions of ^{235}U	s^{-1}
n_{prod}^8	neutron production rate by non-thermal fissions of ^{238}U	s^{-1}
$n(E)$	neutron density per unit energy interval	$m^{-3}J^{-1}$
p	resonance escape probability	
p_i	escape probability for energy range i	
$p(E)$	escape probability to energy E	

$p(Y)$	distribution of the lengths of the projected chords on the diametral plane of a cylinder	m^{-1}
q	slowing-down density	$m^{-3}s^{-1}$
r	radial distance to the centre of a cylinder	m
$s(E, \vec{\Omega})$	angular neutron source density per unit energy interval	$m^{-3}s^{-1}J^{-1}$
t	time variable	s
t_{prod}	neutron produktion rate by thermal fissions	s^{-1}
u	lethargy variable	
v	neutron velocity	$m\ s^{-1}$
w_i	weights to calculate effective fuel temperatures	
x	dimensionless variable used in Doppler broadening	
y	dimensionless variable used in Doppler broadening	
y	distance along the projection of the chord on the diametral plane of a cylinder	m
z	length variable	m
A	nuclear mass in units of the neutron mass	
A_i	absorption rate density in energy range i	$m^{-3}s^{-1}$
$A(l, T)$	absorption rate density at position l with temperature T	$m^{-3}s^{-1}$
C	constant used to describe asymptotic flux	$m^{-2}s^{-1}$
C_d	precursor concentration in delayed neutron precursor group d	m^{-3}
C_j	collision rate in zone j	s^{-1}
C_D	Dancoff-Ginsberg factor	
CC	coupling coefficient	m^{-1}
E	energy variable	J
E_0	resonance energy	J
E_i	lower energy boundary for energy range i	J
E_{max}	maximum source energy	J
E_{ref}	reference energy for the lethargy scale	
E_C	neutron kinetic energy in the CM system	J
I	resonance integral	m^2
I_i	resonance integral for energy range i	m^2
J	function used to calculate resonance integrals	
J_j^+	out-going neutron current (zone j to zone $j+1$)	s^{-1}
J_j^-	in-going neutron current (zone $j+1$ to zone j)	s^{-1}
L_g	leakage term for energy group g	$m^{-3}s^{-1}$
L	chord length	m
$L(\vec{r}_s, \vec{\Omega})$	chord length of the chord at position $\vec{r}_s$ and with direction $\vec{\Omega}$	m

M	nuclear mass	kg
N	nuclide density	m^{-3}
P_{esc}	neutron escape probability from the fuel	
P_j	escape probability for zone j	
$P_{j,i}$	neutron first collision probability from zone j to zone i	
P_A	absorption probability	
P_{FM}	neutron first collision probability from the fuel to the moderator in the two-zones model	
$P(\vec{V}, T)$	nuclear velocity distribution at temperature T	$s^3\,m^{-3}$
S	surface area	m^2
S_0	total neutron source density	$m^{-3}s^{-1}$
S_j	slowing-down source in zone j	s^{-1}
$S(E)$	neutron source density per unit energy interval	$m^{-3}J^{-1}s^{-1}$
T	temperature	K
T_c	central fuel temperature	K
T_c'	central fuel temperature along a chord	K
T_j	transmission probability for zone j	
T_i	temperature in zone i	K
T_{inner}	temperature in the inner fuel zone	K
T_{outer}	temperature in the outer fuel zone	K
T_s	surface fuel temperature	K
T_F	fuel temperature	K
$T_{F,eff}$	effective fuel temperature	K
V	volume	m^3
V	nuclide velocity	$m\,s^{-1}$
Y	length of the projection of a chord on the diametral plane of a cylinder	m
α	parameter related to the nuclear mass	
α_F	fuel temperature coefficient	K^{-1}
α_F^*	alternative fuel temperature coefficient	K^{-1}
β	dimensionless parameter used in the J-function	
β	total delayed neutron fraction	
β_d	delayed neutron fraction in delayed neutron precursor group d	
γ_{ji}	fission yield of nuclide i due to fission of nuclide j	
ϵ	fast fission factor	
ϵ^*	non-thermal fission factor	
η	number of neutrons produced per thermal neutron absorbed in the fuel	
ζ	dimensionless variable used in Doppler broadening	

ζ_{eff}	value of ζ for the effective fuel temperature	
ζ_{max}	maximum value of ζ in a slab	
ζ'_{max}	maximum value of ζ along a chord	
ϑ	angle between the inward normal and the projection of a chord on the diametral plane of a cylinder	
θ	dimensionless variable used in an analytic model for the effective fuel temperature	
θ_{eff}	value of θ for the effective fuel temperature	
λ_0	neutron wavelength for the resonance energy	m
λ_C	neutron wavelength in the CM system	m
λ	decay constant	s^{-1}
$\lambda_{l\rightarrow i}$	decay constant for decay from nuclide l to nuclide i	s^{-1}
μ	optical width	
ν	average number of neutrons produced per fission	
ξ	average lethargy gain per collision	
π	mathematical constant ($\pi = 3.14159...$)	
ρ	reactivity	
σ	standard deviation	
σ	microscopic cross section	m^2
σ_0	value of the total cross section at the resonance energy	m^2
σ_a	absorption cross section	m^2
$\sigma_{a,k\rightarrow i}$	absorption cross section which transmutes nuclide k into nuclide i	m^2
σ_e	escape cross section	m^2
σ_{eff}	effective group cross section	m^2
σ_f	fission cross section	m^2
σ_p	potential scattering cross section	m^2
σ_t	total cross section	m^2
σ_γ	radiative capture cross section	m^2
τ	dimensionless parameter used to describe a parabolic temperature profile in a slab	
τ'	dimensionless parameter used to describe a parabolic temperature profile along a chord	
$\varphi(E, \vec{\Omega})$	angular neutron flux per unit energy interval	$m^{-2}s^{-1}J^{-1}$
$\phi(u)$	neutron flux per unit lethargy	$m^{-2}s^{-1}$
ϕ_g	neutron flux in energy group g	$m^{-2}s^{-1}$
ϕ_j	neutron flux in zone j	$m^{-2}s^{-1}$
ϕ_t	total neutron flux	$m^{-2}s^{-1}$
ϕ_u	constant flux per unit lethargy	$m^{-2}s^{-1}$
$\phi(E)$	neutron flux per unit energy interval	$m^{-2}s^{-1}J^{-1}$
ψ	function to describe the Bethe-Placzek cross section	

χ	function used in an analytic model model for the effective fuel temperature	
$\chi(E)$	fission spectrum	
Γ	total level width	J
Γ_0	total level width at the resonance energy	J
Γ_n	neutron level width	J
Γ_{n0}	neutron level width at the resonance energy	J
Γ_D	Doppler width	J
Γ_γ	partial level width for gamma emission	J
Σ	macroscopic cross section	m^{-1}
Σ_a	macroscopic absorption cross section	m^{-1}
Σ_f	macroscopic fission cross section	m^{-1}
Σ_p	macroscopic potential scattering cross section	m^{-1}
Σ_r	macroscopic removal cross section	m^{-1}
Σ_t	macroscopic total cross section	m^{-1}
Σ_s	macroscopic scattering cross section	m^{-1}
$\Sigma_s(E' \to E)$	macroscopic cross section for scattering from energy E' to energy E	$m^{-1}J^{-1}$
$\Sigma_s(E' \to E, \vec{\Omega}' \to \vec{\Omega})$	double differential scattering cross section	$m^{-1}J^{-1}$
$\Sigma_{s_{i,j}}$	macroscopic scattering cross section from group i to group j	m^{-1}
$\vec{\Omega}$	neutron direction (unit vector)	

Operators

F	fission operator
M	migration and loss operator
$\overline{x}$	average value of x
∇x	gradient of x
$\vec{a} \bullet \vec{b}$	inproduct of $\vec{a}$ and $\vec{b}$

List of abbreviations

b	barn (10^{-28} m^2)
pcm	10^{-5}
ppm	parts per million
BOL	Beginning Of Life
CANDU	CANada Deuterium Uranium reactor
CM	Centre of Mass
CPM	Collision Probability Method
ENDF	Evaluated Nuclear Data File
EPMA	Electron Probe Micro Analysis
MWd/kgU	megawatt-day per kg uranium
HFP	Hot Full Power
HTR	High Temperature Reactor
HZP	Hot Zero Power
JEF	Joint Evaluated File
LAB	Laboratory
LWR	Light Water Reactor
PENDF	Pointwise Evaluated Nuclear Data File
PWR	Pressurized Water Reactor
ROLAIDS	Resonance OverLap Analysis In Discretely represented Systems

References

[1] H.L. Anderson, E. Fermi & L. Szilard, "Neutron Production and Absorption in Uranium," *Phys. Rev.* **56** (1939), 284–286.

[2] L.A. Turner, "Nuclear Fission," *Rev. Mod. Phys.* **12** (1940), 1–29.

[3] E. Creutz, H. Jupnik, T. Snyder & E.P. Wigner, "Review of the Measurements of the Resonance Absorption of Neutrons by Uranium in Bulk," *J. Appl. Phys.* **26** (1955), 257–259.

[4] K.O. Ott & R.J. Neuhold, *Introductory Nuclear Reactor Dynamics*, American Nuclear Society, Illinois, USA, 1985.

[5] B. Pershagen, *Light Water Reactor Safety*, Pergamon Press, Oxford, UK, 1989.

[6] H. van Dam, "Physics of Nuclear Reactor Safety," *Rep. Prog. Phys.* **11** (1992), 2025–2077.

[7] Nuclear Electric, "PANTHER Reference Manual," TNGF/REP/0004/93, Berkeley, UK, 1993.

[8] R.D. Lawrence, "Progress in Nodal Methods for the Solution of the Neutron Diffusion Equation and Transport Equations," *Prog. Nucl. Energy* **17** (1986), 271–301.

[9] K.S. Smith, "Assembly Homogenization Techniques for Light Water Reactor Analysis," *Prog. Nucl. Energy* **17**, 303–335.

[10] F.C.M. Verhagen, "Ontwikkeling en validatie van een fijnmazig kernmodel voor de kerncentrale in Borssele," KEMA Nucleair, 60118-RS 88-4019, Arnhem, The Netherlands, 1988.

[11] C. Ahnert & J.M. Aragones, "Fuel Management and Core Design Code Systems for Pressurized Water Reactor Neutronic Calculations," *Nucl. Technol.* **69** (1985), 350–366.

[12] A. Reichel & A. Keane, "Resonance Absorption in a Cylindrical Fuel Rod with Radial Temperature Variation," *Proc. Roy. Soc. N.S.W.* **94** (1961), 215–225.

[13] A. Reichel, "The Effect of Non-Uniform Fuel Rod Temperatures on Effective Resonance Integrals," Atomic Energy Establishment, AEEW - R 76, Winfrith, Dorset, UK, 1961.

[14] G. Rowlands, "Resonance Absorption and Non-Uniform Temperature Distributions," *J. Nucl. Energy Parts A/B* **16** (1962), 235–236.

[15] J.J. van Binnebeek, "Resonance Integral and Doppler Coefficients in Nonuniform Cylindrical Reactor Fuel Rods," *Nucl. Sci. Eng.* **36** (1969), 47–58.

[16] L. Dresner, "Some Remarks on the Effect of a Nonuniform Temperature Distribution on the Temperature Dependence of Resonance Absorption," *Nucl. Sci. Eng.* **1** (1961), 39–42.

[17] J.E. Olhoeft, "Evaluation of Nuclear Effective Temperature in Thermal Power Reactor Fuel," *Trans. Am. Nucl. Soc.* **13** (1970), 306–307.

[18] K. Smith, "Modern Reactor Core Design Codes and Comparison to Measured Data," *Proc. Joint Conf. Mathematical Methods and Supercomputing in Nuclear Applications* **1** (1993), 479–495.

[19] H. Carlsen & D.N. Sah, "Radial Concentration and Effect on Temperature of Plutonium Formed in UO_2 During Irradiation," *Nucl. Technol.* **55** (1981), 587–593.

[20] R.J. Guenther, D.E. Blahnik, U.P. Jenquin, J.E. Mendel, L.E. Thomas & C.K. Thornhill, "Characterization of Spent Fuel Approved Testing Material–ATM-104," Pacific Northwest Laboratory, PNL–5109-104, Richland, Washington, USA, 1991.

[21] G. Breit & E. Wigner, "Capture of Slow Neutrons," *Phys. Rev.* **49** (1936), 519–531 .

[22] R. Labauve, C. Lubitz, R. Macfarlane, S. Pearlstein, R. Peelle, R. Roussin & L. Stewart, "ENDF-102 Data Formats and Procedures for the Evaluated Nuclear Data File ENDF-6," BNL-NCS 44945, 1990 (Revised 10/91).

[23] H. Tellier, "Multilevel Effect in Uranium-238 and Thorium-232 Effective Neutron Capture Resonance Integrals," *Nucl. Sci. Eng.* **79** (1981), 393–403.

[24] J.J. Duderstadt & L.J. Hamilton, *Nuclear Reactor Analysis*, John Wiley & Sons, New York, USA, 1976.

[25] W.E. Lamb Jr., "Capture of Neutrons in a Crystal," *Phys. Rev.* **55** (1939), 190–197.

[26] L. Dresner, *Resonance Absorption in Nuclear Reactors*, International Series of Monographs on Nuclear Energy, Pergamon Press, Oxford, UK, 1960.

[27] R.L. Murray, "The Reaction Rate of Neutrons in a Maxwellian Medium," *Nucl. Sci. Eng.* **26** (1966), 362–365.

[28] H.A. Bethe & G. Placzek, "Resonance Effects in Nuclear Processes," *Phys. Rev.* **51** (1937), 450–484.

[29] R.J.J. Stamm'ler & M.J. Abbate, *Methods of Steady-State Reactor Physics in Nuclear Design*, Academic Press, London, 1983.

[30] G.I. Bell & S. Glasstone, *Nuclear Reactor Theory*, Van Nostrand Reinhold Company, New York, USA, 1970.

[31] Argonne National Laboratory, "Reactor Physics Constants," United States Atomic Energy Commission, ANL-5800 Second Edition, 1963.

[32] R.E. MacFarlane, D.W. Muir & R.M. Boicourt, "The NJOY Nuclear Data Processing System," Los Alamos National Laboratory, USA, LA-9303-M (ENDF 324), 1982.

[33] J.F. Briesmeister, ed., "MCNP-A General Monte Carlo Code for Neutron and Photon Transport," Los Alamos National Laboratory, USA, LA-7396-M, Rev. 2, 1986.

[34] W.J.M. de Kruijf, "ROLAIDS-CPM: A Code for Accurate Resonance Absorption Calculations," ECN-R–93-013, Petten, The Netherlands, 1993.

[35] L.M. Petrie & N.M. Greene, "XSDRNPM: AMPX module with one dimensional S_n capability for spatial weighting.," ORNL/RSIC-PSR-63, 1978.

[36] M.J. Bell, "ORIGEN - The ORNL Isotope Generation and Depletion Code," Oak Ridge National Laboratory, ORNL-4628, 1973.

[37] M.J. Halsall, "LWR-WIMS, A Computer Code for Light Water Reactor Lattice Calculations," Atomic Energy Establishment , AEEW - R 1498, Winfrith, Dorset, UK, 1982.

[38] H. Tellier, M. Coste, C. Raepsaet & C. Van der Gucht, "Heavy Nucleus Resonant Absorption Calculation Benchmarks," *Nucl. Sci. Eng.* **113** (1993), 20–30.

[39] R.D. Mosteller, L.D. Eisenhart, R.C. Little, W.J. Eich & J. Chao, "Benchmark Calculations for the Doppler Coefficient of Reactivity," *Nucl. Sci. Eng.* **107** (1991), 265–271.

[40] R.D. Mosteller, J.T. Holly & L.A. Mott, "Benchmark Calculations for the Doppler Coefficient of Reactivity in Mixed-Oxide Fuel," *Proc. Int. Topl. Mtg. Advances in Mathematics, Computations, and Reactor Physics*, Pittsburgh, USA (1991).

[41] M. Ouisloumen & R. Sanchez, "A Model for Neutron Scattering off Heavy Isotopes That Account for Thermal Agitation Effects ," *Nucl. Sci. Eng.* **107** (1991), 189–200.

[42] O. Bouland, V. Kolesov & J.L. Rowlands, "The Effect of Approximations in the Energy Distributions of Scattered Neutrons on Thermal Reactor Doppler Effects," *Proc. Int. Conf. Nuclear Data for Science and Technology*, Gatlinburg, USA (1994).

[43] W. Rothenstein, "Effect of Upscattering by Heavy Nuclides on Doppler Changes of Resonance Absorption," *Proc. Int. Conf. Reactor Physics and Computations*, Tel-Aviv, Israel (1994).

[44] R.M. Westfall & M.A. Bjerke, "An Interface-Currents Integral Treatment for Treating Doubly Heterogeneous Multisystem Geometries ," *Proc. Topl. Mtg. Computational Methods in Nuclear Engineering* **II** (1979), 7–71.

[45] J.A. Bucholz, "An Analytical Angular Integration Technique for Generating Multigroup Transfer Matrices," *Nucl. Sci. Eng.* **74** (1980), 163–167.

[46] I. Carlvik, "A method for Calculating Collision Probabilities in General Cylindrical Geometry and Applications to Flux Distributions and Dancoff Factors," *Proc. Int. Conf. Peaceful Uses of Atomic Energy* **3** (1964), P/681.

[47] W.G. Bickley & J. Nayler, "A Short Table of the Functions $Ki_n(x)$, from n=1 to n=16. ," *Phil. Mag.* **20** (1935), 343–347.

[48] N.M. Greene, "BONAMI-S: Resonance Self-Shielding by the Bondarenko Method," NUREG/CR-0200, Volume 2, Section F1, ORNL/NUREG/CSD-2/V2, 1981.

[49] R.M. Westfall, I.M. Petrie, N.M. Greene & J.L. Lucius, "NITAWL-S: Scale System Module for Performing Resonance Shielding and Working Library Production," NUREG/CR-0200, Volume 2, Section F2, ORNL/NUREG/CSD-2/V2, 1981.

[50] L.W. Nordheim, "The Theory of Resonance Absorption ," *Proc. Symposia in Applied Mathematics* **XI** (1961), 58–88.

[51] M.J. Roth, "The WIMS-E Modules W-PRES and W-RES," Atomic Energy Establishment, , AEEW - R 1707, Winfrith, Dorset, UK , 1983.

[52] M.J. Roth, "Resonance Absorption in Complicated Geometries," Atomic Energy Establishment, , AEEW - R 921, Winfrith, Dorset, UK, 1974.

[53] J. Lewins, *Nuclear Reactor Kinetics and Control*, Pergamon Press, Oxford, UK, 1978.

[54] W.J.M. de Kruijf & A.J. Janssen, "On the Definition of the Fuel Temperature Coefficient of Reactivity for Pin-Cell Calculations on an Infinite Lattice," *Ann. Nucl. Energy* **20** (1993), 639–648.

[55] J.R. Lamarsh, *Introduction to Nuclear Reactor Theory*, Addison Wesley, Reading, MA, 1966.

[56] S. Glasstone & A. Sesonske, *Nuclear Reactor Engineering*, Van Nostrand, Princeton, USA, 1955.

[57] R.C.L. van der Stad & H. Gruppelaar, "ECNJEF1, A JEF1 based 219-group cross-section library: User's Manual," ECN-I–92-032, Petten, The Netherlands, 1992.

[58] W.J.M. de Kruijf, "On the calculation of the fuel temperature coefficient of reactivity for a critical configuration," ECN-R–92-007, Petten, The Netherlands, 1992.

[59] W.J.M. de Kruijf & A.J. Janssen, "Detailed Resonance Absorption Calculations with the Monte Carlo Code MCNP and a Collision Probability Version of the Slowing Down Code ROLAIDS," *Proc. Int. Conf. Reactor Physics and Computations*, Tel-Aviv, Israel (1994).

[60] W.J.M. de Kruijf & A.J. Janssen, "Benchmark Calculations on Resonance Absorption by ^{238}U in a PWR pin-cell geometry," ECN-R–93-016, Petten, The Netherlands, 1993.

[61] H. Finnemann & A. Galati, "NEACRP 3-D LWR Core Transient Benchmark," OECD Nuclear Energy Agency, Final Specifications, NEACRP-L-335 (Revision 1), October 1991 (January 1992).

[62] G.M. Roe, "The Absorption of Neutrons in Doppler Broadened Resonances," General Electric Company, Knolls Atomic Power Laboratory, KAPL-1241, New York, USA, 1954.

[63] A. Keane, "Resonance absorption in a slab with a parabolic temperature distribution," Atomic Energy Research Establishment, AERE R/M 198, Harwell, Berkshire, UK, 1958.

[64] W.H. Arnold & R.A. Dannels, "The Doppler Coefficient of $U^{238}O_2$," *Trans. Am. Nucl. Soc.* **3** (1960), 229–230.

[65] P. Greebler & E. Goldman, "Doppler Calculations for Large Fast Ceramic Reactors," General Electric Company, Atomic Power Equipment Company, GEAP 4092, San Jose, California, USA, 1962.

[66] J. Codd, C. Durston & W.V. Wright, "Some Calculations of Fast Reactor Doppler and Sodium Loss Coefficients with Particular Reference to the Effects of Core Lattice Structure and Radial Fuel Temperature Distribution," *Proc. Conf. Safety, Fuels, and Core Design in Large Fast Power Reactors (ANL-7120)*, Argonne, Illinois, USA (1965).

[67] W.G. Pettus & M.N. Baldwin, "Doppler Coefficient Measurements on Th and ThO$_2$ Rods with Nonuniform Temeperature Distributions," *Nucl. Sci. Eng.* **26** (1966), 34–46.

[68] I.D. Palmer, K.W. Hesketh & P.A. Jackson, "A Model for Predicting the Radial Power Profile in a Fuel Pin," *IAEA Specialists' Mtg. on Water Reactor Fuel Element Performance Computer Modelling*, Preston, UK (1982).

[69] J.M. Aragones, "Detailed Calculations in Energy and Space of Effective Neutron Resonance Cross Sections," *Nucl. Sci. Eng.* **68** (1978), 281–298.

[70] R.C.L. van der Stad, Cai Chonghai, H. Gruppelaar & V. Lalov Lalov, "EJ2-XMAS, a JEF2.2 Based Neutron Cross Section Library in the XMAS Group Structure: User Manual," ECN-I-94-049, Petten, The Netherlands, 1994.

[71] J.L. Kloosterman, "New Working Libraries for Transmutation Studies," *Proc. Global '93*, Seattle, Washington, USA (1993).

[72] M.C. Brady, "Burnup Credit Criticality Benchmark, Part I-B Isotopic Prediction, Problem Specification," Nuclear Energy Agency, NEA/NSC/DOC(92)10/REV, 1992.

[73] H. Matzke, "On the rim effect in high burnup UO_2 LWR fuels," *J. Nucl. Mater.* **189** (1992), 141–148.

Dankwoord

Vanaf deze plaats wil ik alle mensen bedanken die direct of indirect hebben bijgedragen tot de totstandkoming van dit proefschrift. Allereerst wil ik mijn directe begeleider Dr. Ir. Ton Janssen bedanken voor zijn vele goede suggesties en de talloze kritische opmerkingen, die me telkens weer met de voeten op de grond brachten wanneer dat nodig was. Bovendien kon ik bij hem altijd terecht wanneer ik problemen had met reactorfysische theorie. Vooral "Duderstad" kwam vaak ter sprake.

Vervolgens wil ik Prof. Dr. Ir. H. van Dam en Dr. Ir. J.E. Hoogenboom bedanken, die me vanuit Delft van nuttige suggesties en kritiek hebben voorzien. De door hen begeleide onderwijsbijeenkomsten in Delft met andere promovendi hebben in belangrijke mate bijgedragen tot mijn opleiding.

Bij het ECN wil ik graag Dr. Harm Gruppelaar, Ir. Henk Klippel en alle (ex-)medewerkers van de groep fysica van geavanceerde reactoren bedanken voor de goede samenwerking in de afgelopen 4 jaar. Dankzij de vele hulp heb ik onder andere snel geleerd om met computers om te gaan.

Voor het wegwijs raken in de software van ons code-systeem en het onvermijdelijke "debuggen" ben ik veel dank verschuldigd aan Henk Oudshoorn. Als redder in de nood heeft hij problemen opgelost wanneer ik het helemaal niet meer zag zitten.

Verder wil ik mijn kamergenoot Hans Hendriks en de andere (ex-)leden van de HFR rekenclub bedanken voor de fijne werksfeer op de kamer. Zij stonden altijd klaar om te helpen waar nodig en spartelden nooit tegen wanneer ze mochten dienen als eerste klankbord voor mijn ideeën.

Tenslotte wil ik graag mijn ouders bedanken voor de ondersteuning die ze me altijd gegeven hebben tijdens mijn studie en mijn promotieonderzoek. Ook alle familieleden en vrienden die in moeilijke tijden hebben bijgesprongen wil ik hier bedanken.

En Joyce, waarom, gewoon daarom.

<div align="right">Willy de Kruijf</div>

Curriculum Vitae

Willy de Kruijf werd op 16 mei 1966 in 's-Hertogenbosch geboren. In 1984 behaalde hij het gymnasium β diploma aan het Jacob Roelantslyceum te Boxtel. Vervolgens studeerde hij Technische Natuurkunde aan de Technische Universiteit Eindhoven. In mei 1990 studeerde hij af op onderzoek aan hoge-temperatuur supergeleiders in de groep Coöperatieve Verschijnselen van Prof. Dr. Ir. W.J.M. de Jonge. Aansluitend trad hij als promovendus in dienst van het Energieonderzoek Centrum Nederland (ECN), hetgeen resulteerde in dit proefschrift. Vanaf 1 juli 1994 is hij als post-doc werkzaam bij het ECN.